# Modelling of Transionospheric HF Radio Wave Propagation for the ISIS II and ePOP Satellites

A Thesis Submitted to the
College of Graduate Studies and Research
in Partial Fulfillment of the Requirements
for the degree of Master of Science
in the Department of Physics and Engineering Physics
University of Saskatchewan
Saskatoon

By
Robert Gordon Gillies

# Permission to Use

In presenting this thesis in partial fulfilment of the requirements for a Postgraduate degree from the University of Saskatchewan, I agree that the Libraries of this University may make it freely available for inspection. I further agree that permission for copying of this thesis in any manner, in whole or in part, for scholarly purposes may be granted by the professor or professors who supervised my thesis work or, in their absence, by the Head of the Department or the Dean of the College in which my thesis work was done. It is understood that any copying or publication or use of this thesis or parts thereof for financial gain shall not be allowed without my written permission. It is also understood that due recognition shall be given to me and to the University of Saskatchewan in any scholarly use which may be made of any material in my thesis.

Requests for permission to copy or to make other use of material in this thesis in whole or part should be addressed to:

Head of the Department of Physics and Engineering Physics
116 Science Place
University of Saskatchewan
Saskatoon, Saskatchewan
Canada
S7N 5E2

# Abstract

The enhanced Polar Outflow Probe (ePOP) satellite is to be launched in 2007. One of the 8 instruments it will carry is a Radio Receiver Instrument (RRI) which is a passive radio receiver. The RRI will detect HF (High Frequency band 3 to 30 MHz) radio waves from ground transmitters, one of which is the Saskatoon SuperDARN radar. The modification of an HF radar wave as it propagates through the ionosphere to the satellite is the dominant scientific interest of this thesis. The modification of a radar wave as it propagates through the ionosphere can be used to characterize the ionosphere and reveal a better understanding of magnetoionic radar wave propagation. A ray tracing program has been written to determine characteristics of the wave, including the wave path and the full polarization state, at the satellite receiver.

As a confirmation of the ray tracing program abilities, data from a similar transionospheric experiment in 1978, the ISIS II satellite mission, has been analyzed and compared with simulated results. The ISIS II transionospheric experiment received radar signals from a transmitter (9.303 MHz) located in Ottawa, Canada. These signals were analyzed and it was noted that the signal periodically faded in and out both due to differential Faraday rotation effects (due to propagation through an ionized medium and reception on a single dipole antenna) and due to satellite spin rotation at rates up to 13 Hz. Also observed was a splitting of the received signal into Ordinary (O-mode) and Extraordinary (X-mode) components causing a delay between the arrival of the modes at ISIS II of up to 0.8 ms. Simulations have been carried out to model the radar wave propagation from the ground transmitter through the ionized medium of the ionosphere to the spacecraft. The modelled signal shows very similar trends to the observed signal. A linear regression analysis comparing observed to simulated fade rates gave values of slope equal to 1.07 and regression coefficient equal to 0.934. The regression analysis of mode delay gave

values of slope equal to 1.14 and regression coefficient equal to 0.930.

Ray path modelling has also been simulated for the RRI experiment on ePOP. These simulations have been carried out for various ionospheric and satellite pass configurations. The expected fade rates, mode delays, and latitudinal range of received signal was determined from the simulated data in each case. The dependence of these characteristics on the various pass configurations are presented and discussed.

# Acknowledgements

First and foremost, I'd like to thank my supervisor Dr. Glenn Hussey. For the opportunity to begin this project as a summer student and continue it in this thesis I am extremely grateful. If not for many patient hours spent in discussion about all aspects of this project from its overall goals down to simple grammar, I would not have been able to accomplish what I have.

A special thanks goes to Dr. Gordon James of the Communications Research Centre for introducing me to the ISIS satellite experiment which would ultimately form the backbone of my thesis. Also thanks for the helpfulness shown in many emails and discussions to help me understand better an almost unlimited number of items that have gone into this work.

I would also like to acknowledge Dr. Dieter Andre for his assistance in writing the original ray tracing program and assisting me in understanding it. Without this, the project would not have been able to even begin.

Thank you also to Dr. George Sofko for being a great teacher of so many of the concepts that went into this thesis. The theory section of this work was simple and easy to write due to clear and understandable teaching in class and out. Thanks also to Drs. Don Danskin, Sasha Koustov, and Kathryn McWilliams for support and advice.

I would like to express my thanks to the Department of Physics and Engineering Physics and the Institute of Space and Atmospheric Studies for financial assistance in the form of scholarships. I would also like to thank NSERC for funding this research and Dr. Andrew Yau who is the principle investigator for the ePOP satellite. Thanks also goes to the Canadian Space Agency for funding the ePOP satellite and the RRI which allowed this research to take place.

Finally, a special thanks to Megan for her unconditional love and support – regardless of how late I was out working some nights.

# Contents

# List of Tables

# List of Figures

# List of Abbreviations

| | |
|---|---|
| B-field | Magnetic Field |
| CADI | Canadian Advanced Digital Ionosonde |
| CASSIOPE | CAScade Smallsat and IOnospheric Polar Explorer |
| COSPAR | COmmittee On SPAce Research |
| CRC | Communications Research Centre |
| E-field | Electric Field |
| ePOP | enhanced Polar Outflow Probe |
| EUV | Extreme Ultraviolet |
| $f$oE | E-region peak |
| $f$oF1 | F1-region peak |
| $f$oF2 | F2-region peak |
| FOV | Field of View |
| HF | High Frequency (3-30 MHz) |
| $IG_{12}$ | Global Ionospheric Index |
| IGRF | International Geomagnetic Reference Field |
| IMF | Interplanetary Magnetic Field |
| IRI | International Reference Ionosphere |
| ISIS | International Satellites for Ionospheric Studies |
| LT | Local Time |
| NASA | National Aeronautics and Space Administration |
| $N_e$ | Electron Density |
| O-mode | Ordinary Mode |
| QL | Quasi-Longitudinal |
| QT | Quasi-Transverse |
| RRI | Radio Receiver Instrument |
| $R_{Z12}$ | 12-month running mean of sunspot number |
| SuperDARN | Super Dual Auroral Radar Network |
| URSI | International Union of Radio Science |
| UT | Universal Time |
| VHF | Very High Frequency (30-300 MHz) |
| X-mode | Extraordinary Mode |

# Chapter 1

# Introduction

## 1.1 Motivation for Research

In late 2007 a fully Canadian designed and built satellite will be launched. This satellite is called Cassiope and will carry a scientific payload called the enhanced Polar Outflow Probe (ePOP) which will be discussed in further detail in Chapter 5. There will be several main instruments on the payload, one of which is a Radio Receiver Instrument (RRI). The principle investigator (PI) of the RRI is Gordon James from the Communications Research Centre (CRC) in Ottawa, Canada. The RRI is designed to be a passive receiver of radio wave signals in the frequency range of 0-18 MHz. One interesting experiment that will be performed by the RRI is the monitoring of signals sent from various ground transmitters. In particular the Super Dual Auroral Radar Network (SuperDARN) array of antennas will be used to send HF (High Frequency) waves through the ionosphere to be detected by the RRI on ePOP.

The overarching goal of performing ionospheric studies is to develop a better and clearer understanding of all aspects of the ionosphere. This understanding can assist in such items as space weather predictions and global radio communications. The ePOP satellite will attempt to assist in these studies through two primary scientific goals: 1) quantifying of small-scale plasma outflow in the polar ionosphere and associated plasma wave processes at never before achieved resolutions, and 2) observation of neutral particle escape in the upper polar atmosphere [*Yau et al.*, 2002]. The instrument of interest in this thesis, the RRI, will assist in these goals by studying how a radio wave propagates through a medium such as the ionosphere. Many factors,

such as photoionization, convection, and polar outflow, influence plasma parameters such as density enhancements or depletions which may modify or be detected by radio waves. In essence ionospheric parameters and structures can be 'imaged' by the RRI experiment. Despite the concentration of ePOP on the polar regions, the transmitters used for the RRI experiment will send detectable amounts of signal to both auroral and mid-latitudes where the satellite can also detect these HF waves. The RRI will be able to study both large scale and small scale plasma processes. Large scale processes are associated with the modification of the radar wave as it propagates through the ionospheric plasma medium allowing for the detection of ionospheric structures (i.e., density enhancements and depletions, magnetospheric closing currents in the polar ionosphere, the mid-latitude trough region, to name a few). Small scale processes are associated with instability generation or reflections from gradients in the ionosphere. For example, a better understanding of coherent scattering mechanisms of HF waves is needed. Specifically, whether the scattering is always due to plasma waves generated by ionospheric instabilities (i.e., electrostatic plasma waves) or sometimes may be due to "partial reflection" from sharp electron density gradients in the ionosphere. It has been typically assumed that F-region coherent scatter, such as that observed by SuperDARN, is due to Bragg scattering from plasma waves; however, small-scale structures that could cause these waves to be reflected have been reported [*Trondsen and Cogger*, 1998]. Simultaneous measurements of back scatter observed by SuperDARN and forward scatter observed by the RRI will clarify this question.

The primary goal for this thesis is to develop a realistic model to predict the radio signal that will be received by the RRI on ePOP from a ground transmitter. The initial primary motivation for the modelling was to help in interpreting the RRI signals when the satellite becomes operational. Once the basic characteristics of the received signal were discovered through modelling, further analysis was done to examine the dependency of various ionospheric factors on the signal. As such, the analysis presented in this thesis provides a basis for interpretation of the transionospheric propagation experiment on ePOP and will allow a method for studying large

scale ionospheric properties. Specifically, this thesis deals with the effects of large scale ionospheric parameters such as overall electron density values on radio wave propagation. The initial case of a well-behaved and quiet ionosphere is reported here, while small scale effects are left for future research. The effect of these small scale structures on the propagating wave can reveal further information about the state of the ionosphere. For example, distortions in the received signal at various pass locations may be an indication of the existence of ionospheric structures [*Wang et al.*, 2004].

An experiment performed in 1978 by the ISIS II satellite mission provided an excellent starting point for the signal modelling. In conjunction with an HF ground transmitter located in Ottawa, Canada; the ISIS II spacecraft performed a similar experiment to the proposed RRI transionospheric propagation experiment. The ground transmitter operated at 9.303 MHz and its transmitted signal propagated through the ionosphere where it was detected by a dipole antenna located on the spacecraft. As outlined in this thesis, study of the characteristics of the received signal yielded two benefits: 1) it allowed insight into the type of signal to be expected for the RRI experiment and 2) it gave a testing ground for the modelling software that was developed.

## 1.2 Sun/Earth System

The ionosphere (discussed in Section 1.3) is the region of the atmosphere which the ePOP satellite will primarily study. This region is affected greatly by solar activity. As such, an understanding of solar processes and the linking of the Sun/Earth system is required for an understanding of the ionosphere of the Earth.

A large outflow of charged particles, called the solar wind, is produced by the Sun. This outflow is caused by the large pressure difference between the corona of the Sun and interplanetary space. The pressure pushing the steady stream of ionized particles outwards from the Sun overcomes the gravitational attraction of the Sun. The measured properties of the solar wind near Earth show a typical electron density

of $\sim$7 $cm^{-3}$ and a flow speed of $\sim$450 $km \cdot s^{-1}$ [*Kivelson and Russell*, 1995]. A weak interplanetary magnetic field (IMF) is produced by the Sun which has a strength near Earth of <10 nT. The charged particles of the solar wind attach to the highly conducting IMF lines and carry the field with them as they travel outwards from the Sun. The positive ions in the solar wind are in equal numbers to the electrons and are made up mostly of protons and a small number of helium atoms.

The magnetic field of the Earth can be approximated as a dipole field with the northern magnetic pole situated near the southern geographic pole of the Earth and the southern magnetic pole situated near the northern geographic pole of the Earth. Therefore, the magnetic field lines are oriented nearly vertically in the polar regions and point northward in the equatorial region. The area within the closed magnetic field lines of the Earth is known as the magnetosphere. On the sunward side, the interaction of the IMF with the magnetic field of the Earth compresses the magnetosphere, while on the anti-sunward side the magnetosphere is significantly expanded ('dragged' by the IMF) as can be seen in Figure 1.1. The IMF constantly interacts with the magnetosphere of the Earth and this causes magnetic field lines of the Earth to connect to the IMF lines. Since the solar wind is constantly streaming past the Earth, the newly connected field lines get dragged backwards over the polar regions of the Earth and drive ionospheric plasma convection in these regions. This interaction also opens up the magnetosphere to solar wind plasma. The magnetic field lines are excellent conductors of charged particles and, as such, magnetospheric plasma streams down the magnetic field lines into the atmosphere of the Earth. The streaming plasma causes ionization at ionospheric altitudes and can create optical emissions that are known as the aurora. These auroras are better known as the Northern or Southern Lights, depending on which hemisphere is examined. The auroras occur mostly in the polar regions of the Earth because the magnetic field lines are basically vertical at high latitudes and allow high altitude magnetosphere plasma access to lower ionosphere altitudes [*Kelley*, 1989]. The solar wind can vary rapidly in density and speed depending on solar activity. Such variations in the solar wind directly affects ionospheric activity on Earth. As explained in the next section,

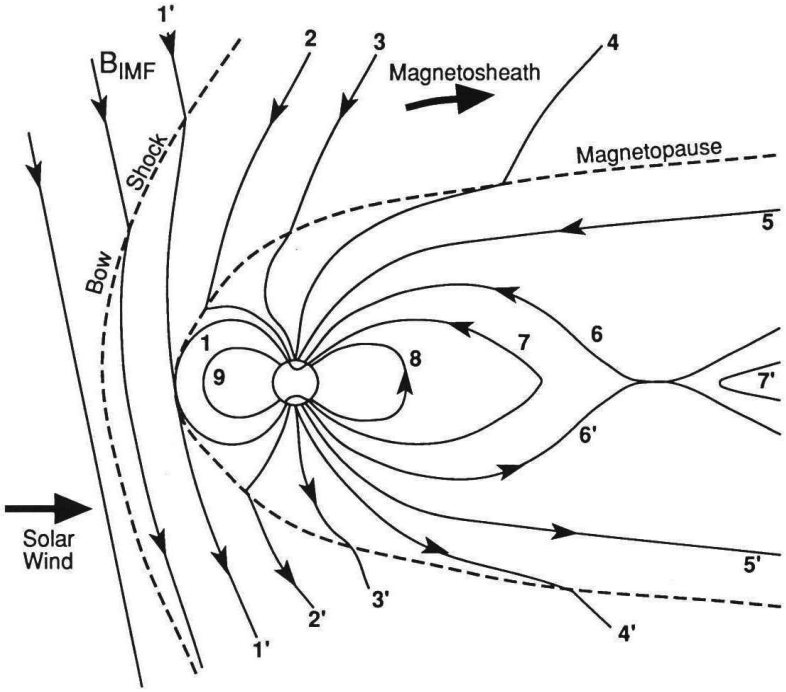


Figure 1.1: The interaction of the IMF and solar wind with the magnetosphere of the Earth. The IMF lines connect with the field lines of the magnetosphere of the Earth and drive convection of plasma in the polar regions. The bow shock represents the location of pressure balance between the solar wind and the magnetosphere of the Earth. The magnetopause defines the boundaries of the closed field lines of the magnetosphere. Finally, the magnetosheath is the area encompassed by the bow shock and magnetopause. Figure 9.11 from *Kivelson and Russell* [1995].

the electron density in the ionosphere is highly dependent on solar activity.

## 1.3 The Ionosphere of The Earth

The ionosphere is the region of the atmosphere where free ions and electrons can exist (in a quasi-neutral plasma such as the ionosphere, the number of free electrons is approximately equal to the number of free ions). The boundaries of the ionospheric regions are not clearly defined. The bottom of the ionosphere is generally estimated at ∼100 km altitude [*Kivelson and Russell*, 1995], although in general there is some ionization in the atmosphere down to ∼80 km. The upper limit of the ionosphere

is quite ambiguous and rarely mentioned in textbooks [*Kelley*, 1989; *Davies*, 1966; *Kivelson and Russell*, 1995; *Budden*, 1985; and *Hunsucker and Hargreaves*, 2003], however it is generally accepted to range up to several thousand kilometers.

The ionosphere is formed mainly by the radiation of the Sun striking the atmosphere of the earth and ionizing molecules [*Davies*, 1966]. There are several forms of radiation that will cause ionization of the molecules in the atmosphere. This ionizing radiation includes; extreme ultraviolet (EUV) light (eV), X-rays (keV), solar wind particles (up to MeV range), or even cosmic rays (GeV range) that are not from the Sun. In practice, however, the main contributer to ionization is EUV light from the Sun.

Two items are needed for the creation of substantial quantities of ionized molecules. First, the molecules themselves are needed in sufficient quantities to be ionized. Second, some mechanism for ionizing the molecules is needed. At heights below 80 km, there is a large quantity of neutral molecules, however very few photons of the appropriate energy penetrate that deep into the atmosphere because they are mostly all absorbed above. Also, if any electron/ion pairs are created they quickly recombine with each other due to collisions with the high neutral atmosphere density. The net result is essentially no ionization near the earth. At high altitudes ($\sim$1000 km) there are sufficient numbers of EUV photons from the Sun, however there is very little atmosphere to be ionized. The net result is a low number of ionized pairs (low electron density). In between these two extremes, a compromise is reached. There is enough atmosphere to create ionized pairs and many photons penetrate to these heights because there is little absorbing atmosphere above [*Budden*, 1985]. The net result is a relatively high electron density between about 100 km and 500 km, with a peak electron density ($N_e$) that can reach more than $10^{12}$ m$^{-3}$. A general plot of electron density as a function of height is presented in Figure 1.2. From this figure it can be noted that the highest electron density occurs at $\sim$300 km. The main regions of the ionosphere are indicated in this figure.

There are three main regions in the ionosphere. Two of these regions, the E-region and F-region, are defined by electron density peaks. The first region that

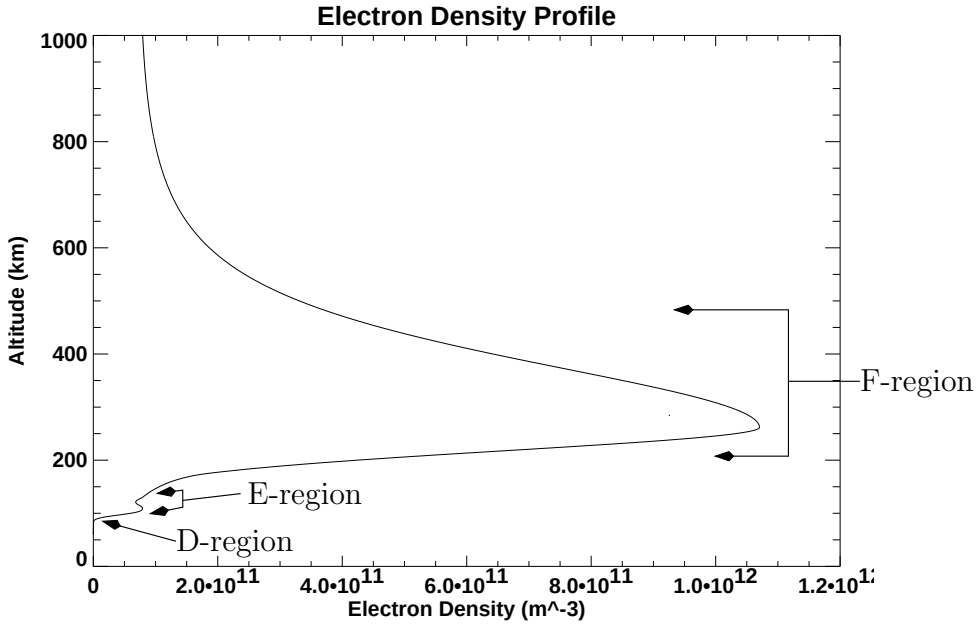


Figure 1.2: A typical electron density profile of the ionosphere of Earth. The profile was generated from the International Reference Ionosphere (IRI) modelling program (see Chapter 3).

was discovered was the E-layer. Its peak was the first to reflect radio transmissions and it was called the E-layer for 'Electric-layer' [*Kivelson and Russell*, 1995]. The E-layer or E-region exists between ∼90 km to 150 km altitude. The peak of the E-region occurs at ∼110 km altitude and has an electron density on the order of $10^{11}$ m$^{-3}$ during the day [*Kelley*, 1989]. The next region is the F-region. The F-region exists at all heights in the ionosphere above the E-region — from ∼150 km and up. The peak electron density in the F-region can be higher than $10^{12}$ m$^{-3}$ and is located at ∼300 km. The F-region is actually further classified by the F1 and F2 peaks. The F1 peak occurs at the lower altitude of the two peaks and is not always present, especially for winter conditions [*Hunsucker and Hargreaves*, 2003]. The F2 peak is the location of the highest $N_e$ value and exists above the F1 peak. The third defined region of the ionosphere is the D-region. The D-region is not defined by a peak electron density; it is simply the layer below the E-region on the bottom of the ionosphere. The electron density in the D-region is very low and at times is

non-existent. Each region is highly variable with respect to time and location. The electron density peak values in the ionosphere all vary by more than a factor of ten depending on time and location.

The peak electron densities in the ionosphere are commonly referenced with respect to the maximum radar frequency that can be reflected by them. This is related to the local plasma frequency of the medium and will be discussed in Chapter 2. Due to this relationship of radar frequency and peak electron density values, the E-region peak is referred to as the $f$oE peak and the F1 and F2 peaks are referred to as the $f$oF1 and $f$oF2 peaks, respectively, where $f$o refers to the maximum radar frequency reflected.

The production of electron/ion pairs in the ionosphere is driven in a similar fashion to the heating of the surface of the Earth. The more vertically overhead the Sun is positioned, the more heat is delivered, and the more ionized molecules are produced. A result of this is that there is generally a higher overall electron density nearer to the equator than at higher latitudes. One would expect that the highest electron densities would be found directly at the equator, but actually there is an $N_e$ trough region directly over the equator and the overall electron density increases to peak values at $\sim \pm 10$–$20^\circ$ latitude [*Bhuyan et al.*, 2003]. This phenomenon is known as the equatorial ionization anomaly and may be explained by the "fountain effect". At the equator there is an eastward pointing electric field during the daytime that couples with the northward magnetic field to create an upward **ExB** drift motion of plasma [*Kelley*, 1989]. This upward motion causes plasma to travel upwards from the F-region at the equator and be transported downwards along the magnetic field lines north and south of the equator thus reducing the plasma or electron density at the equator.

For a sunlit (daytime) ionosphere, the Sun creates electron/ion pairs through photoionization at a faster rate than recombination. As a result, typically there is a peak in $f$oF2 near or shortly after noontime [*Bhuyan et al.*, 2003]. The $f$oF2 peak slowly drops off as the Sun sets and reaches a minimum right before sunrise when recombination has had the most time to decrease the number of ionized pairs.

Typically, therefore, daytime $N_e$ peak values are usually much higher than nighttime values.

One general behaviour of the $f$oF2 peak that does not follow from the simple rule of more sunlight causing higher electron density values is a seasonal dependence which is operational at higher latitudes. One would expect that in winter time a lower electron density peak will exist than during summer. This is indeed the case for nighttime $N_e$ levels, but during the daytime for winter months higher F-region electron densities are observed. This is referred to as the seasonal anomaly [*Davies*, 1966]. A typical daytime $f$oF2 peak in the winter at higher latitudes will be nearly an order of magnitude higher than a typical summer $f$oF2 peak. This F-region characteristic is not as apparent at lower latitudes and this is to be expected because lower latitudes are not as seasonally dependent as higher latitudes. The reason for this anomaly is the different compositions of ions in the F-region between the two seasons. It has also been reported that at middle latitudes, a semiannual variation in the noontime $f$oF2 peaks exists with maximum $N_e$ occurring at the equinoxes [*Richards*, 2001].

## 1.4 Ground Ionospheric Experiments

Evidence of an ionized component of the atmosphere of the Earth became apparent in 1901 when Marconi sent radio frequency transmissions from the British Isles to Newfoundland. Due to the curvature of the Earth, it would be impossible for straight line of sight transmissions over this distance so it was apparent that the radar waves must have been reflected off of an ionized layer [*Hunsucker and Hargreaves*, 2003].

One of the first and simplest methods for studying the ionosphere was to use an ionosonde. An ionosonde is basically a radio transmitter and receiver system which can operate at radio frequencies up to 20-30 MHz [*Hunsucker and Hargreaves*, 2003]. Ionosondes are typically pulsed radar systems (transmit a pulse, wait for the returned signal to be received, repeat over and over) which can change frequency (sweep in frequency) from 1 to 20 MHz. By measuring the time for a reflection of

a radio wave from the ionosphere at each frequency, a listing of electron density as a function of altitude above the ionosonde can be developed. The physics of this is discussed in Chapters 2 and 4, but basically radio waves at or below the local plasma frequency are reflected and higher frequency ones propagate through the ionosphere. Ionosondes can give reliable $N_e$ profiles (bottomside soundings or ionograms) up to the F-region peak at ∼300 km altitude. Chapter 4 discusses the use of ionosondes on satellites to determine $N_e$ profiles for altitudes in the ionosphere above the F-region peak.

In Canada, a collection of ionosonde stations make up the Canadian Advanced Digital Ionosonde (CADI) network [*MacDougall et al.*, 1995]. Radars from the CADI network will be used as transmitters, as well as SuperDARN radars, in the transionospheric propagation experiment with the RRI instrument on ePOP.

Another method for study of the ionosphere is to use coherent backscatter radars. One of the most prominent examples of this is the SuperDARN system [*Greenwald et al.*, 1995]. There are numerous SuperDARN radar sites scattered about the globe. The basic principle of a SuperDARN radar is to have a coherent HF wave between ∼8–20 MHz scatter from field aligned irregularities in the high latitude ionosphere. By measuring the Doppler shift of the the scattered wave, the line of sight plasma drift velocity in the F-region can be determined. Two radars probing the same area of the F-region can determine two line of sight velocities and the addition of these vectors will give the actual velocity of the plasma. The SuperDARN network of radars operates continuously and covers almost the entire region (polar cap) of both the north and south poles. As such, convection maps of the ionosphere are generated on a minute by minute basis and stored for later study. Since the ionosphere reacts to processes from the Sun and magnetosphere, these convection maps offer information on the behaviour of the Earth/Sun environment. It is planned to use at least the SuperDARN radar in Saskatoon, Canada for the ePOP mission. Only a small fraction of the transmitted signal is scattered in the ionosphere and most propagates out into space. The RRI on ePOP will fly through the SuperDARN field of view and be able to receive and record this signal transmitted from the ground which was modified as

it propagated through the ionosphere.

## 1.5 Canadian Ionospheric Satellites

In 1962 Canada became the third country in history to have a satellite in orbit around the Earth. Alouette 1 was launched and became operational on September 29, 1962 [*Hartz*, 1964]. This satellite was entirely designed and built in Canada and was launched by the National Aeronautics and Space Administration (NASA) in the United States. The primary goal of the Alouette satellite was to perform topside soundings of the ionosphere to determine electron density profiles from ∼300 km (the $f$oF2 peak) to the altitude of the spacecraft at ∼1000 km. Alouette 1 also provided data on local magnetic field strength. The spacecraft was designed to operate for only a year, but ended up performing its mission for ten years. The Alouette 1 satellite had a back up built in case of malfunction with the original. This back up was launched as Alouette 2 in 1965 and performed a similar mission to its predecessor. For more information on the Alouette satellites see `http://www.space.gc.ca/asc/eng/satellites/alouette.asp`.

The success of the Alouette program led to the development of a new class of satellites called ISIS (International Satellites for Ionospheric Studies). ISIS I was launched in 1969 and flew in an elliptical orbit with a perigee of ∼550 km and an apogee of ∼3500 km. In 1971, ISIS II was launched into a nearly circular orbit of 1400 km. Like the Alouette missions, the main goals of both these satellites was to develop topside soundings or ionograms of the ionosphere. They also contained other instruments to measure temperature and magnetic field strength. ISIS II also had the ability to take photographs of the entire auroral oval over the North pole. An experiment was also performed with both satellites which was of importance to the goals of this thesis. Both satellites received HF radar transmissions from several dedicated ground transmitters. The received signal was able to reveal information on how the radio wave was affected as it propagated through the ionosphere. These transionospheric experiments on the ISIS satellites are similar to the RRI experiment on the upcoming

ePOP satellite. As well, the millions of topside profiles produced from the Alouette and ISIS spacecraft programs are the primary data sets used for the topside portion of ionogram profiles produced by the International Reference Ionosphere (IRI) model [*Bilitza*, 2004]. The IRI model is the international standard for ionospheric density modellers and is discussed in Chapter 3. Further information on the ISIS satellites is found at `http://www.space.gc.ca/asc/eng/satellites/isis.asp`.

## 1.6 Outline of Thesis

Chapter 2 of this thesis gives background on magnetoionic theory. The derivation of the complex index of refraction in an ionized magnetic medium is presented. Then an overview of radio wave polarization states will be discussed. Finally, the different propagation characteristics of a wave travelling parallel or perpendicular to magnetic field lines will be explained.

A great deal of programming was performed to model the behaviour of propagating waves in the ionosphere. These so-called ray tracing programs (simulations) are discussed and explained in Chapter 3. Also discussed in this chapter is the IRI electron density modelling program used to supply $N_e$ profiles for the ray trace modeller.

The ISIS II satellite performed an experiment that was similar to the upcoming HF wave propagation (transionospheric) experiment of the RRI on ePOP. The data analysis from the ISIS II experiment is presented in Chapter 4. In this chapter simulations of actual ISIS II transionospheric observations using the ray trace modeller are explained. Comparisons between the ray tracer simulations and the actual data are made.

Chapter 5 presents and discusses some preliminary simulations which describe the expected radar wave signal to be received by the RRI on ePOP from SuperDARN transmissions. Various ionospheric electron densities, satellite parameters and transmitting frequencies are compared. The results of these simulations are examined with respect to the ionospheric physics discussed in Chapter 2.

Finally, Chapter 6 summarizes the results and conclusions from the ray tracer simulations for ePOP and ISIS II experiment analysis. Future directions are also discussed.

# Chapter 2

# Magnetoionic Theory

Magnetoionic theory is the study of the propagation of electromagnetic (EM) waves through an ionized magnetic medium. As the ionosphere is a weakly ionized plasma this theory is fundamental to research of this thesis. The polarization state of the wave also must be known. This chapter presents magnetoionic and polarization theory.

## 2.1 Electromagnetic Wave Polarization State

One of the main goals of this thesis is to understand the polarization state of a radio wave when it is received by ePOP after propagating through the ionosphere. In order to discuss this effectively, the various definitions and terminology used in this research must be presented. This section will provide a brief overview of polarization definitions used in this thesis.

The EM or radar wave considered will be a monochromatic wave. This is a theoretical wave that is infinitely long. The polarization of a wave is defined by the shape that the end point of the electric field vector traces out as the wave propagates. The polarization can be defined by either the magnetic field vector or the electric field vector as they are oriented perpendicular to one another; however, since antennas and their receivers make electric field measurements, the electric field is what is commonly used when discussing polarization. In general, the polarization of a signal is elliptical and the polarization state is referred to as a polarization ellipse.

Figure 2.1 shows the general form of a polarization ellipse. The orientation angle ($\psi$) is defined as the angle between the $x$-axis and the semi-major axis of the ellipse

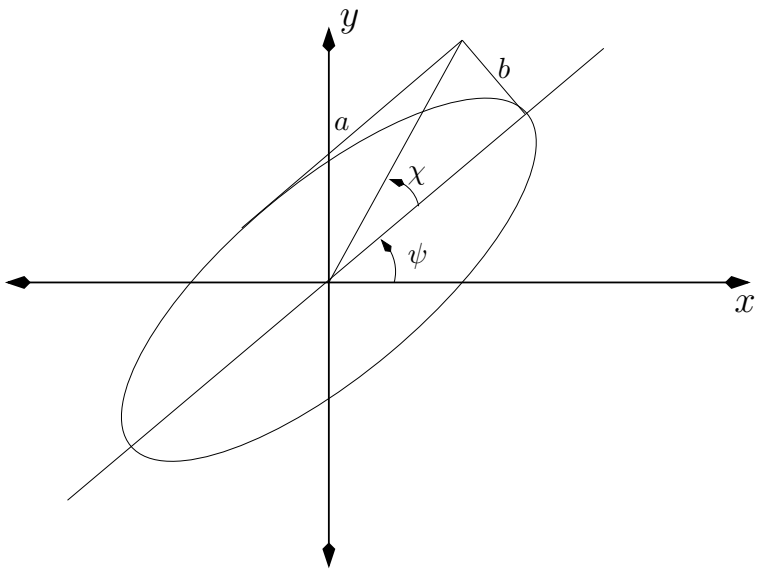


Figure 2.1: A general form of the polarization ellipse. $\psi$ represents the orientation angle, $a$ represents the semi-major axis, $b$ represents the semi-minor axis, and $\chi$ represents the ellipticity angle of the ellipse.

and can range from 0° to 180° [*Born and Wolf*, 1980]. The ellipticity angle ($\chi$) is defined as the ratio of the semi-minor axis ($b$) to the semi-major axis ($a$),

$$\chi = \pm \arctan(\frac{b}{a}). \tag{2.1}$$

The ellipticity angle ranges from -45° to 45°. The polarization ellipse can have a form from linear (which is an ellipse with an ellipticity of 0°), to circular (an ellipse with ellipticity of ±45°). The variables $\psi$ and $\chi$ define the shape of the polarization ellipse and the inclusion of either one of the axes magnitudes $a$ or $b$ will define the polarization of the wave completely. The state of the wave can be further defined by the inclusion of an unpolarized component of the signal in addition to the polarization ellipse. The unpolarized component corresponds to completely random motion of the electric field endpoint. The amplitude of an unpolarized wave will be the same in any direction that is perpendicular to the propagation direction. In actual data there will always be an unpolarized portion of the wave, however for the signals dealt with in this research it is expected to typically be small and is not considered. In future research it is expected that analysis including the unpolarized wave component may

be of importance.

## 2.2 Appleton-Hartree Derivation

The first step to studying the propagation of a wave through the ionosphere is to determine the index of refraction of a travelling radio wave in an ionized magnetic medium. This is also crucial for determining the polarization state of the wave. As will be shown below, the index of refraction and polarization state of a wave in such a medium are directly related. As outlined below, when a wave propagates through an ionized medium with an external magnetic field, two different indices of refraction exist. These two indices of refraction correspond to two modes of propagation. The ordinary mode (O-mode) and the extraordinary mode (X-mode) are affected differently by the external magnetic field (B-field). In magnetoionic propagation, both modes have an index of refraction that is less than unity, with the X-mode having a smaller value than the O-mode. To determine the index of refraction in the ionosphere, one can use the Appleton-Hartree equation. Below, the Appleton-Hartree equation is derived using the method expressed by *Budden* [1961].

Firstly, Maxwell's equations are used to derive a relationship between the magnetic and electric fields of a propagating electromagnetic (EM) wave. The two Maxwell equations that are used are:

$$\nabla \times \mathbf{E} = -\mu_o \frac{\partial \mathbf{H}}{\partial t}, \tag{2.2}$$

$$\nabla \times \mathbf{H} = \frac{\partial \mathbf{D}}{\partial t}, \tag{2.3}$$

where, $\mathbf{E}$ is the electric field of the EM wave, $\mathbf{H}$ is the magnetic field of the EM wave, $\mathbf{D}$ is the electric displacement of the wave and $\mu_o$ is the permeability of free space. Also needed is the relation between $\mathbf{E}$, $\mathbf{D}$, and the polarization field ($\mathbf{P}$). This relation is given by

$$\mathbf{D} = \epsilon_o \mathbf{E} + \mathbf{P}, \tag{2.4}$$

where $\epsilon_o$ is the permittivity of free space. It should be noted that in this notation the polarization field refers to the field that develops in a material from the imposed

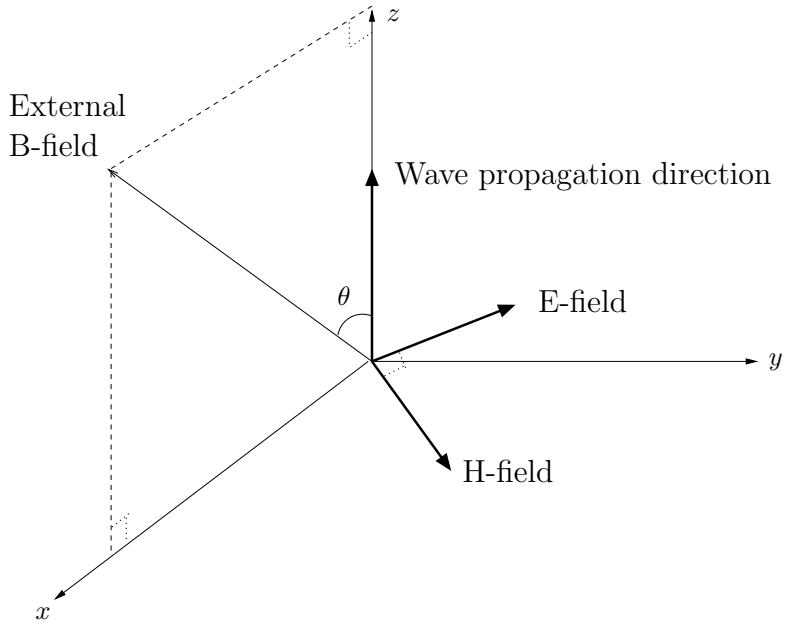


Figure 2.2: Geometry for Appleton-Hartree Derivation.

external electric field of the EM wave applying a force in opposite directions on the electrons and ions in the material. The polarization field should not be confused with the polarization state of the wave, which refers to the shape the endpoint of the electric field of a travelling EM wave traces out as explained in Section 2.1.

Assuming a harmonic EM wave traveling in the $+z$ direction with its wave vector given by $\mathbf{k} = k\hat{z}$, the geometry for this derivation is shown in Figure 2.2. The $x$-axis is positioned so that the component of the B-field in the $xy$-plane is aligned along it, so that $\mathbf{B} = B\hat{x} + B\hat{z}$. The E-field (or H-field) of the wave is given by

$$\mathbf{E} = \mathbf{E}_o e^{i(kz-\omega t)}, \tag{2.5}$$

where $\mathbf{E}_o$ is the maximum amplitude of the E-field, $k$ is the wave number, and $\omega$ is the wave angular frequency. Therefore, taking the curl operator of $\mathbf{E}$ or $\mathbf{H}$ will give the spatial $(ik)$ term, while taking the time derivative will give the temporal $(-iw)$ term. When Equations 2.2 and 2.3 are expanded and rearranged using this knowledge the following is obtained:

$$\mathbf{D} = \frac{k^2}{\mu_o \omega^2}(E_x\hat{x} + E_y\hat{y}), \tag{2.6}$$

$$\mathbf{H} = \frac{k}{\mu_o \omega}(-E_y \widehat{x} + E_x \widehat{y}). \tag{2.7}$$

It should be understood that in this notation, the phasor term of the various fields has simply been implied. For example, $E_x$ refers to $E_{xo}exp(i(kz-\omega t))$. By combining Equations 2.4, 2.6 and 2.7 one arrives at the ratio $\rho$ given by

$$\rho \equiv \frac{P_y}{P_x} = \frac{E_y}{E_x} = \frac{D_y}{D_x} = \frac{-H_x}{H_y}. \tag{2.8}$$

$\rho$ defines the wave polarization. It is the ratio between the $x$ and $y$ components of the various fields. This ratio will describe the polarization state of either mode.

Using the definition of index of refraction

$$n \equiv \frac{kc}{\omega}, \tag{2.9}$$

where $c$ is the speed of light in a vacuum given by [*Griffiths*, 1999]

$$c = \frac{1}{\sqrt{\epsilon_o \mu_o}}, \tag{2.10}$$

Equation 2.6 can be rewritten as shown in Equation 2.11.

$$\mathbf{D} = \epsilon_o n^2 (E_x \widehat{x} + E_y \widehat{y}). \tag{2.11}$$

One further relation that will be needed is that of polarization and electric field. By combining 2.4 and 2.11 one gets

$$\mathbf{P} = \epsilon_o (n^2 - 1)(E_x \widehat{x} + E_y \widehat{y}) - \epsilon_o E_z \widehat{z}. \tag{2.12}$$

It should be noted that in Equation 2.12 an $E_z$ term has appeared. In most EM wave propagation cases there is no component of the E-field along the wave vector direction. This is not the case in magnetoionic wave propagation. The $E_z$ term is typically small and is ignored here.

The next step in the Appleton-Hartree derivation is to examine the equation of motion for an electron in a magnetoionic medium. There are three forces acting on the electron: the electric force, the magnetic force, and frictional forces. This leads to the following equation of motion

$$m\frac{d^2\mathbf{r}}{dt^2} = -e\mathbf{E} - e\frac{d\mathbf{r}}{dt} \times \mathbf{B} - \nu m \frac{d\mathbf{r}}{dt}, \tag{2.13}$$

where $m$ is the mass of an electron, $\mathbf{r}$ represents the position vector of the electron, $e$ is the elementary charge, $\mathbf{B}$ is the external magnetic field, and $\nu$ is the collision frequency of electrons with other particles. The first term in the equation of motion is the electric force, the second term is the magnetic force and the last term is the frictional force. It is assumed that the motion follows a harmonic oscillation in the same manner as Equation 2.5. With much rearranging and use of Equation 2.14, which defines the resulting net polarization field from a displaced set of electrons, one arrives at a slightly different version of the original equation of motion, which is Equation 2.15.

$$\mathbf{P} = -N_e e \mathbf{r}, \tag{2.14}$$

$$-\mathbf{P} = \frac{N_e e^2 \mathbf{E}}{m\omega^2} + \frac{ie\mathbf{P} \times \mathbf{B}}{m\omega} + \frac{i\mathbf{P}\nu}{\omega}, \tag{2.15}$$

where $N_e$ is the free electron density in the plasma.

The plasma frequency is defined by Equation 2.16 and the cyclotron or gyro frequency is defined by Equation 2.17 and both can be used to simplify Equation 2.15. The plasma frequency describes the frequency at which free electrons oscillate in a plasma. Radar waves below the plasma frequency will be reflected by the plasma while radar waves above this frequency will propagate through. The cyclotron frequency describes the frequency at which the free electrons will gyrate about the external magnetic field. These definitions are further simplified by the definitions shown in equations 2.18 through 2.21. In these equations $\theta$ is the aspect angle. This angle is the angle formed between the magnetic field and the direction of propagation ($\mathbf{k}$) of the EM wave.

$$\omega_p^2 = \frac{N_e e^2}{m\epsilon_o}, \tag{2.16}$$

$$\omega_c = \frac{eB}{m}, \tag{2.17}$$

$$X = \frac{\omega_p^2}{\omega^2}, \tag{2.18}$$

$$Y_T = \frac{\omega_c}{\omega} \sin\theta, \tag{2.19}$$

$$Y_L = \frac{\omega_c}{\omega} \cos\theta, \tag{2.20}$$

$$U = 1 + i\frac{\nu}{\omega}. \tag{2.21}$$

$X$ is the ratio of plasma frequency to radar frequency. $Y_T$ and $Y_L$ are the ratios between cyclotron frequency and radar frequency in the transverse and longitudinal directions with respect to the external magnetic field respectively. $U$ is a factor that relates collision frequency to radar frequency.

It should be noted that in this research collisions between electrons and neutrals has been neglected. In the E-region, collisions can have an effect on a propagating EM wave; however, typically for the radar frequencies of interest in this thesis the affect of collisions can be ignored in the E-region, which makes up a very small portion of the radar wave path. The majority of the modifications to the wave take place in the F-region where the $N_e$ is highest. The collision frequency of electrons and ions is negligible for altitudes above the E-region ($\sim 10^3$ Hz, compared to a typical radar frequency of $\sim 10^7$ Hz), and therefore it is reasonable to neglect the effect of collisions at this time.

With the use of these definitions, Equation 2.15 can be broken down into its component form. When this is done, the following equations result:

$$-\epsilon_o X E_x = U P_x + i Y_L P_y, \tag{2.22}$$

$$-\epsilon_o X E_y = -i Y_L P_x + U P_y + i Y_T P_z, \tag{2.23}$$

$$-\epsilon_o X E_z = -i Y_T P_y + U P_z. \tag{2.24}$$

One can rearrange these equations to develop an expression for $\rho$ in Equation 2.8 and thus for the magnitude ratio of the $x$-axis and the $y$-axis of the various fields. This expression is shown in its final form as

$$\rho = \frac{i Y_T^2}{2 Y_L (U - X)} \pm i \sqrt{\frac{Y_T^4}{4 Y_L^2 (U - X)^2} + 1}. \tag{2.25}$$

This equation gives the ratio between $E_x$ and $E_y$ or $H_x$ and $H_y$ as expressed in Equation 2.8. This ratio is used to determine the polarization state of either mode. From this equation, the O-mode ratio is determined using the negative sign and the X-mode ratio is determined using the positive sign.

Using Equations 2.12, 2.22 and 2.25 one can derive the final form of the equation describing the index of refraction ($n$) in an ionized magnetic medium. The Appleton-Hartree equation is thus given as

$$n^2 = 1 - \frac{X}{U - \frac{Y_T^2}{2(U-X)} \pm \sqrt{\frac{Y_T^4}{4(U-X)^2} + Y_L^2}}. \tag{2.26}$$

There a several important features to observe in this equation. The first is that there are two values for the index of refraction in a plasma. These two values correspond to the two modes of propagation. The X-mode is most affected by the medium and therefore it is the smaller of the two. Taking the negative sign in the Appleton-Hartree equation will give the value for the X-mode. The O-mode is closer to unity and is found by using the positive sign in the equation. The next item to notice is that the index of refraction is highly dependent on $X$ which is directly related to electron density. Therefore, the index of refraction will deviate more from unity for larger values of electron density. Also, the index of refraction of the two modes will differ from one another by the most amount for large values of electron density. The final note is that the index of refraction only has an imaginary term in the $U$ variable. If there are no collisions between electrons and ions, the value for index of refraction becomes purely real. The previous statements only hold for values of $X$ $< 1.0$. When $X$ approaches 1.0, the situation becomes much more complicated.

A plot of $n^2$ as a function of the ratio $X$ is shown in Figure 2.3. It is seen that as $X$ approaches 1.0, the index of refraction for the X-mode becomes purely imaginary (because $n^2$ is negative) and it only propagates as an evanescent wave which is a wave that decays exponentially with distance. This occurs at the point,

$$X = 1 - Y. \tag{2.27}$$

where

$$Y^2 = Y_T^2 + Y_L^2. \tag{2.28}$$

When $X$ becomes 1.0 exactly, the O-mode also becomes evanescent. Slightly before this point where $X$ becomes exactly 1.0, another mode appears at a value of

$$X = \frac{1 - Y^2}{1 - Y_L^2}. \tag{2.29}$$

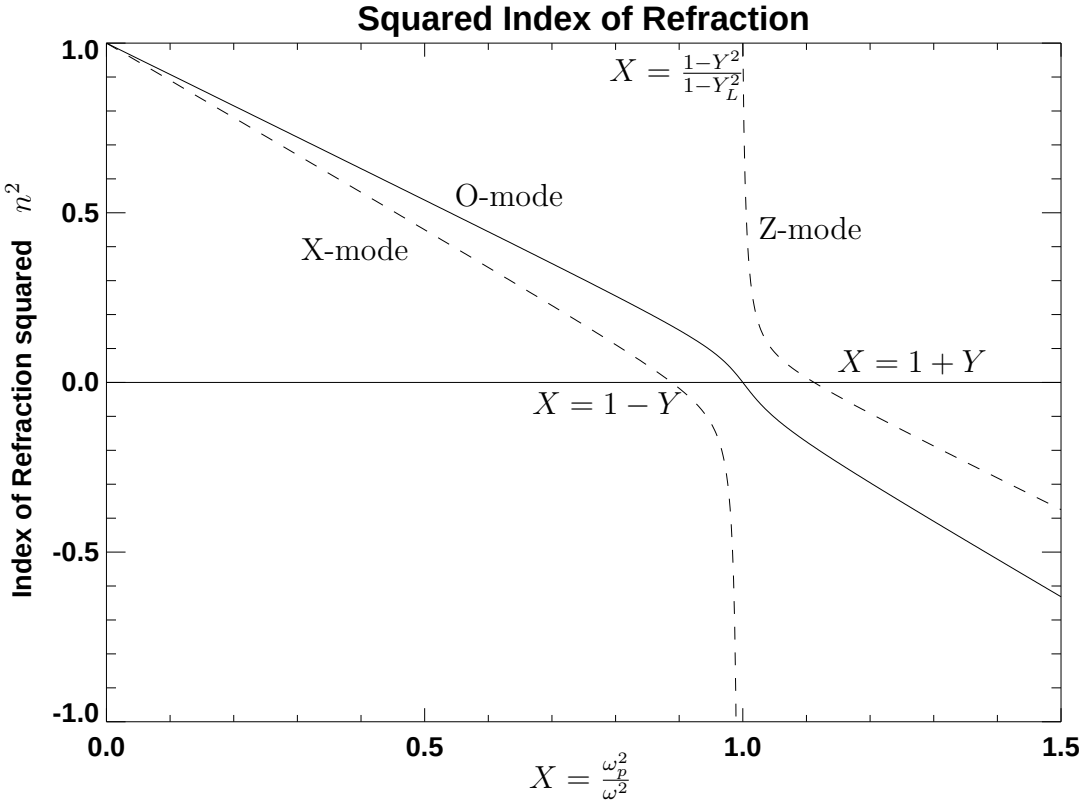


Figure 2.3: $n^2$ for increasing values of $X = \frac{\omega_p^2}{\omega^2}$, (aspect angle is 40°, radar frequency is 15 MHz, magnetic field strength is 0.600 G). All values of $n^2 < 0.0$ represent evanescent, non-propagating waves. Note that the X-mode is always at a lesser value than O-mode and the separation between them increases as $X$ increases. Z-mode waves propagate under the condition of $X > 1.0$. Note that an '$X$' refers to the term in Equation 2.18, while the 'X' in X-mode refers to the extraordinary propagation mode.

This is actually the X-mode from the Appleton-Hartree equation, but because physically it is separated from the classic X-mode propagation it is often called the Z-mode. This mode will become evanescent at the point

$$X = 1 + Y. \tag{2.30}$$

The Z-mode only propagates at relatively low frequencies (<2 MHz) given normal ionospheric conditions.

## 2.3 QT and QL Propagation

In the previous section it is shown that the index of refraction and polarization ratios of the propagation modes are described by quite elaborate equations. Further, different propagation characteristics are exhibited for propagation in different directions with respect to the external B-field. If the EM wave is propagating more or less parallel or anti-parallel to the external B-field lines, this is called quasi-longitudinal (QL) propagation. On the other hand, if the wave is travelling more or less perpendicular to the external B-field, it is called quasi-transverse (QT) propagation. Interestingly, under typical ionospheric conditions relatively high frequency waves can be considered to propagate in the QL regime for very large aspect angles. For example, at a VHF radar frequency of 50 MHz the propagating wave can be well described by the QL approximation for aspect angles up to nearly 87° [*Hussey*, 1994]. At a typical HF SuperDARN operating frequency (∼15 MHz), the QL approximation is valid for aspect angles up to ∼60°. The resultant polarization states for QT and QL propagation are quite different and are examined below.

Imagine a linearly polarized radar signal travelling parallel (or anti-parallel) to the B-field lines such that $\theta$=0°. This wave will be split into two circular waves of opposite sense with different indices of refraction. The 'sense' of a polarization ellipse is determined by the direction in which the electric field vector traces out the ellipse. Examination of Equation 2.25 indicates that under these conditions the magnitude of the axis ratio is unity. Both terms with $Y_T$ are zero and the result is $\rho = \pm i$. As $|\rho|$=1, the magnitude of the field along either axis of the modes is equal and therefore each mode propagates as a circular wave. These two circular waves will rotate at slightly different rates (due to the different indices of refraction) and with different senses of rotation (due to the different signs for $\rho$). The net result of two circular waves of the same magnitude propagating with different senses is a linear wave. Since the waves have different indices of refraction, they will go through different amounts of phase in a set distance. This will result in a change in the orientation angle of the resultant linear wave as it propagates. This effect

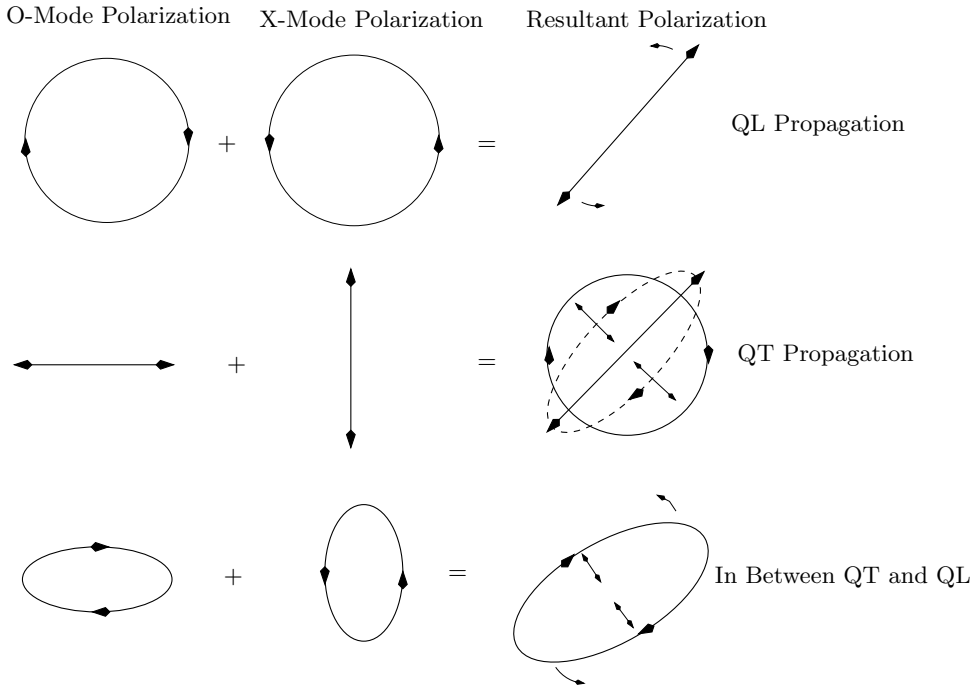


Figure 2.4: Polarization ellipses for various aspect angles with collisions neglected.

is called Faraday rotation [*Budden*, 1985]. Faraday rotation can only be operable when the QL propagation conditions are met. The Faraday rotation effect has be used for a number of research experiments such as calculating the electron density in the E-region [*Hysell and Chau*, 2001] or F-region [*Shpynev*, 2004] and estimating the plasma density in the corona of the Sun by measuring the Faraday rotation that the corona causes on a galactic radio source [*Mancuso and Spangler*, 1999].

QT propagation conditions are valid when the wave propagation direction is perpendicular to the B-field ($\theta$=90°). Examination of Equation 2.25 indicates that two perpendicular linear waves will propagate in the medium. The two terms with $Y_L$ in the denominator go to infinity and the result is that $\rho$ is either zero or infinity. Axes ratios of zero and infinity correspond to two linear waves that are aligned perpendicular to one another. An axis ratio of zero corresponds to alignment with the magnetic field and a ratio of infinity corresponds to alignment perpendicular to the B-field. These two waves will develop a phase difference between one another because of the different indices of refraction associated with the two modes. Two

orthogonal linear waves can be added to create a polarization state of any ellipticity, including the extremes of linearly or circularly polarized, depending on the relative phase of the linear waves. As a result the net polarization of the signal will oscillate between linear and circular polarization states when propagation can be described by QT propagation conditions.

In between the two extremes of parallel (QL) and perpendicular (QT) propagation with respect to the magnetic field a polarization ellipse that will change shape in the same manner as in the QT regime and also have its major axis rotated in the manner of Faraday rotation in the QL regime will result. Figure 2.4 shows the expected polarization states for either mode in the QT and QL regimes of propagation. Also shown is a polarization state in between the two extremes. The resultant polarization of the signal is shown in each case as well. In general the resultant polarization state can be thought of as a combination of propagation in the QL and QT regimes. As such, it is important to completely calculate the index of refraction and the polarization state of either mode when simulating the signal received at a satellite. The calculation of the final polarization state is explained in the following chapter.

# Chapter 3

# Ray Tracing

In order to predict the signal to be received by the RRI on ePOP, a software tool was developed to predict how radio waves propagate through the ionosphere. A computer program has been written at the University of Saskatchewan by Dieter Andre to perform ray tracing of EM waves through an ionized medium. The program solves the Appleton-Hartree equation for index of refraction presented in the previous chapter and then uses the Hamiltonian ray path equations as presented by *Haselgrove* [1963] to 'trace' the path of an EM wave through a plasma. The program is able to determine the path that an HF radio wave will take given a starting position and direction and an electron density profile within which to propagate.

For this thesis modifications have been made to this program to allow both the starting and ending locations of the wave to be considered. With this modification the program will iteratively search for the correct initial direction that will cause the ray to pass through the location of the satellite in space. The accuracy of this convergence method will also be examined. Additionally, another computer program was written to calculate the polarization state and all other wave parameters (i.e., propagation time, propagation distance, etc.) along the ray trace path. The ray tracing and analysis programs will be discussed in detail in this chapter. As well, the International Reference Ionosphere (IRI) modelling program will be discussed as a method for creating ionospheric $N_e$ profiles as a required input parameter to the ray tracing program.

## 3.1 Ray Tracing Formulae

The ray tracing program that will be discussed in Section 3.2 is based on the formulae given in *Haselgrove* [1963]. Using the Appleton-Hartree expression (Equation 2.26) for the complex index of refraction in a plasma, a set of equations was developed by *Haselgrove* [1963] to determine the direction a wave will take given a set of propagation conditions. If $F(\mathbf{k}, \omega, \mathbf{x}, t)$ represents the dispersion equation which is simply the Appleton-Hartree formula (Equation 2.26, the ray equations are given by [*Molcho and Censor*, 1986]

$$\frac{d\mathbf{x}}{dt} = -\frac{\partial F}{\partial \mathbf{k}} \Big/ \frac{\partial F}{\partial \omega} , \tag{3.1}$$

and

$$\frac{d\mathbf{k}}{dt} = \frac{\partial F}{\partial \mathbf{x}} \Big/ \frac{\partial F}{\partial \omega} . \tag{3.2}$$

Equation 3.1 indicates the group velocity of the wave in Cartesian coordinates and Equation 3.2 gives the change in the wave normal direction. Both these quantities are determined from the dispersion equation which is dependent on wave direction $\mathbf{k}$, frequency $\omega$, position $\mathbf{x}$, and, in the general case, time $t$. For the ray tracing performed with the Appleton-Hartree equation, all the variables at a set location are made to be unchanging with time, if not so already, and, as such, this implicitly includes the time dependence. The derivation of the *Haselgrove* [1963] expressions is quite complex so only the resulting equations will be reported here.

Using the notation from *Haselgrove* [1963] the variables $x_1$, $x_2$, and $x_3$ represent the displacement coordinates of the wave at a point along the ray path. The coordinates represent a Cartesian coordinate system with its origin at the centre of the Earth. The variables $u_1$, $u_2$, and $u_3$ represent a vector that is parallel to the wave normal and with a magnitude $u$ equal to the refractive index. $X$ is defined as in Chapter 2 and $Y_1$, $Y_2$, and $Y_3$ make up a vector $\mathbf{Y}$ that is parallel to the magnetic field and has a magnitude $Y = \omega_c/\omega$ as also given in Chapter 2. The variables $J$, $K$, $L$, and $M$ are introduced as intermediate calculation steps and are given by the

following equations,

$$J = 2[2(1 - X - Y^2)p + Y(1 + (\mathbf{v} \cdot \mathbf{u})^2)], \tag{3.3}$$

$$K = -2X(\mathbf{v} \cdot \mathbf{u})(pY - 1), \tag{3.4}$$

$$L = Y(1 - Y^2)p^2 - 2(1 - X - Y^2)p - Y, \tag{3.5}$$

$$M = 2Xp(pY - 1). \tag{3.6}$$

Where $\mathbf{v}$ is the unit vector of $\mathbf{Y}$ and $p$ is found from the solution to the quadratic equation

$$(1 - X - Y^2)p^2 + (Y(1 + (\mathbf{v} \cdot \mathbf{u})^2)p - (\mathbf{v} \cdot \mathbf{u})^2 = 0. \tag{3.7}$$

Using the dispersion equation (Appleton-Hartree) derived in Chapter 2 and Equation 3.1, the equation for calculating the direction a ray is going to travel given a starting location and direction is

$$\frac{dx_i}{dt} = Ju_i - KYv_i, \tag{3.8}$$

where $i$ represents a Cartesian coordinate. Equation 3.8 gives the derivative of one of the three spacial components with respect to some arbitrary step size (time or distance along the path) for each Cartesian coordinate. Calculating all three components of Equation 3.8 for a set step size gives the location in space of the next point along the ray path. This equation is the group velocity of the wave. Also needed is the change in the wave normal direction from one point to the next. This is calculated using the following equation,

$$\frac{du_i}{dt} = L\frac{\partial X}{\partial x_i} + \sum_j (Ku_j + MYv_j)\frac{\partial Y_j}{\partial x_i}. \tag{3.9}$$

Equation 3.9 will give the change in the wave normal direction from one point to the next on the ray path. This is necessary because the index of refraction is spatially anisotropic (i.e., it can be described by a tensor) and, as such, is dependent on wave direction. Notice that given a condition where there are no gradients in $N_e$ or magnetic field, the change in wave direction is zero as expected. The values that are obtained from Equations 3.8 and 3.9 are then used when calculating the conditions

for the next step along the path. These calculations are repeated for each step along the ray trace path until the required propagation distance from the transmitter is traced out.

## 3.2 Ray Tracing Software

### 3.2.1 Original Program

It was shown in Chapter 2 that the index of refraction in a magnetoionic medium is dependent on electron density and on the magnetic field strength and direction. Chapter 1 discussed how variable the electron density can be in the ionosphere. At typical HF radar operation frequencies, the propagating waves will be affected significantly by the ionosphere. In order to get a better understanding of radar wave propagation for instruments such as SuperDARN, the path a wave will take through the ionosphere can be modelled (ray traced) based on the equations presented in the previous section.

A computer program has been written at the University of Saskatchewan which performs ray tracing. This program, 'tracer.c' (see Appendix A), was written in the C programming language. The program takes as inputs: a 1-D or 2-D electron density profile, a starting location of the wave, a starting direction of the wave, and the radar frequency. The equations discussed in Section 3.1 are used to calculate the direction a wave will travel given a set of propagation conditions. The program will output the path a radar wave in the ionosphere will take with a point along the path being calculated roughly once every kilometre. The actual distance between points on a ray trace is dependent on the gradients in electron density. If there are large gradients, the program takes smaller steps, but if the gradients are very small, the program uses larger steps to more efficiently and quickly calculate the wave path. The program can trace both the ordinary and extraordinary modes. This is necessary because they will take different paths through the ionosphere as they have (typically slightly) different indices of refraction.

When a wave propagates through the ionosphere with a frequency that is comparable to the plasma frequency, it can be affected greatly. As an example, the plasma frequency associated with the F-region peak can be 9 MHz or higher, while the SuperDARN operating frequency can be anywhere from 8 MHz to 20 MHz, though more typically between 9 MHz and 16 MHz. Figure 3.1 shows ray paths through the ionosphere at various elevation angles. The horizontal axis is geographic latitude and the vertical axis is altitude. The transmitted frequency was set to be 15 MHz in this case. The $N_e$ profile that was used was a smoothly varying horizontally stratified profile with a peak density of $10^{12}$ m$^{-3}$, which gives a corresponding peak plasma frequency of 9.0 MHz. This profile is presented in Figure 3.2. Rays that are launched at an elevation angle less than $\sim 36^\circ$ are totally refracted back to the Earth. The rays just above this 'cutoff' elevation are greatly affected and travel a long distance before leaving the ionosphere. However, rays launched at much higher elevation angles are bent little when passing through the ionosphere.

One of the keys to obtaining an accurate representation of the path a wave will take is to have a reliable $N_e$ profile. The ray tracing program has the ability to take as input either a 1-D or a 2-D profile. The 1-D profile will be a listing of altitudes and their corresponding electron densities. This profile is horizontally stratified in that the program assumes the same density for all latitude and longitudes at a certain height. A simple and reasonably accurate method to obtain these 1-D profiles is to use the International Reference Ionosphere (IRI) model, which will be discussed in detail in Section 3.3. Two-dimensional profiles may also be used as input to the ray tracing program. For these profiles $N_e$ will be both a function of height and range from the transmitter. Any resolution of height and range can be used in the ray tracing program provided the user has the ability to develop the profiles (either from actual observations or the IRI modeller). The method used in this thesis to develop 2-D profiles is to take various 1-D height dependent profiles and align them in range from the radar. If the 1-D profiles that are aligned are similar enough, the result will be a smoothly varying 2-D profile. For this thesis, the resolution in altitude for the profiles was 1 km and the resolution in range was usually around one or two degrees

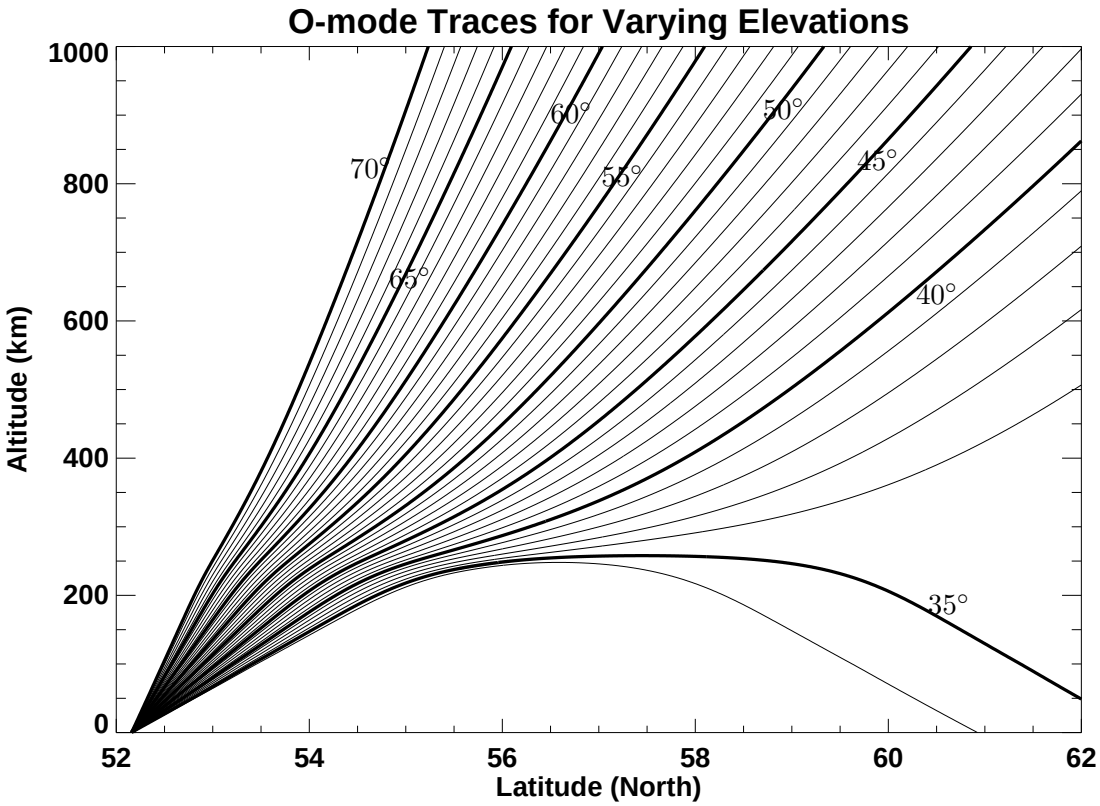


Figure 3.1: Various ray traces for the O-mode at different initial elevation angles (elevation angles begin at 34° and are spaced at 1° intervals). The transmitted frequency is 15 MHz and the peak plasma frequency is 9.0 MHz.

of latitude, which is ∼150 km to 300 km at satellite altitudes.

The second item that is important for good representative ray traces is the magnetic field of the Earth. In this ray trace program, the International Geomagnetic Reference Field (IGRF) model is used. This model is commonly used to model the magnetic field of the Earth [*Maus et al.*, 2005]. Unlike $N_e$ profiles, which are strongly dependent on time of day and season, the magnetic field is essentially constant at all times and, as such, it is not necessary to supply a specific magnetic field for a given time as it is with the electron density profile. The model magnetic field is sufficient to obtain a very good estimate of the actual field strength and direction.

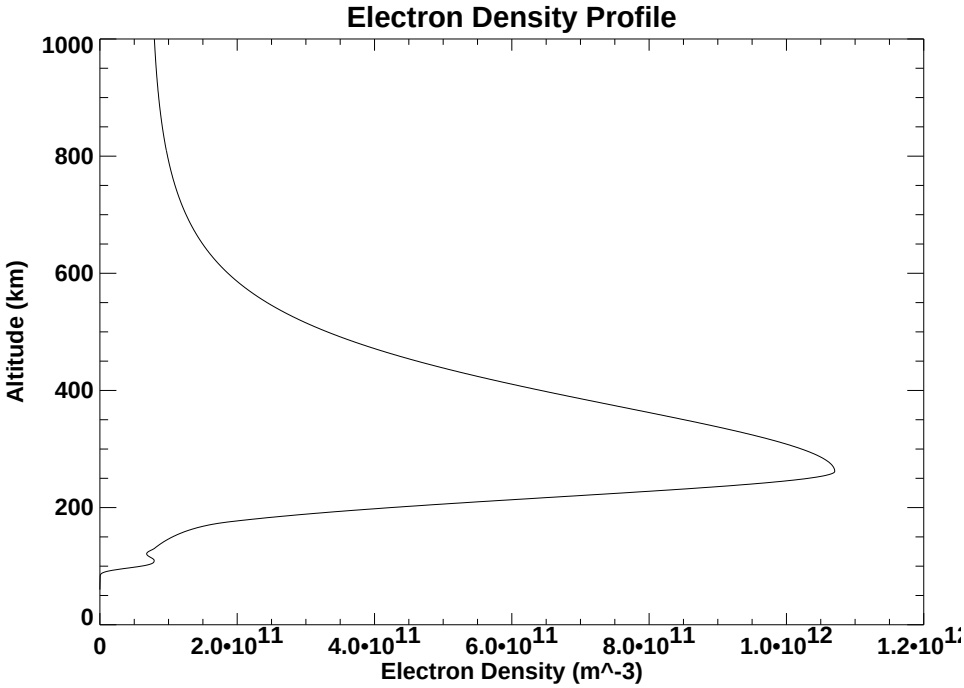


Figure 3.2: Electron density profile with an F-peak density of $10^{12}$ m$^{-3}$.

### 3.2.2 Modifications for Two-Point Solution of Ray Trace

One of the original purposes of the ray tracing software was to help understand how a wave of given characteristics will propagate through the ionosphere. An example is a study to examine conditions for obtaining SuperDARN echoes by determining where the radio wave became perpendicular to the magnetic field lines (irregularities that the SuperDARN wave scatters from are aligned with the magnetic field lines so echoes only occur when the wave is nearly perpendicular to these lines) [*Danskin et al.*, 2002]. With the incorporation of the RRI instrument on the Cassiope satellite to study transionospheric propagation, a new use was found for the software in the determination of the expected radar wave received by the RRI on ePOP. In order to use the ray tracing software to model the expected signal from SuperDARN at ePOP, the program needed to be modified to allow a traced ray to intersect with a desired location in space.

The convergence of a ray trace to the satellite location was performed using

a Newton iteration method [*James*, 2005a]. The two parameters the ray tracing program uses to specify direction are polar and azimuth angles. The polar angle is measured downwards from zenith and the azimuth angle is measured eastwards from due north with respect to the starting or transmitter location. A starting ray is traced with an initial polar angle $\alpha$ and azimuth angle $\beta$. This starting ray will reach the altitude of the satellite at a location with colatitude (90°-geographic latitude) and longitude coordinates $\theta_1$ and $\phi_1$, respectively. Then a second ray is traced with starting direction $\alpha+\triangle\alpha$ and $\beta$. This second ray crosses the altitude of the satellite at coordinates $\theta_2$ and $\phi_2$. A third and final ray is traced with a starting direction of $\alpha$ and $\beta+\triangle\beta$, which crosses the satellite altitude at $\theta_3$, $\phi_3$.

The next step was to look at the distances between the three traced rays. By calculating where the rays ended in relation to their desired position, a better guess of the starting direction is made. A correction to starting polar and azimuth angles was found by employing the following equations [*James*, 2005a]:

$$\triangle\alpha' = \triangle\alpha \frac{\phi_s - \phi_1 - \frac{\phi_1-\phi_3}{\theta_1-\theta_3}(\theta_s - \theta_1)}{\phi_2 - \phi_1 - \frac{\phi_1-\phi_3}{\theta_1-\theta_3}(\theta_2 - \theta_1)} \tag{3.10}$$

and

$$\triangle\beta' = \triangle\beta \frac{\phi_s - \phi_1 - \frac{\phi_1-\phi_2}{\theta_1-\theta_2}(\theta_s - \theta_1)}{\phi_3 - \phi_1 - \frac{\phi_1-\phi_2}{\theta_1-\theta_2}(\theta_3 - \theta_1)}, \tag{3.11}$$

where $\theta_s$ and $\phi_s$ are the colatitude and longitude of the satellite respectively. With these values calculated the program goes onto the next iteration. In the next step the starting $\alpha$ and $\beta$ values were set to $\alpha+\triangle\alpha'$ and $\beta+\triangle\beta'$ and the whole process was repeated. The iteration steps continued until the distance between a point on the traced ray and the actual desired location was less than the required convergence distance, which was usually set to be 10 m. In order to reach this accuracy, the method of convergence usually took only two or three iterations, provided a reasonable starting guess was made. In this case a reasonable starting guess usually meant that the initial ray path direction was within $\sim$20° elevation and azimuth of the correct starting direction. If the initial guess direction was not within this estimated range it would usually become immediately obvious as the program would diverge rapidly in search of an unattainable solution. If this occurred, it was a simple matter

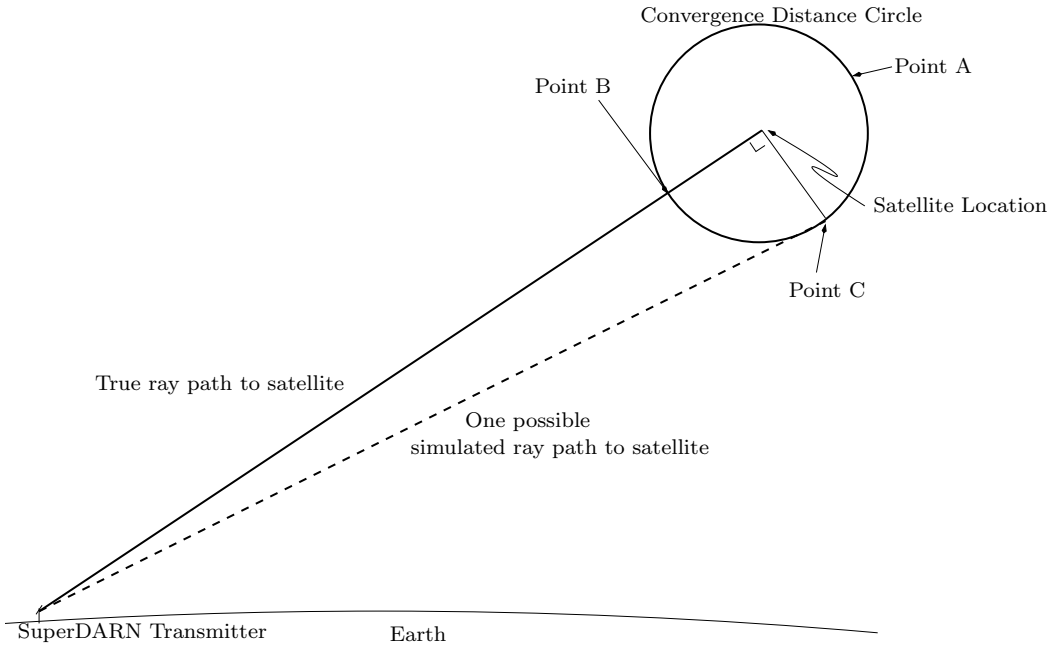


Figure 3.3: The geometry of the ray tracing shows that phase error is largest for simulated ray paths ending at points A and B and but very small for a ray path ending at point C.

to restart the program with a more reasonable initial direction.

There is a question as to whether converging a ray to within 10 m of the satellite was sufficient to give a useful answer. At an HF operating frequency of 15 MHz the wavelength in free space is 20 m. This means that the convergence distance was half of a wavelength at this frequency. If, for example, the O-mode and the X-mode were traced to opposite ends of the error range, the error in phase difference between the two modes would be $2\pi$. For propagation conditions where Faraday rotation dominates, a phase change difference of $2\pi$ will cause the orientation angle to go through one revolution. Therefore if the error in phase difference is greater than $2\pi$, the orientation angle information becomes ambiguous. Fortunately, this magnitude of error is not expected due to the method of convergence used. This is demonstrated in Figure 3.3.

In Figure 3.3 the ray path is shown as a straight line from the SuperDARN antenna array to the satellite location (in reality it is a curved path, but for this

explanation this aspect is not of importance). The circle around the satellite represents the convergence distance. If a point on the ray trace falls anywhere in this circle, the convergence criterion was satisfied and the program completed. The phase a wave goes through is directly dependent on distance travelled. It can be seen that the difference between the real phase path and the simulated phase path could be quite large if the closest point on the ray path was near the front or back of the convergence circle (points A or B in the diagram). Interestingly, this result will never occur due to two characteristics of the ray trace process. First, near the satellite altitude the distance between calculation points on the ray path was set to be very small (<10 cm). Secondly, the ray path length was set to be much longer than the path to the satellite (i.e., the program will always try to go past the satellite). The former characteristic of the program assures that many very short path length 'point' calculations occur close to the satellite position, while the latter characteristic assures that the path calculations occur both before and after the location of the satellite. As a result of this the closest point to the satellite location on any given ray path will be essentially along a line that goes through the satellite and point C (see Figure 3.3). Even if the closest point is at C on the circle (which is the worst case scenario), the phase error is going to be very small. As the ray path is on the order of thousands of kilometers, the distance that is travelled by the simulated ray path will be almost equal to the actual distance a ray would take to meet up with the satellite.

To develop an idea of how accurate the ray tracing program is in determining phase, several ray paths need to be calculated in close proximity to each other. Since each ray path is traced independently the variation in phase difference between the O- and X-modes from one convergence point to the next will indicate the accuracy of the program in regards to calculating phase difference. The random variation of phase difference from one latitudinal point to another should be quite small even when large convergence distances are used given the reasoning from Figure 3.3 and this is indeed the case as shown below.

An examination of the random phase variation due to the numerical nature of the

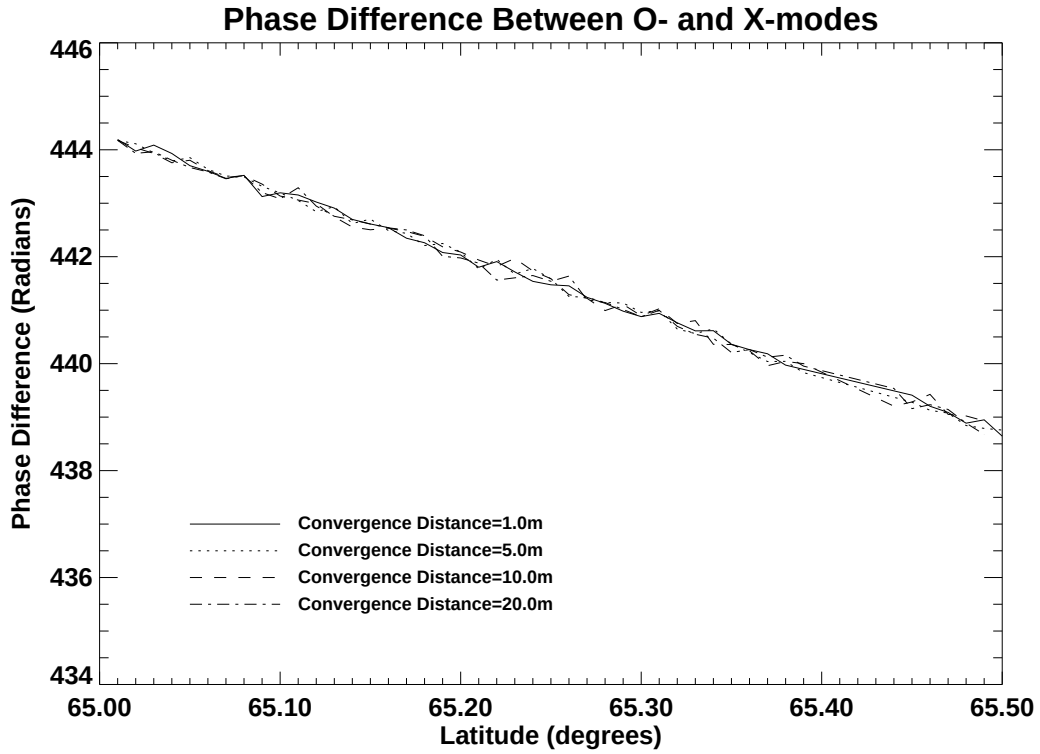


Figure 3.4: Phase difference between O- and X-modes for convergence distances of 1 m, 5 m, 10 m, and 20 m.

calculations for various convergence distances was performed. The phase difference between the modes was calculated for each ray trace and if it showed little random variation over this distance (at worst, less than $2\pi$ to remain unambiguous) then it was known that the convergence distance in question was acceptable. This test was carried out for convergence distances of 1 m, 5 m, 10 m, 20 m, 50 m, 100 m, 500 m, and 1000 m. The phase differences between the two modes as a function of latitude are shown in Figures 3.4 and 3.5. From inspection of these figures it be seen that for convergence distances up to 100 m the random variation in phase difference is less than one radian. At 500 m the error between ray traces becomes quite large (greater than $2\pi$). Therefore, a convergence distance of 10 m was sufficient to obtain reliable simulation information.

The ray tracing program converges both the O- and X-modes to the satellite location in space. To accomplish this, slightly different initial ray directions are used

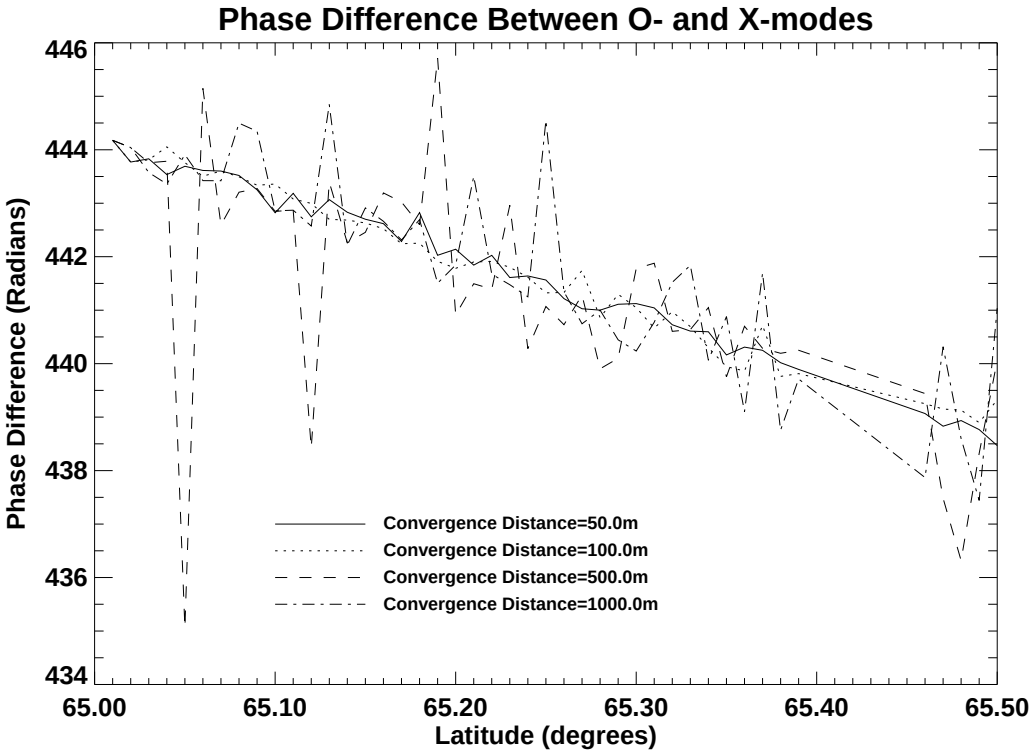


Figure 3.5: Phase difference between O- and X-modes for convergence distances of 50 m, 100 m, 500 m, and 1000 m.

for either mode. Figure 3.6 demonstrates this process. It should be noted that the angle between the arriving O- and X-modes, shown as $\theta$ in the figure, is in fact quite small for all ray tracing simulations considered here. The difference in arrival direction of the two modes is typically of the order of less than $\sim 0.1^\circ$ at 15 MHz and $\sim 0.3^\circ$ at 9.3 MHz. As such, the difference in the angle of arrival of the O- and X-mode waves at the satellite is negligible and need not be considered.

### 3.2.3 Analysis of Polarization State

All that has been discussed so far is the path that the wave will take through the ionosphere from the transmitter to the satellite, there is no information about the properties of the received wave. When characterizing the signal received by the RRI, there are a couple factors to consider. There will be polarized and unpolarized

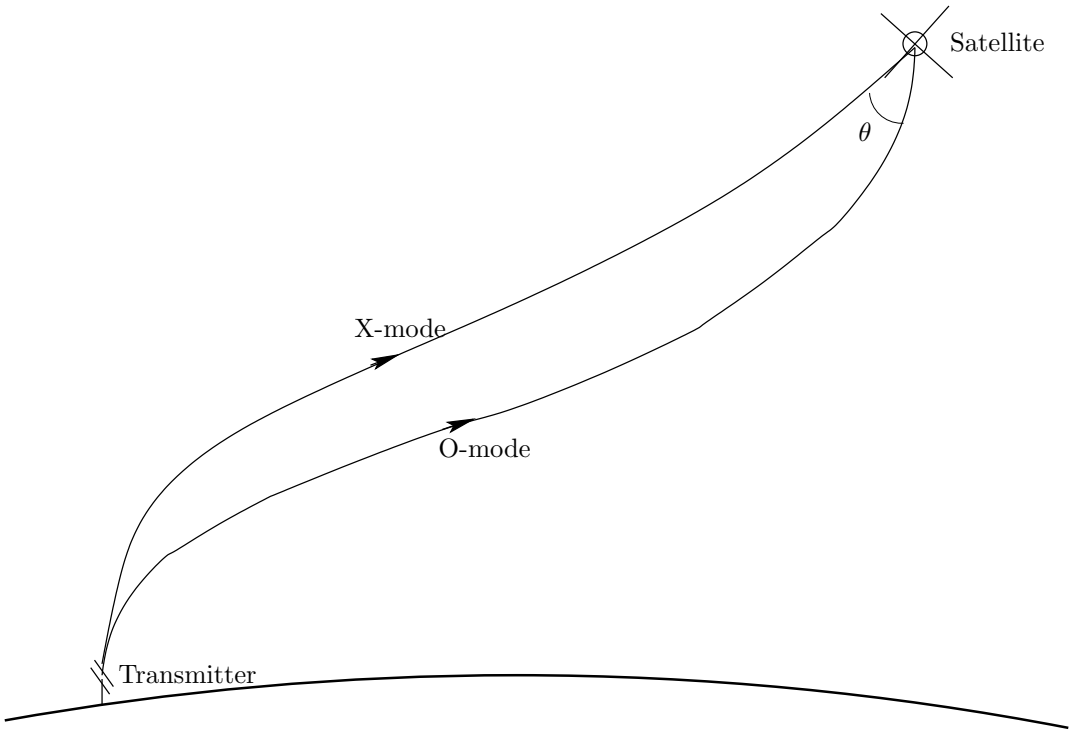


Figure 3.6: The two modes must travel different paths from the transmitter on the ground to the satellite receiver. The angle between the O- and X-mode arrival directions ($\theta$) is excessively exaggerated in this figure. Typically, this angle is of the order of $\sim 0.1^\circ$ for a 15 MHz wave and thus is neglected.

portions of the signal. For this research only the polarized portion of the signal has been studied, as the unpolarized portion is expected to be small. Also, the power of the signal was not considered in this study. In future work both the unpolarized portion and power of the signal should be examined.

To obtain this additional information an IDL program called 'rayanalyze.pro' (see Appendix B) was written to determine the polarization state of the signal from a calculated ray path. As was shown in Chapter 2, the polarization of an EM wave in a magnetoionic medium is dependent on several different factors. The angle that the wave vector makes with the magnetic field lines will determine if the propagation may be characterized as QT, QL or somewhere in between. The electron density will also affect the index of refraction and the separation between the modes. Another parameter of importance is the initial polarization state of the wave at the trans-

mitter. This section will give an overview of the calculation of the final polarization state expected to be detected by the receiver on the satellite.

The first step was to define the initial state of the wave at the transmitter. Both the SuperDARN array to be used with the RRI on ePOP and the Northridge transmitter used for the ISIS II transionospheric experiments produce waves of roughly the same polarization state at the ground. In both cases the starting polarization state was a linear wave that was oriented in the east-west direction parallel to the earth. In the coordinate system outlined in Chapter 2, this would result in a polarization state with an electric field of the form

$$\mathbf{E}_o = E_o \widehat{y}. \tag{3.12}$$

The external B-field is oriented in the $xz$ plane and, as such, is therefore perpendicular to the starting polarization state. This geometry is demonstrated in Figure 3.7.

When a wave is launched into the ionosphere, the polarization state will be affected according to Equation 2.25. The first point along the ray path in the ray path simulation sees the horizontally linear wave split into the two different modes (O- and X-modes). The only polarization states that are allowed to propagate in a magnetoionic medium are given by the equation for $\rho$, Equation 2.25. Therefore at this first step the program splits the wave into two (orthogonal) ellipses with different senses of rotation about the magnetic field. These two ellipses represent the O and X propagation modes. The program then calculates the relative strengths of these modes based on the initial polarization state at the beginning of each step. Equation 2.25 guarantees that the two propagation ellipses it describes are always orthogonal to one another. Much the same way a vector can be resolved into orthogonal $x$ and $y$ components, a given polarization state can be resolved into two orthogonal ellipses. However, these two polarization ellipses have different indices of refraction as given by Equation 2.26 and will therefore travel along typically similar, but slightly different paths, to reach the satellite location. Note that for low enough frequencies, low elevation angles, and/or high electron densities the modes can have significantly different paths. In the modelling program, each mode was followed

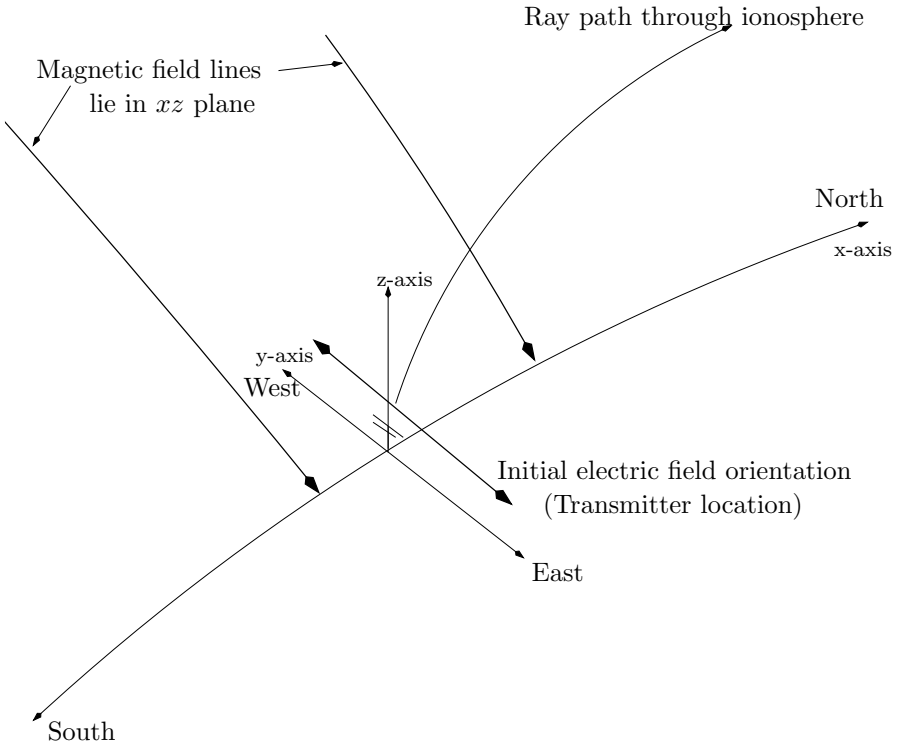


Figure 3.7: Geometry of initial polarization state with respect to the external magnetic field lines shows that the electric field polarization is initially perpendicular to the magnetic field lines.

and analyzed separately and at the point where they intersect at the satellite, the polarization states of the modes were added together.

At the second point along a ray path the mode that was being followed will encounter slightly different conditions than at the previous point. As a result of this the polarization ratio of Equation 2.25 will change slightly and the ellipse that entered this region will need to be modified (i.e., it is split into the two orthogonal polarization states that are able to propagate in this step) in order to propagate in these conditions. The same step was performed as when the original polarization state was decomposed into its two orthogonal (or mode) components, except now one of the ellipses has a very small relative magnitude because the conditions were nearly the same as the previous step. In other words, the conditions of propagation have changed little so the required shape of the ellipses changes little also. The small ellipse was not the mode of interest and was discarded while the larger ellipse

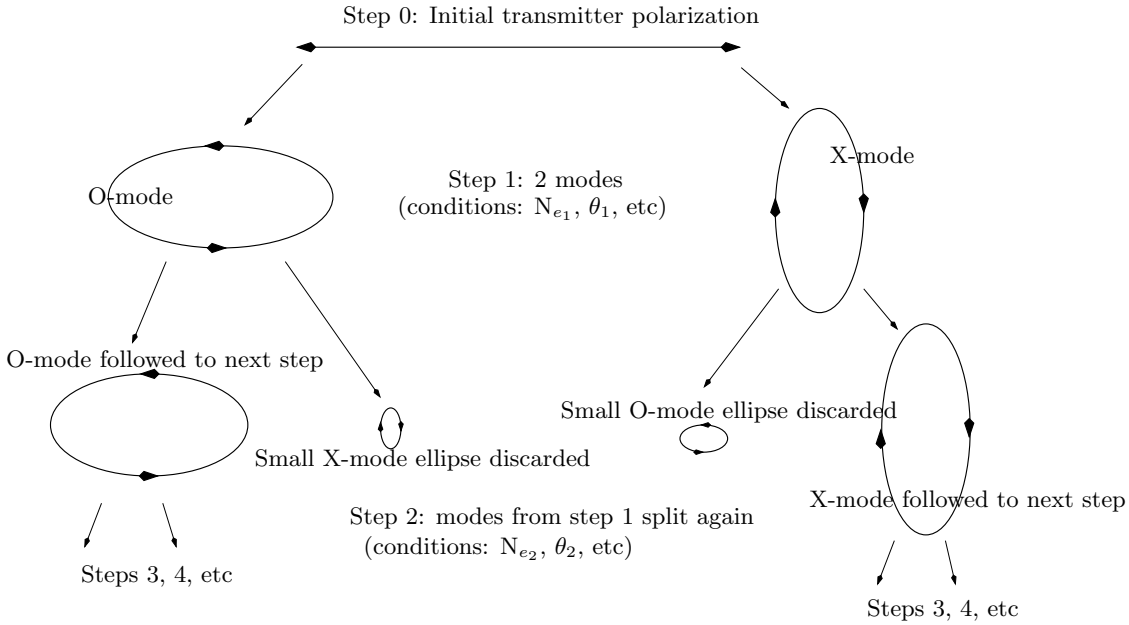


Figure 3.8: The polarization ellipse shapes at each step in the ray tracing program. Horizontal linear polarization splits into two elliptical polarization states. At each point two more ellipses are found with one being insignificant and discarded.

of interest was carried on to the next step. At each subsequent step, this process repeats itself for each mode until the location of the satellite was reached. A diagram to better understand this process is shown in Figure 3.8.

Once the final polarization of both modes is found at the satellite location, the accumulated phase difference between the modes is calculated. The phase difference is calculated by summing over each step along the ray path using

$$\phi_{dif} = \frac{\omega}{c}(\sum^{i}(n_{oi}l_{oi}) - \sum^{j}(n_{xj}l_{xj})), \tag{3.13}$$

where $n_{oi}$ and $n_{xj}$ are the indices of refraction for the O- and X-modes at a given step ($i$ or $j$) along the ray trace, $l_{oi}$ and $l_{xj}$ are the path lengths between steps on the ray path, $\omega$ is the angular radar frequency, and $c$ is the speed of light in a vacuum. Other parameters were calculated such as time delay ($t_d$) and the difference in path length ($d$) between the modes. These are calculated as follows:

$$t_d = \frac{1}{c}(\sum^{i}\frac{l_{oi}}{n_{oi}} - \sum^{j}\frac{l_{xj}}{n_{xj}}), \tag{3.14}$$

and

$$d = (\sum^{i} l_{oi} - \sum^{j} l_{xj}). \tag{3.15}$$

By using the accumulated phase difference and the shapes and sizes of the two polarization ellipses, the final polarization state of the wave at the satellite location was calculated. The accumulated phase difference was added to the O-mode and then the two mode ellipses were decomposed into $x$ and $y$ components separately. These components were then added together by complex arithmetic and the final polarization state of the wave was found.

## 3.3 International Reference Ionosphere Profiles

### 3.3.1 IRI Background

One of the most important components for performing the numerical ray tracings was the inclusion of an electron density ($N_e$) profile. The $N_e$ profile that a radio wave propagates through is the primary modifier of the ray path. To develop realistic $N_e$ profiles for the ionosphere a dependable modelling program was needed. The standard for ionospheric parameter specifications is the International Reference Ionosphere (IRI) model. The COmmittee On SPAce Research (COSPAR) recommends the IRI model for use in ionospheric modelling [*Bilitza*, 2001]. A joint working group of COSPAR and the International Union of Radio Science (URSI) developed and continually improves the IRI model.

The IRI model delivers several parameters such as electron and ion densities, temperatures, and drift velocities. The main interest in radio wave propagation studies using ray tracing is, of course, the electron density. The best method of determining these quantities is from experimental data. Using various ground ionosondes and satellite topside sounders that have been active for several years a large data base of information has been collected. Whenever possible this data is used for the IRI model, however gaps in data do exist and are filled based on theoretical considerations as best as possible.

As was mentioned in Chapter 1, the main driver of ionospheric densities is the Sun. The EUV wavelength part of the solar spectrum contributes to ionospheric formation. However, the EUV index cannot be observed for prolonged periods of time or on a global scale because it is absorbed by the atmosphere. As a result the two indices that are used in the model are the global ionospheric index ($IG_{12}$) and the 12-month running mean of sunspot number observed from the Zurich observatory ($R_{Z_{12}}$). This is a measure of the number of sunspots visible from this observatory. The sunspot number is strongly correlated to the ionospheric density provided the number is not too high. If $R_{Z_{12}}$ becomes larger than about 150, it has been seen that the ionospheric density becomes saturated and does not rise accordingly. This is the reason that the $IG_{12}$ index is brought in. $IG_{12}$ is an index based on various ionosonde stations around the globe. The $IG_{12}$ index is used to model the F-peak density and the $R_{Z_{12}}$ index is used for the F-peak altitude and topside profile. Since the two indices that the modelling is based on are monthly averages, daily and hourly measures of $N_e$ can be quite different than the model predicts.

### 3.3.2 IRI Use

The IRI program is very user friendly. The program can either be downloaded for use or users can query for results directly from the IRI website (`http://modelweb.gsfc.nasa.gov/models/iri.html`). Whichever method is being used, there are several items that are required to obtain an electron density profile. The year, day and time (either UT or LT) must be supplied. As well, the location on earth of the $N_e$ profile in either geographic or geomagnetic coordinates is required. The final required input is the initial and final heights along with the height step size. There are several optional items that can be entered such as sunspot number, ionospheric index, F-region peak density, or F-region peak altitude. The F-peak density and altitude are useful to enter if there is something like an ionosonde operating at the location of interest. If the F-peak density is known the program will scale the calculated $N_e$ profile based on the peak value that is supplied. The altitude range of the IRI profile used for the ray path simulations is from 60 km to 2000 km. This range is sufficient

for the satellites of interest in this thesis.

The IRI output is a collection of variables given as a function of altitude. For profiles used in this thesis the altitude step size was 1 km with an altitude range as stated immediately above. The parameters that are supplied by the IRI model at each altitude are electron density, neutral temperature, ion temperature, electron temperature, and ion percentages of $O^+$, $N^+$, $H^+$, $He^+$, $O_2^+$, and $NO^+$. Only the $N_e$ profiles were of interest in the current thesis. As the output of the IRI model is a one dimensional $N_e$ profile, 2-D profiles were created by combining several 1-D profiles.

# Chapter 4

# ISIS II Analysis

The major goal of this thesis was to model the signal that will be received by the RRI instrument on the ePOP satellite from ground transmitter stations. The validation of the model was greatly assisted by comparing it with the data set from the ISIS II satellite. In 1978 the ISIS II satellite had a transionospheric experiment with a number of similarities to the proposed RRI experiment on ePOP. There are a number of benefits to analyzing the ISIS II data and comparing it with the ray tracing model presented in the previous chapter. The first is for validation of the ray tracing model using actual data. A good understanding of the capabilities of the model will be of significant assistance in interpreting the data collected by the RRI on ePOP. Furthermore, it allows for the testing of the ability of the model to predict the wave polarization state received at the satellite. ISIS II only had a single dipole antenna; however, the RRI on ePOP consists of a pair of crossed dipoles with the ability to receive full polarization information.

In this chapter, the ISIS II mission is presented, and the data from this transionospheric propagation experiment is analyzed. The ray path simulations, which model the received signal at ISIS II using the developed software discussed in Chapter 3, are then discussed. Finally, these simulations are compared to observed data.

## 4.1 ISIS II Mission

The ISIS II satellite was one of the pioneers in studying the ionosphere of the Earth. ISIS II was launched in 1971 and operated in some capacity until 1990. The satellite was placed in a nearly circular orbit at ∼1400 km altitude [*James*, 2005a]. The

inclination of the orbit was 89°, meaning that it orbited in a plane set 89° from the equator. The satellite itself was spun at ∼3 rpm to maintain stability, resulting in one spin every 20 s.

One of the main instruments on the ISIS II satellite consisted of a radio transmitter/receiver connected to an 18 m tip-to-tip dipole antenna. This antenna was used to transmit and receive HF radio signals. The main goal for this antenna was to perform $N_e$ measurements of the topside portion of the ionosphere. In this mode the satellite created hundreds of topside profiles (ionograms) per orbit. A secondary objective of the antenna was to operate in a passive receiving mode. In this transionospheric mode the antenna would receive signals from a dedicated ground transmitter, of which there were several located over the globe. Interlaced with the receiving portion of a transionospheric pass were several topside scans. The transionospheric data that was studied here is from the Northridge transmitter that was located in Ottawa, Canada. The data were recorded from June and July of 1978.

The Northridge transmitter sent out a radio wave at 9.303 MHz and had a power output of 1 kW [*James*, 2005a]. The transmitter consisted of two perpendicular dipoles fed in phase and oriented northwest-southeast and northeast-southwest. This created a polarization state that was linear, horizontal to the earth, and roughly perpendicular to the geomagnetic field lines. The transmitter operated as a pulsed radar system, modulated with a square wave pulse at a pulse repetition frequency of 180 Hz and a 50 percent duty cycle. This meant the transmitter was sending a constant pulse for ∼2.8 ms and then it turned off for the same period of time. The transmitter operated in this mode for about 25 s at a time, then it completely turned off and the satellite began a topside sounding for about 20 s, after which the transmitter would turn on for ∼25 s and so on. In this configuration, the topside sounding mode supplied $N_e$ measurements which were used to constrain the ray tracing model. The next section will discuss in detail how the signal was recorded and some of the interesting features that were observed in the signal.

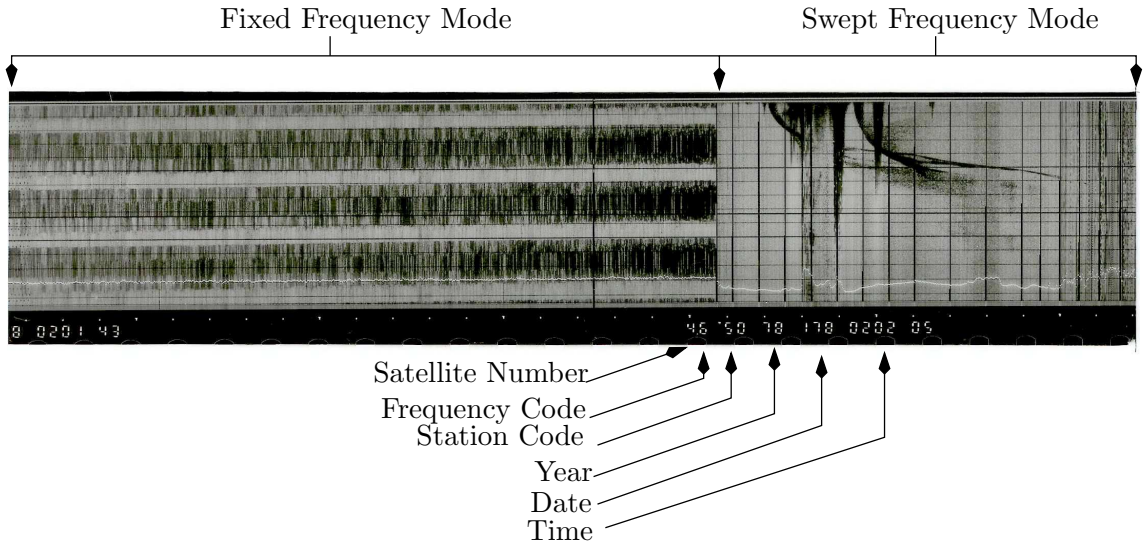


Figure 4.1: Example of ISIS II film data. "White" on the film represents no signal while the darker the markings the stronger the received signal. The fixed frequency or transionospheric portion of the data is observed as the three or four horizontal bars on the left of the frame. The swept frequency or topside scan is presented on the right. Data is from the pass on June 27, 1978 at ∼2:02 UT.

## 4.2 Transionospheric Data From ISIS II

### 4.2.1 Film Data Explanation

The radio signal that was received by the ISIS II satellite was sent down with the satellite telemetry to a ground receiving station. At this station, the signal was recorded onto 35 mm film. The film data is physically available for study at the Communications Research Centre (CRC) in Ottawa and other locations. Due to the physical limitations of studying rolls of film data, the information is in the process of being digitized and placed online for study (`http://cdaweb.gsfc.nasa.gov/cdaweb/pre_istp/`). All the data presented and analyzed in this thesis were from the digitized data set.

An example of film data is shown in Figure 4.1. When examining the data one observes two sets of signals interlaced together. The fixed frequency portion of the data appears as three horizontal dark bars or bands of signal. In reality, there

were four bars of signal recorded in a vertical stripe, however in most cases the film has been cut so that only three and a portion of a fourth bar are observable. The bars represent the received signal from the 180 Hz square pulses transmitted from Ottawa. The signal was recorded from top to bottom and left to right. The time for recording one vertical strip was set so that the instances of pulse arrivals would line up horizontally and create straight bars. In this way, structure in the signal that occurs on the order of seconds can be read across the horizontal, and structure on the order of milliseconds, or on the order of the individual pulse length, can be observed in the vertical direction. Figure 4.2 demonstrates how the film was analyzed. If signal amplitude is plotted as a function of time down a vertical slice (cross section), the individual pulses are observed. If, however, signal amplitude is plotted as a function of time from a horizontal slice (left to right), one observes a continuous section of received signal.

Returning to Figure 4.1, the white dots at the bottom of the film correspond to one second intervals. To the right of the fixed frequency portion of the film is the swept frequency mode. This is represented by lines of signal coming down from the top and proceeding to the right. The topside sounding portion of the film is useful in determining the $N_e$ profile in the ionosphere from the altitude of ISIS II down to the F-region peak ($f$oF2). How this is accomplished will be discussed in Section 4.3.1.

### 4.2.2 Signal Features

When the transionospheric or fixed frequency portion of the data was studied, several features were noted. For the most part, the signal that was received from the transmitter over Ottawa behaved as one would expect. There was weak and somewhat noisy signal near the edges of the pass, where the satellite had almost passed over the horizon (descending node) or was just coming up from the horizon (ascending node). When ISIS II was nearly overhead of Ottawa strong signal was observed. The strong signal was evident as simply four dark horizontal bars representing the square wave pulses. For most of the passes this was the behaviour of the signal in general, but in some cases interesting features appeared in the signal structure.

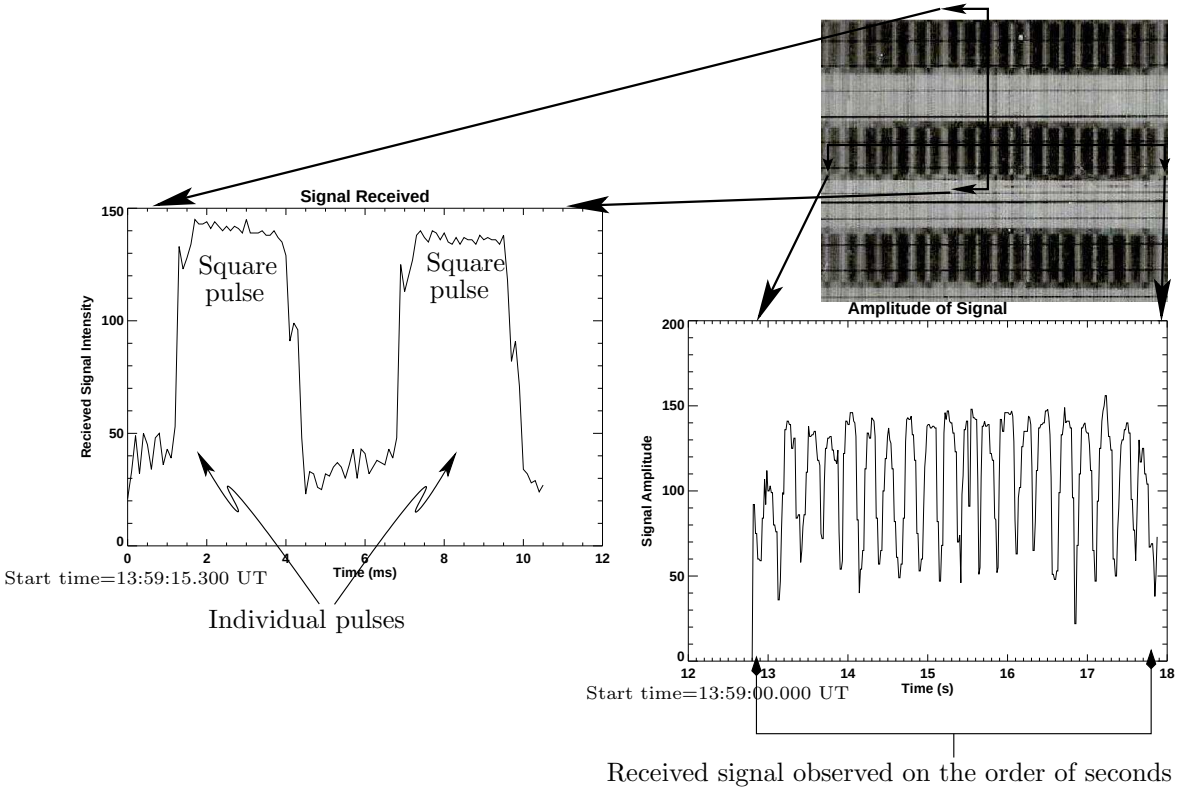


Figure 4.2: A small section of the transionospheric propagation portion of the film. Features in the individual pulses, with a time scale on the order of ms, are observed from a vertical cross section of the film data. Features on the order of seconds are observed from a horizontal cross section. Data shown was recorded on July 3, 1978 at 13:59 UT.

The first feature noticed upon examining a few passes was that for large periods of time, the signal appeared slowly and periodically to fade in and out. This fading rate was $\sim$0.1 Hz and was observed for the portion of a pass where the satellite was north of the transmitter. An example of this type of signal is presented in Figure 4.3. The reason for this type of fading was the spacecraft stability rotation. As mentioned, the ISIS II spacecraft was spun at approximately 0.05 Hz (3 rpm). In the northern portion of the pass, the spacecraft was spinning in such a way that it rotated the dipole so at a certain time the dipole was almost parallel with the line of sight to the transmitter and, as such, little or no signal was received (i.e., the Tx on the ground was looking at the end of the Rx antenna on the satellite). A short time later after

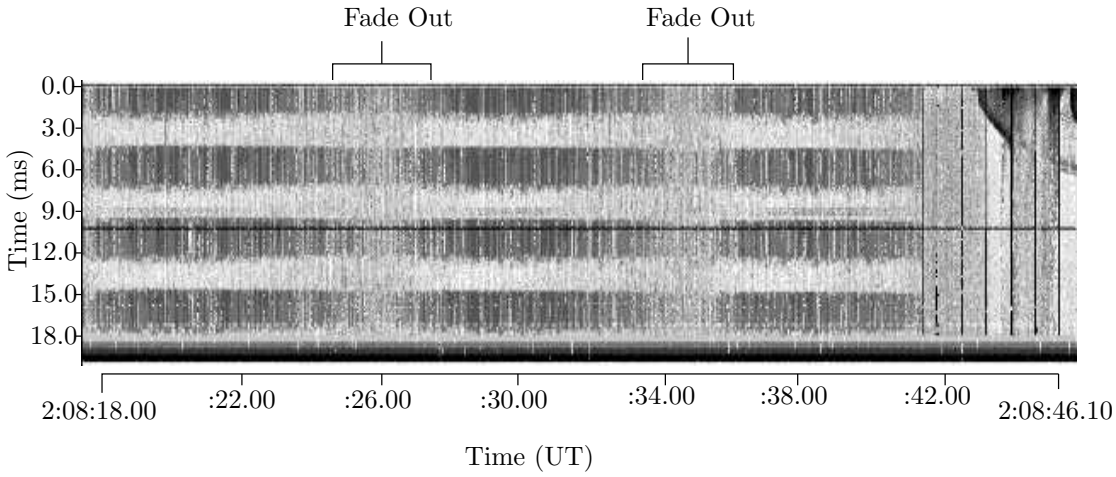


Figure 4.3: Periodic fading of the received signal was observed at a rate of about 0.1 Hz. The fading was caused by the spacecraft stability rotation. Data is for the pass on July 3, 1978. Time in UT is shown on the $x$-axis.

half a rotation (10 s), the dipole would be perpendicular to the line of sight to the transmitter and a strong signal would be recorded (i.e., the Tx on the ground was looking at the whole length of the Rx antenna on the satellite). There was no slow fading observed to the south of the transmitter as the spacecraft orientation changed such that the dipole antenna on the satellite was always aligned perpendicular to the line of sight of the transmitter despite the stability rotation. The orientation of the antenna on the spacecraft with respect to the transmitter on the ground is further clarified in Figure 4.4.

In the region to the south of the transmitter, a different type of periodic fading was observed. In some of the passes there were instances of periodic fading at a much faster rate than the stability rotation fading. An example of this appears in Figure 4.5. This periodic fading is attributed to Faraday rotation of the wave as it propagates through the ionosphere. The wave started out as linearly polarized and oriented east-west at the transmitter, but as it travelled up through the ionosphere its orientation relative to the magnetic field of the Earth, which remains roughly the same, changes due to Faraday rotation. The observation of this effect is expressed by the orientation angle, $\psi$, which was discussed in Chapter 2. When a wave reached the

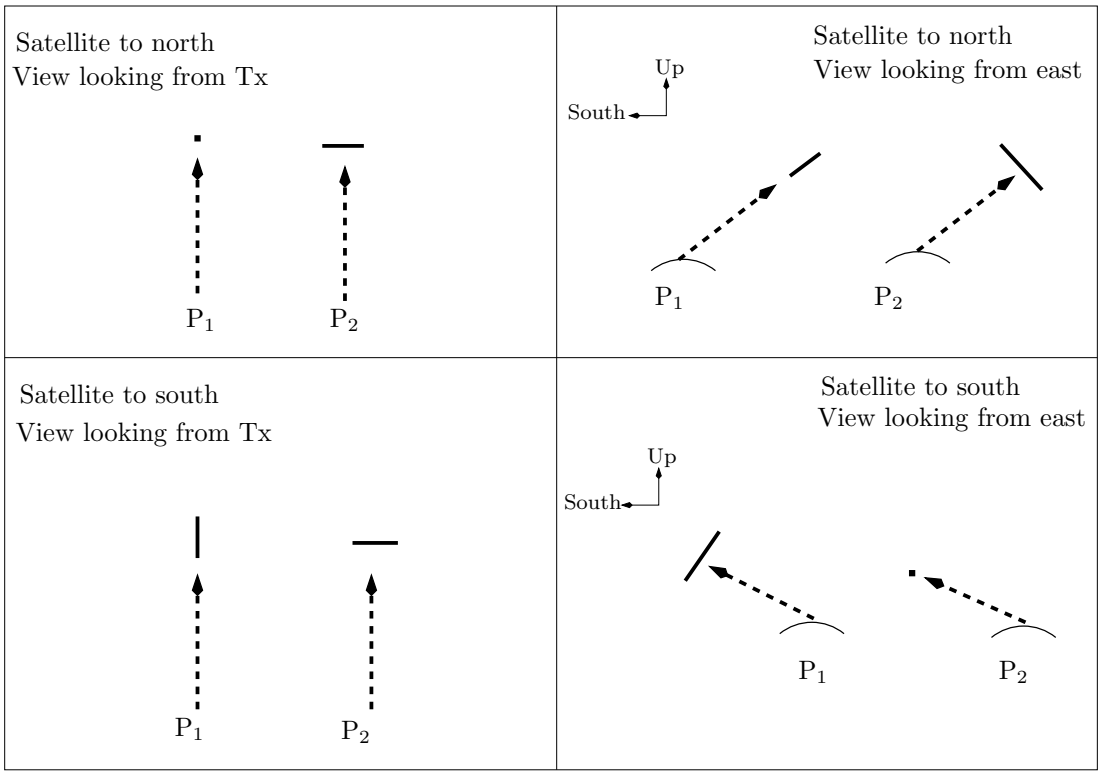


Figure 4.4: Various orientations of the dipole axis (solid line) with respect to the transmitted wave direction (dashed line). $P_1$ and $P_2$ correspond to two satellite antenna orientations separated by 10 seconds. The dots represent the view of the end of the dipole. The top left panel indicates the extreme orientations (idealized) of the dipole that is encountered by the wave when the satellite is in the north — either the end of the dipole or the full dipole depending on the satellite orientation at the time. The bottom left panel indicates the extreme orientations of the dipole as viewed from the transmitter when the satellite is in the south — a full dipole at all times. The right panels show the orientations from the point of view of an observer situated east of the transmitter-satellite pair.

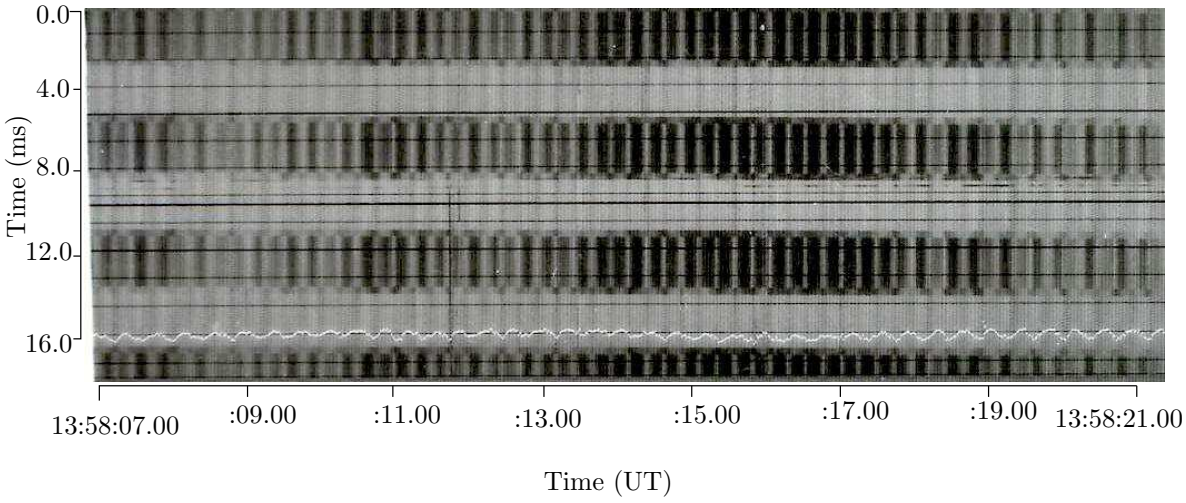


Figure 4.5: Periodic fading of the received signal is observed at a rate of ∼4 Hz. This fading is caused by Faraday rotation of the linear propagating wave as it is received by ISIS II. Data is for the afternoon pass on July 3, 1978. Time in UT is shown on the $x$-axis.

satellite it typically had completely rotated several times and its orientation angle could be anywhere between 0° and 180°. If the orientation angle was such that it was nearly parallel to the spacecraft dipole, a strong signal was recorded. As the satellite moved in the sky, the Faraday rotation a received wave underwent was dependent on its path to the satellite, which was in turn dependent upon the position of the satellite. As a result, the orientation angle received at ISIS II changed as the satellite travelled. When it changed by 90° compared to the parallel alignment case, it was perpendicular to the dipole axis and little or no signal was received. As the satellite progressed further, the polarization state Faraday rotated more and eventually it was aligned with the dipole again and a strong signal was again recorded. This resulted in a periodic fading of the recorded signal. This type of signal fading has also been studied during rocket flights through the ionosphere [*James and Calvert*, 1998].

Another signal characteristic which was often observed in a significant number of the passes was differential mode delay. When an HF wave propagates through the ionosphere it splits into the O- and X-modes (see Chapter 2), which have different indices of refraction. This means that the time it takes for one mode to reach the

satellite will be different than the time for the other mode. This results in an often noticeable separation in time between the recording of the O-mode portion of a pulse and the recording of the X-mode portion. This is called differential mode delay [*James*, 2005]. An example of differential mode delay can also be observed in the data presented in Figure 4.5. Above and below the portion of signal that was attributed to Faraday fading, two narrow bars of signal may be observed which do not periodically fade. The signal on the top of each bar represents the O-mode only signal and it arrives at the satellite first. Next comes the portion of signal where both modes are observed together. It is known that this is a combination of both modes because there is very evident Faraday fading occurring. The final part of the signal, at the bottom of a band, is the portion of the signal where only the X-mode signal is being received at the satellite as the O-mode portion of the pulse has completed. Faraday fading and mode delay are further discussed in Figures 4.6 and 4.7. In Figure 4.6 a typical vertical slice of a bar presented in Figure 4.2 has been plotted. Notice that at the beginning and end of each pulse the signal is at a much lower amplitude, representing the signal as received from the individual modes only due to mode delay. Figure 4.7 shows a horizontal slice of a bar to demonstrate the periodic fading of the signal from Faraday rotation.

A further type of fading was observed but not considered in this thesis. This is the fading of a single mode. The cause of this fading is due to interference effects of either only O-mode waves or only X-mode waves following two or more distinct paths to reach the satellite. The result is an interference pattern produced in the single mode portions of the data. A single mode arriving at the satellite from two paths will only occur in the case of $N_e$ enhancements or depletions acting like a lens to focus the rays. Considerations of $N_e$ enhancements or depletions of this type were not done in this thesis work. This fading is discussed in detail by *James*, [2003]; *James*, [2005a]; and *James et al.*, [2005b]. The self-fading of the modes can be observed in Figures 4.2 and 4.5.

From the study of several satellite passes it was noted that the various signal characteristics only occurred during specific portions of a pass. As was mentioned,

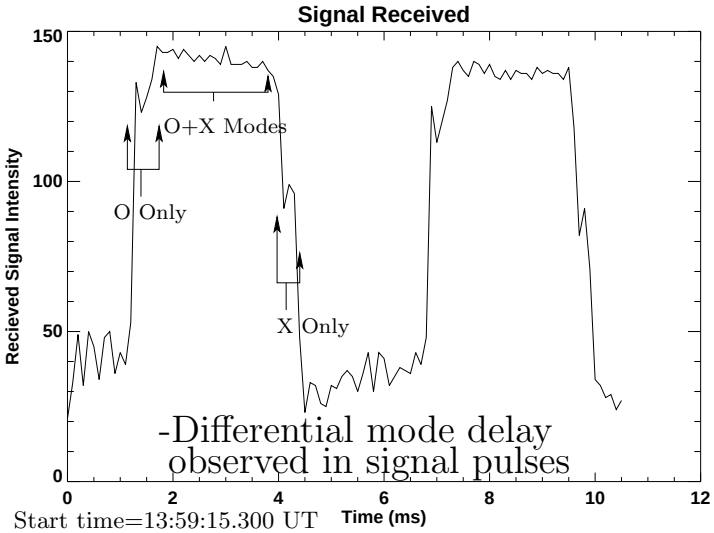


Figure 4.6: In the individual signal pulses, delay between the arrival of the modes at the satellite is observed. Data is from the pass on July 3, 1978.

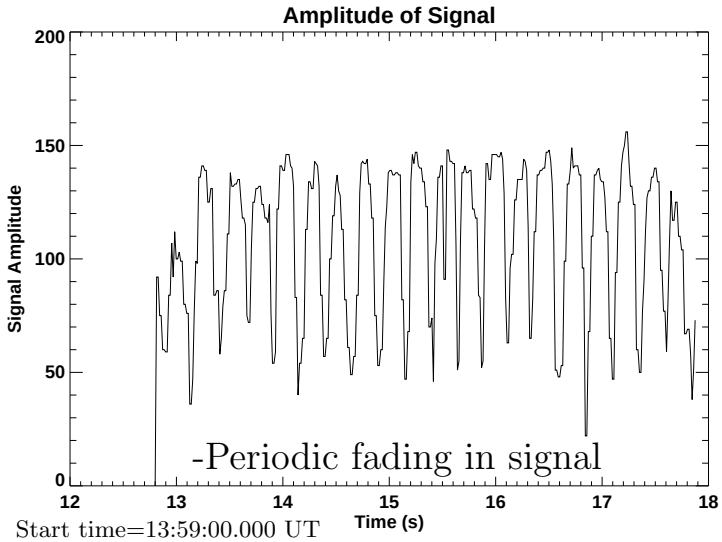


Figure 4.7: When several seconds of film data is examined, periodic Faraday fading of the signal is observed. Data is from the pass on July 3, 1978.

the slower fading due to spacecraft stability rotation only occurred north of the transmitter simply due to orbital mechanics. The differential mode delay and the periodic Faraday fading were both found predominantly to the south of the transmitter. Sometimes they occurred directly overhead, but never to the north of the transmitter in this data set. The probable reasons for this are that the difference in indices of refraction for the two modes becomes larger both when the electron density is higher, as it is to the south due to stronger photoionization, and when the geometry of the propagating waves is best described by QL propagation. Both of these factors occur for propagation to the south of the transmitter. Recall from Chapter 2 that quasi-longitudinal (QL) propagation describes a wave which is travelling roughly parallel or anti-parallel to the external B-field lines, while quasi-transverse (QT) propagation describes a wave propagating roughly perpendicular to the external B-field lines. The reason for the wave being more QL to the south is shown in Figure 4.8. Also, as was explained in Chapter 2, Faraday rotation only occurs when the wave is propagating in the QL direction. In the north, the propagation was more QT and Faraday rotation did not occur. When there is QT propagation the polarization state of the propagating wave does not Faraday rotate due to the phase difference accumulation between the modes. Instead of Faraday rotation the phase difference between the modes leads to a polarization ellipse which oscillates between circular and linear states. This was not detected by the dipole antenna on ISIS II, but it is expected that the ePOP RRI will be able to observe this polarization change.

### 4.2.3 Quantifying Periodic Fading and Differential Mode Delay

Over the years the ISIS II spacecraft was operational it generated a great deal of data. Only a very small fraction of the data has been analyzed in this thesis. There were several requirements that needed to be met in order to study a particular pass in detail. The first requirement was that accurate orbital data of the spacecraft

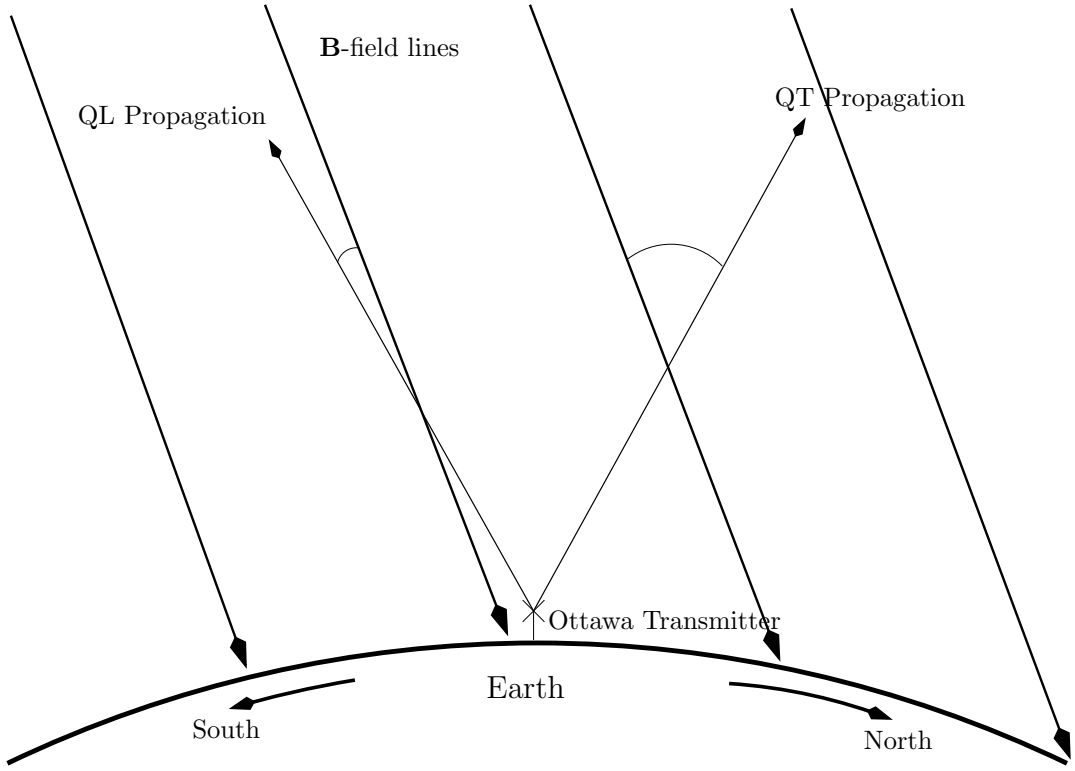


Figure 4.8: For a wave propagating to the south of the transmitter it was propagating in the QL regime. This causes Faraday rotation of the wave and resulted in periodic fading and mode delay to be observed in this region. When the satellite was to the north of the transmitter, the wave propagated in the QT regime and neither periodic Faraday fading or mode delay was observed.

needed to be available for a pass. The second was that the received signal for the pass needed to have been digitized. Finally, only passes that had signal received during a significant portion of the pass were studied. There were many passes that meet the first two criteria, however many had little or no signal recorded. The most prominent reason for this was likely that the overall electron density of the ionosphere was too high for propagation of a 9.3 MHz wave into the upper ionosphere where the satellite orbited. Most waves were reflected back towards Earth at lower altitudes. After eliminating passes using these criteria, the result was a detailed examination of eighteen passes from the summer months of 1978.

In analyzing the film data, the first step was to determine instances of measurable mode delay. Plots of signal amplitude, as in Figure 4.6, were examined at

several points along a single pass and instances where mode delay was observed were recorded. The magnitude of the mode delay was determined directly from the amplitude plot and the location of the satellite was recorded. There was measurable mode delay in fifteen of the eighteen passes. For the most part this delay was observed to the south of the transmitter and it ranged in magnitude from 0.1 ms to 0.8 ms. The general pattern was that the delay increased with increasing distance from the ground transmitter, which is expected because the O- and the X-modes will take longer paths to the satellite and aquire more time delay between each other.

The periodic Faraday fading was slightly more difficult to calculate than mode delay. Fourier analysis was performed on sections of the signal where Faraday fading was observed in order to determine the dominant frequencies. Of the eighteen studied passes, eight contained measurable Faraday fading. The magnitude of the fading was observed to vary from $\sim$0.5 Hz to $\sim$13 Hz. As with the mode delay, in general, the magnitude of the Faraday fading frequency increased with increasing distance from the transmitter. The increase of fade rate to the south is also reported by *James et al.*, [2005b]. It should be noted that the Fourier analysis method also measured the slower fading that was due to the satellite rotation to the north of the transmitter. It was observed that this frequency was indeed at $\sim$0.1 Hz in all cases, further supporting the conclusion that it was the satellite rotation that causes this periodic fading.

## 4.3 Ray Tracing for ISIS II

All of the suitable ISIS II passes over the Ottawa transmitter have been analyzed for periodic fading due to Faraday rotation and for differential mode delay. The magnitudes of these two quantities have been calculated throughout each pass. The next step was to test the ray tracing software to examine whether it could reproduce the results observed during the actual ISIS II mission. Fortunately, the ISIS II spacecraft performed several topside soundings every orbit along with the transionospheric observations, so an estimation of the electron density in the ionosphere at

the time can be obtained. The topside soundings occurred roughly once every 2.5° in latitude. Using the convergence method discussed in Chapter 3, ray paths were calculated for several points along the orbit of the satellite at the latitudes where signal was recorded. Next, the simulated periodic fade rates and mode delays were calculated by integrating over the various ray paths to the satellite. Finally, the fade rates and mode delay times calculated from the ray tracing model were compared to the actual data.

### 4.3.1 Developing $N_e$ profiles from Topside Soundings

It was found that the most important factor in determining the behaviour of a radio wave in the ionosphere was having a realistic electron density profile. The electron density peak in the F-region of the ionosphere can vary by more than one order of magnitude at different times and locations. Vastly different propagation characteristics will result from such different $N_e$ profiles. As a result, the characteristics of the signal received by a satellite from a wave which propagates through the ionosphere is dependent mostly on the $N_e$ profile. When performing ray trace calculations to model the expected signal, it was found that an accurate representation of at least the $f$oF2 peak density was needed. In the case of the ISIS II observations, the simulations of the received signal were greatly assisted by using $N_e$ information from the topside sounding mode which was interlaced with the transionospheric mode.

An example of an ISIS II ionogram is presented in Figure 4.9. Using the complicated inversion technique, the electron density in the ionosphere from the location of the F-peak to the satellite altitude can be calculated for that specific time and location (i.e., the topside ionosphere $N_e$ profile can be calculated). The calculation of the entire topside profile from a topside ionogram is rather involved and, of course, does not give any information on the bottomside profile. It was discovered that the most important aspect of an $N_e$ profile, with regard to the simulations, was a realistic F-region peak density ($f$oF2), only the $f$oF2 peak value was calculated from the topside measurements. This peak density was used to scale IRI modelled profiles. IRI model profiles are useful because they can be generated for any ionospheric

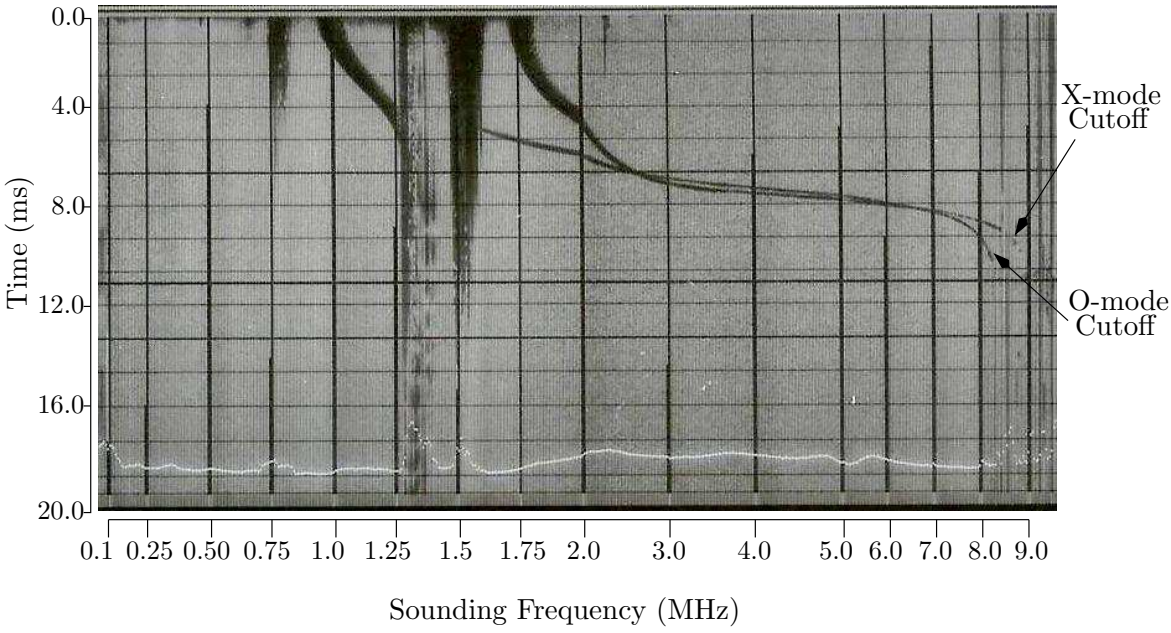


Figure 4.9: An example of a topside ionogram. The $f$oF2 density is determined from the O-mode cut-off frequency. A more detailed analysis can reveal the entire topside electron density profile. The ionogram was recorded during the pass on June 28, 1978 at 14:37 UT.

situation. Since the ionosphere was quiet and well behaved for the passes under consideration (see Section 4.4 and Table 4.1), it was expected that using a general IRI profile scaled to specific F-peak densities was sufficient. This turned out to be the case. Another reason to use IRI profiles is that, for ePOP ray path modelling, the only available $N_e$ profiles at this time are models such as IRI.

The calculation of the density at the F-peak is fairly straightforward. When a radio wave is propagating in a medium with increasing electron density the index of refraction decreases as was demonstrated in Figure 2.3. The result is that the wave will slow down as it propagates. When the plasma frequency, given by Equation 2.16, becomes larger than the wave frequency, the index of refraction for the O-mode becomes purely imaginary. At this point the O-mode is reflected and propagates back towards the transmitter. In a sounder, when the frequency becomes high enough, the O-mode will penetrate through the F-peak and no return signal will be obtained. If one takes the last frequency that was reflected, one can calculate the electron

density of the $f$oF2 peak. By setting the plasma frequency (Equation 2.16) equal to the radar frequency and solving for $N_e$, the equation to determine the peak electron density in the ionosphere is,

$$N_e = \frac{4\pi^2 m_e \epsilon_o f^2}{e^2}. \tag{4.1}$$

Substituting the values for the constants this reduces to,

$$N_e = 0.0124 f^2. \tag{4.2}$$

This equation will give the value for $N_e$ at the F-peak given the maximum reflected frequency $f$. In the example given in Figure 4.9, the O-mode cutoff frequency is ∼8.2 MHz. Using Equation 4.2, the F-peak electron density is therefore ∼8.3x10$^{11}$ m$^{-3}$.

Once the F-peak density was determined only one piece of information about the $N_e$ profile was known. The next step was to use IRI modelling to estimate $N_e$ for all other altitudes. In order to obtain the full electron density for a given latitudinal location the IRI model was used with an F-peak scale density given by the topside sounder. The IRI profile that was chosen to be scaled was for an average day (quiet) in July, 1978, at the location of Ottawa and for the approximate local time of the satellite pass. The result was a profile that lists $N_e$ as a function of altitude starting at 60 km up to 1460 km with the electron density value every 1 km. This process was done for each topside sounding that was available on each pass. These profiles were then combined for each pass to give a 2-D $N_e$ profile in latitudinal range from the transmitter and altitude.

### 4.3.2 ISIS II Ray Tracing Methodology

The previous ray tracing discussions have all dealt with the calculating of ray paths to a single point in space. The next step required was to perform ray trace calculations to several points along a satellite track and to calculate the polarization state of the wave at each point. For the studied passes of the ISIS II satellite the position in latitude, longitude, and altitude of the spacecraft was listed once every second. Using this knowledge, a representative satellite pass was entered into the ray tracing

program. Since the satellite was in a nearly perfectly polar and circular orbit, the only variable that changes throughout a pass was latitude. A series of ray paths were calculated along a pass of the satellite every 0.1° in latitude.

Using the method described in Chapter 3, the polarization state was calculated at every point along the pass. The change of phase difference between the modes at two subsequent points along the satellite path was calculated and a value for the change in orientation angle from one point to the next was obtained. This change in orientation angle was divided by the time it takes the satellite to travel the distance between the two points and the result was the fade rate per second in radians. This value was then divided by $2\pi$ to obtain the fade rate in Hz. Therefore, the formula for calculating fade rate ($F_R$) from the two calculated phase differences ($\phi_{ox1}$, $\phi_{ox2}$) is given as,

$$F_R = |\frac{v_s(\phi_{ox1} - \phi_{ox2})}{2\pi d}| \tag{4.3}$$

where, $d$ is the distance the satellite travelled from point 1 to 2, and $v_s$ is the velocity of the satellite calculated by,

$$v_s = \sqrt{\frac{GM_e}{(h_s + R_e)}}. \tag{4.4}$$

$G$ is the gravitational constant, $M_E$ is the mass of the Earth, $h_s$ is the altitude of the satellite, and $R_E$ is the radius of the Earth. This fade rate was calculated for every point along the path. Also calculated using Equation 3.14 was the differential mode delay at each point.

## 4.4 Comparison of Ray Traces to Actual Data

All the passes that have been simulated using the ray tracing program were compared to the observed data. The passes that were studied took place on days with relatively low solar activity. Table 4.1 lists the passes and the corresponding Kp index at the time of the pass. Kp is a measure of the geomagnetic disturbance due to solar activity on a scale of zero to nine. On the Kp scale, zero represents very quiet conditions and nine represents very disturbed conditions. It was noted that all the studied passes

| Date of Pass | Time (UT) | Kp index |
|---|---|---|
| 178 (June 27) | 13:50 | 3.0 |
| 182 (July 1) | 14:25 | 2.3 |
| 184 (July 3) | 02:00 | 1.0 |
| 184 (July 3) | 13:50 | 1.7 |
| 185 (July 4) | 02:40 | 3.7 |
| 189 (July 8) | 01:25 | 2.7 |
| 189 (July 8) | 13:15 | 3.3 |
| 190 (July 9) | 02:00 | 3.0 |
| 190 (July 9) | 13:50 | 2.0 |
| 192 (July 11) | 01:25 | 2.0 |
| 193 (July 12) | 02:00 | 0.3 |

Table 4.1: Solar Activity during each ISIS II pass.

occurred for times when Kp was less than four.

For all passes of the satellite over the Ottawa transmitter the observed fade rate and mode delay show the same trends with the values from the simulations. For example, Figures 4.10 and 4.11 are typical results comparing observed to simulated fade rates and Figures 4.12 and 4.13 are comparisons of observed to simulated mode delay, all as a function of latitude. These examples show rather similar trends between the ray path simulations and the actual observed satellite data.

It should be noted that the results that were obtained from the ray path simulations were surprisingly good, especially when one considers possibilities for errors to occur. The intermittent topside sounder only produced one $N_e$ profile every 350 km. The ionosphere can vary by a fairly substantial amount over this distance, so it was fortunate that the $N_e$ profiles were realistic enough to allow the ray path simulations to reproduce the experiment results as accurately as they did. As well, the film that the topside soundings were recorded on was not always clear. There were several ionogram scans in which the O-mode cut off frequency was either too weak

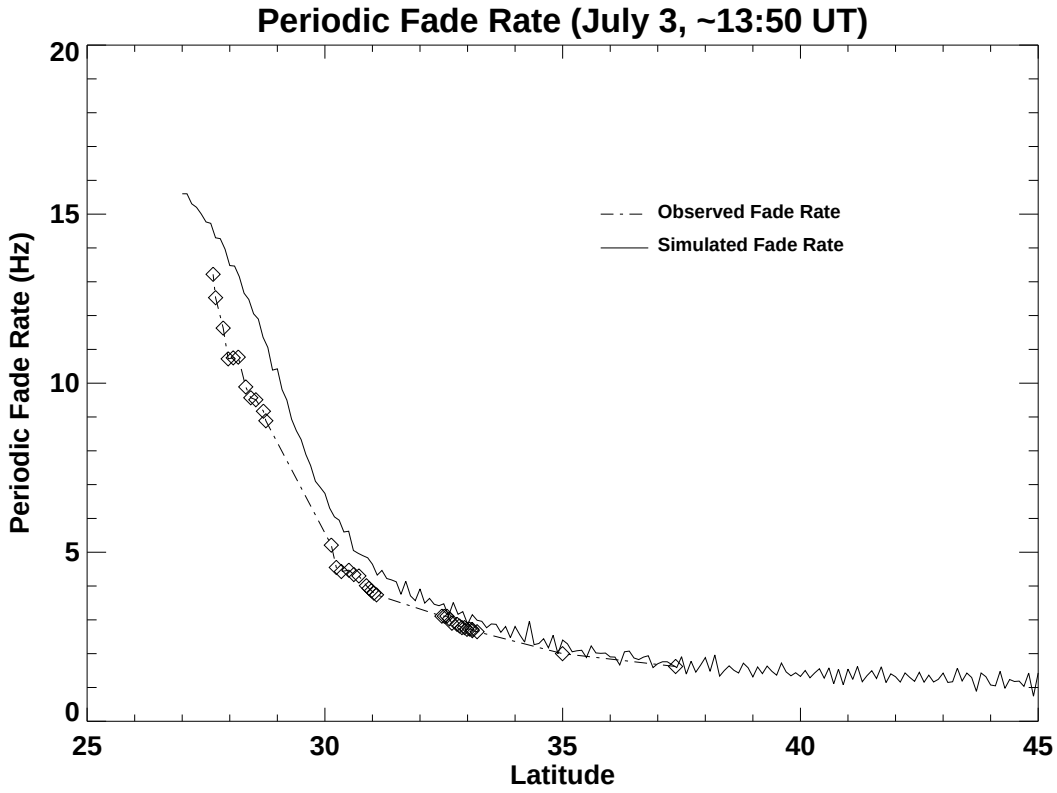


Figure 4.10: Example comparison of simulated and observed periodic fade rates for a single ISIS II pass over Ottawa.

or there was too much noise recorded on the film to determine the O-mode cut off to a suitable accuracy. Finally, the use of only the $f$oF2 peak and not the entire topside profile in the simulations was believed to create a substantial possibility of error. The fact that the simulations followed the observed data quite closely despite the uncertainties mentioned indicates a few important points. The passes all took place on relatively quiet days, and this was perhaps a reason that the intermittency of the ionograms did not cause more error. This also indicates that on quiet days the IRI modeller is sufficient to develop accurate enough profiles given just the $f$oF2 peak as a scaling value.

The examples of Faraday fading comparisons have many more data points than the mode delay examples. This is because the data point locations for mode delay were picked quite subjectively by choosing instances where there was clear and de-

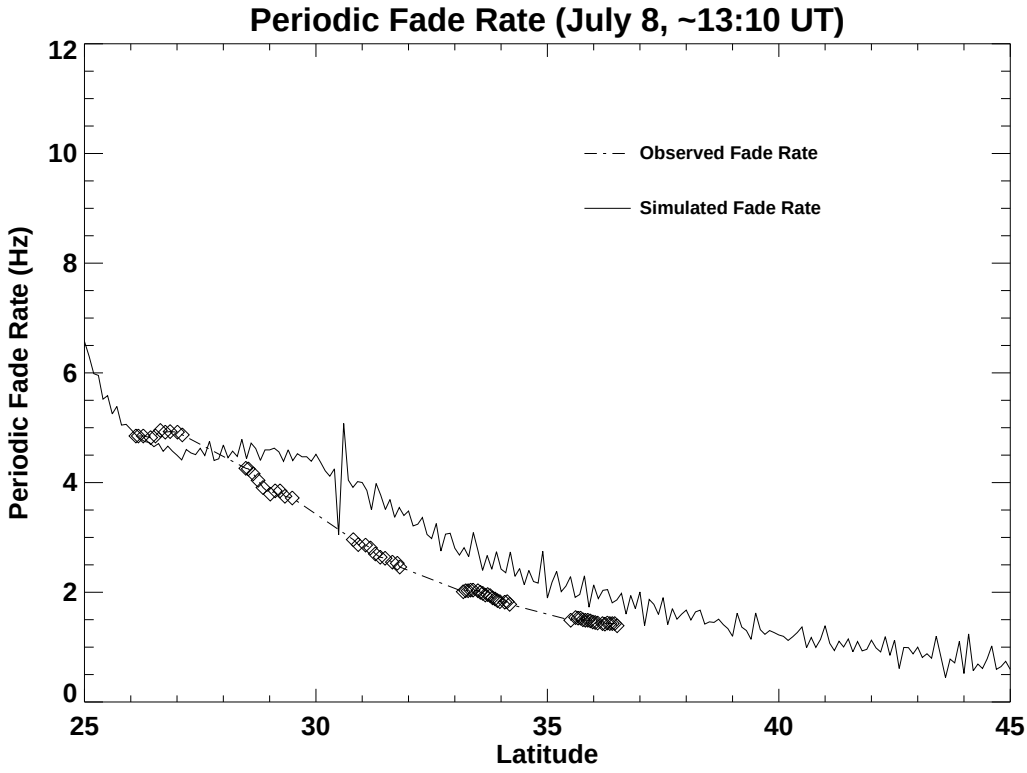


Figure 4.11: Example comparison of simulated and observed periodic fade rates for a single ISIS II pass over Ottawa.

fined mode delay that could be measured. The data points for periodic fading were found by performing a Fourier analysis on the transionospheric sections of the data in a methodological manner so that more data points were revealed. The signal that will be analyzed from the ePOP mission will have full polarization information, no interruptions for topside scanning, and will be much clearer and stronger. As such, it is expected that both fading and mode delay values will be available almost continuously throughout a pass. Nonetheless, the intermittent data points are sufficient for comparing ray path simulations to actual observed data.

The simulated data are strongly indicative of characteristic trends observable in the data sets. It is remarkable how well the two data sets show the same trends. Some general limitations between the agreement of the trends were discussed above. Now some specific limitations of this analysis will be discussed. One limitation of

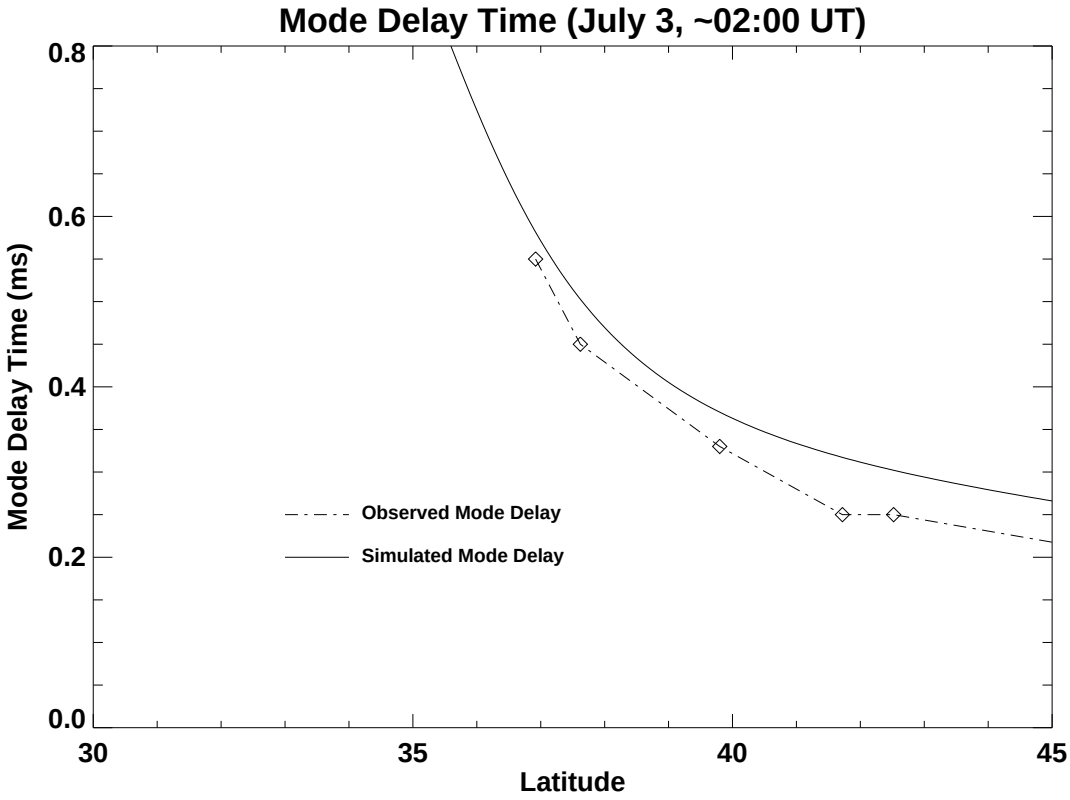


Figure 4.12: Example comparison of simulated and observed mode delay times for a single ISIS II pass over Ottawa.

the accuracy of the simulation was the determination of realistic $N_e$ profiles from the intermittent topside soundings on ISIS II ($f$oF2) and the model IRI profiles. The sounder only recorded a topside profile about once every 50 s and this amounts to approximately one profile every 2.5° in latitude. This spacing results in the possibility of small scale structures existing in the ionosphere at the time of the pass but not being properly simulated. An example of this can be observed in the pass that occurs during the afternoon of July 9. A portion of the received signal is shown in Figure 4.14. The fade rate observed at 35.6° latitude was 4.5 Hz while the fade rate observed at 35.2° was 6.6 Hz. A difference in fade rates of 2.1 Hz was observed over a latitudinal range of only 0.4°, while an electron density profile was only generated every 2.5° in latitude. This is very likely one reason for the discrepancy between the observed and simulated fade rates at this location as illustrated in Figure 4.15.

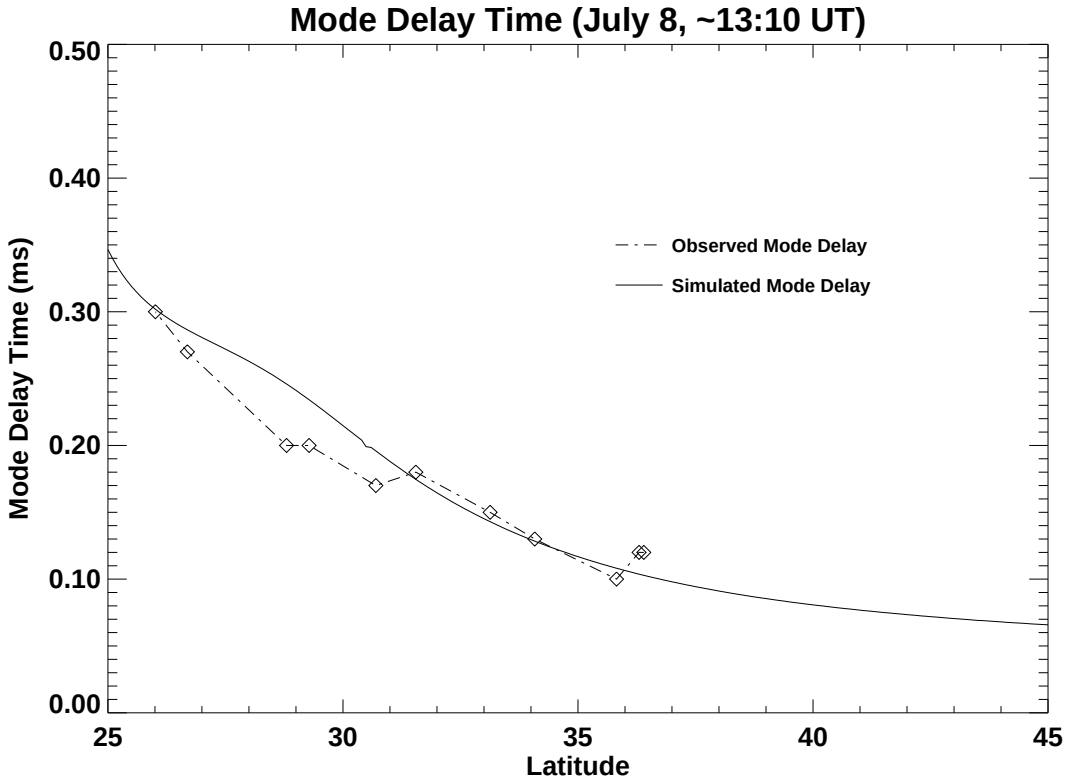


Figure 4.13: Example comparison of simulated and observed mode delay times for a single ISIS II pass over Ottawa.

Another problem in obtaining realistic $N_e$ profiles is due to data quality in some of the topside ionograms themselves. In some cases the signal received from the O-mode near the cutoff frequency was very weak making it difficult to determine. As an example, consider Figure 4.16 which shows an ionogram from the pass on July 8. The difficulty in determining the O-mode cut off in Figure 4.16 can be demonstrated by comparing this ionogram to the relatively clear O-mode cut off observable in the ionogram in Figure 4.9. The ionogram in Figure 4.16 can be interpreted such that the plasma frequency in the F-region may be anywhere from 5.2 MHz to 5.8 MHz. This leads to a range of $N_e$ peaks from 3.4x$10^{11}$ m$^{-3}$ to 4.2x$10^{11}$ m$^{-3}$. This ambiguity in the $N_e$ peak value may account for the small discrepancies observed in the comparisons of fade rate and mode delay in Figures 4.11 and 4.13. Clearly, available and accurate $f$oF2 values are critical in producing accurate ray tracing simulations.

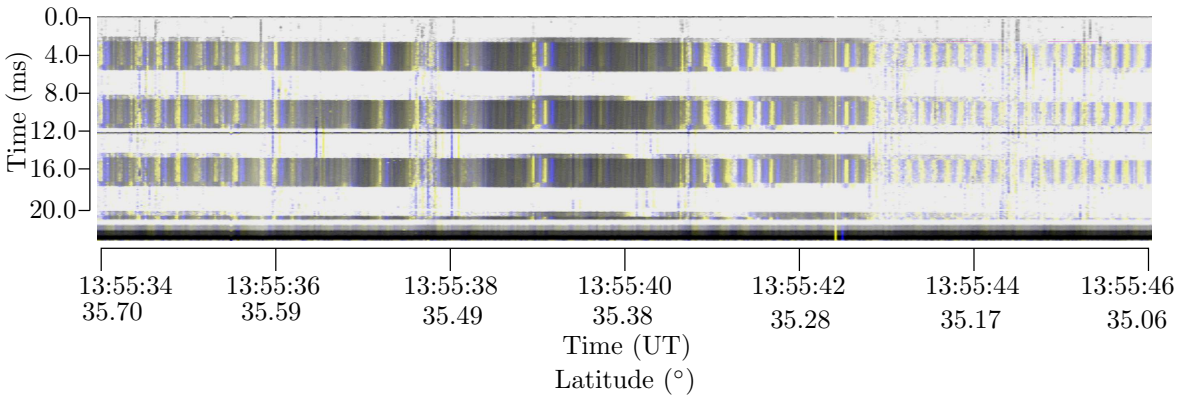


Figure 4.14: Example of rapidly changing fade rates observed in the signal on July 9. The fade rate at 35.6° is 4.5 Hz while the fade rate at 35.2° is 6.6 Hz.

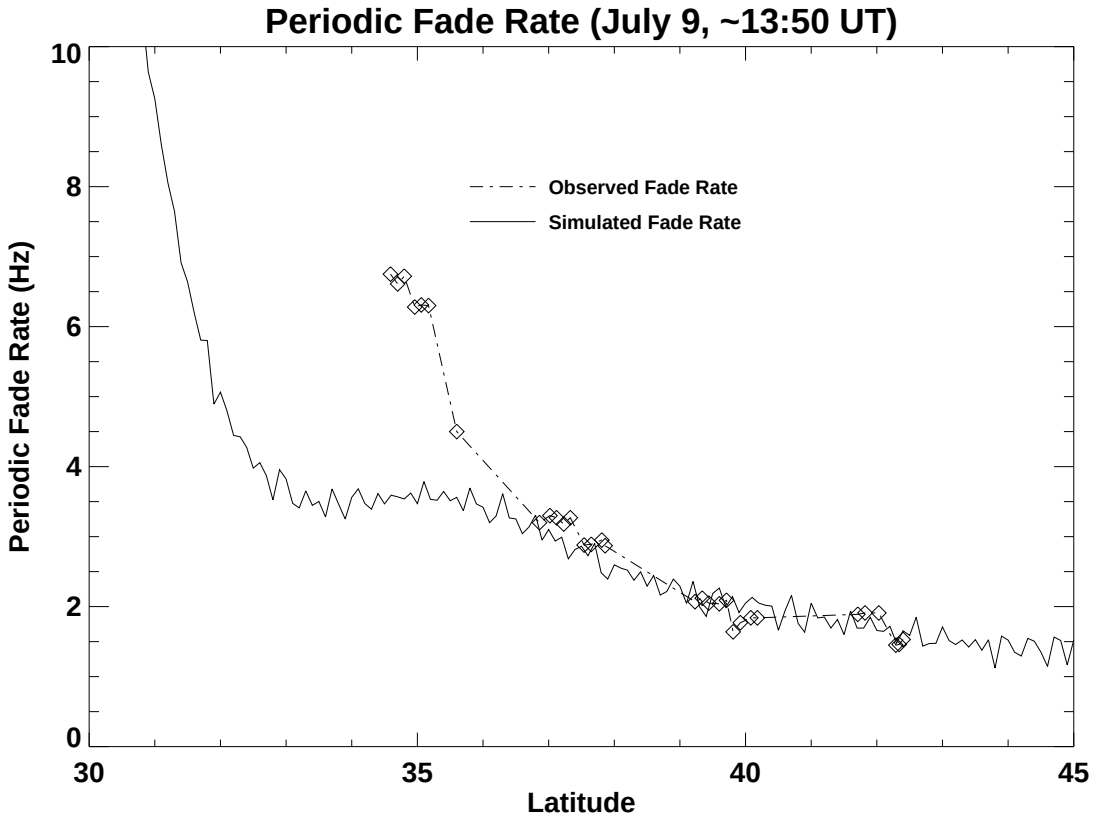


Figure 4.15: Observed and simulated fade rates for the July 9 pass. Rapid change in fade rates around 35° latitude were observed which the ray trace failed to simulate.

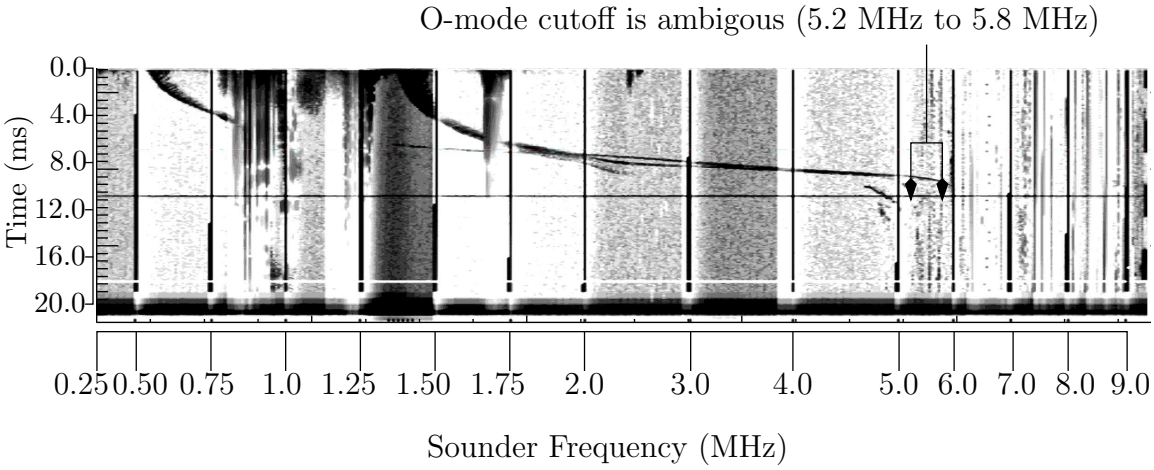


Figure 4.16: Topside ionogram example from the July 8 pass. The plasma frequency in the F-peak is not clearly defined and can be estimated to range from 5.2 MHz to 5.8 MHz. The ionogram was recorded at 42° latitude.

### 4.4.1 Linear Regression Analysis

Despite some difficulties in obtaining completely realistic $N_e$ profiles for some of the passes, the comparisons of observed data to simulated values indicate remarkably similar trends. A linear regression analysis of observed data to simulated data demonstrates this. Since each pass only has a few data points, values for all the passes were compared together to provide more meaningful statistics. Figure 4.17 shows the comparison of all data points for observed fade rates on each simulated pass plotted against the corresponding simulated fade rates at the same latitude. The linear regression analysis indicates that the points lie along a line with a slope of 1.07 and a regression value of 0.934. The number of points compared in this analysis was 213. Likewise, all the observed and simulated data points for mode delay were compared. The mode delay comparison is presented in Figure 4.18. Here the statistics consists of 63 points and regression analysis gives a slope of 1.14 and a regression value of 0.930. The ideal slope and regression values for this analysis are 1.0 so the simulated and observed values for both periodic fade rate and differential mode delay agree.

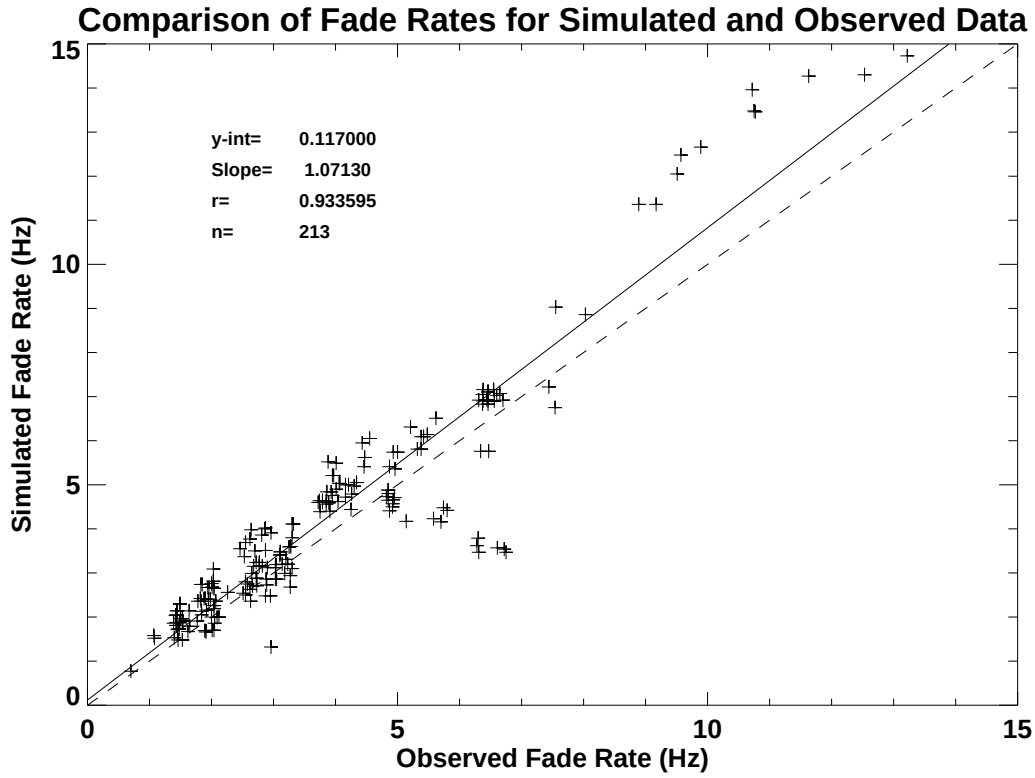


Figure 4.17: Linear regression comparison of all fade rate values. The solid line is the best fit line and the dashed line is the ideal fit line.

## 4.5 ISIS II Analysis Summary

The satellite ISIS II provided a good set of data to study in preparation for the transionospheric propagation experiment with ePOP. Several passes of the satellite over Ottawa, Canada resulted in HF signal that propagated from a ground transmitter through the ionosphere to be recorded by the dipole antenna on the spacecraft. The signal observed in these passes has been analyzed and several signal features were apparent. A time delay between the arrival of the O-mode and X-mode at the satellite exists due to separation of the two modes when they propagate through the ionosphere. Periodic fading of the signal was observed for significant portions of many of the passes. This fading was caused both by the satellite stability rotation, which caused the receiving dipole to significantly change its orientation with respect

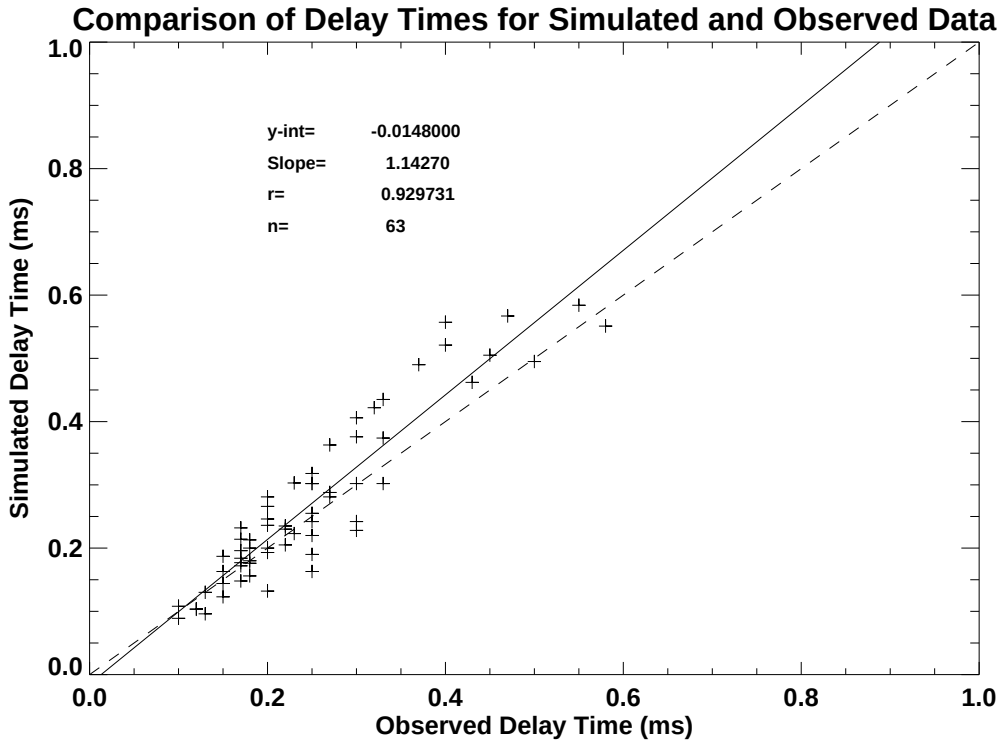


Figure 4.18: Linear regression comparison of all mode delay values. The solid line is the best fit line and the dashed line is the ideal fit line.

to the direction of wave propagation, and by Faraday rotation of the wave. The magnitudes of mode delay and Faraday periodic fading at various latitudes has been tabulated. Ray path simulations were performed to simulate Faraday fade rates and mode delay times of the actual ISIS II observations. A comparison of these simulated values with those determined from the actual ISIS II observations revealed very similar trends. There was good correlation between the simulated and observed data sets as linear regression analysis indicated slopes close to the ideal value of unity and high regression values (periodic fade rate: slope=1.07, regression coefficient=0.934; mode delay: slope=1.14, regression coefficient=0.930).

This ISIS II analysis has accomplished two important objectives. It has shown that the ray trace program can accurately simulate the signal that will be received by a spacecraft, and it has given insight into the signal structure that is to be expected from other transionospheric experiments such as the RRI on ePOP.

# Chapter 5

# RRI Signal Modelling

## 5.1 The CASSIOPE Satellite

CASSIOPE stands for CAScade, Smallsat, and IOnospheric Polar Explorer. This is a Canadian led small satellite mission with two distinct payloads. The scientific payload is the group of instruments which make-up the enhanced Polar Outflow Probe (ePOP) and the commercial payload, called Cascade, is a proof-of-concept data storage-and-forward system. Despite the satellite actually being called Cassiope, it is also commonly referred to as ePOP and throughout this chapter the two names will be used interchangeably to describe the satellite. The goals of the ePOP mission are: to study outflows of both plasma and neutral particles from the polar region; to study the generation of waves and interactions of particles associated with the outflow; and to examine the effects of the outflow on radio wave propagation. This thesis is concerned with developing a physically based model to assist in better understanding the third objective. The Cassiope satellite is to be launched in late 2007 and operate for at least four years. It will be placed in an elliptical orbit with an apogee of 1500 km and a perigee of 350 km. The inclination of the orbit will be 80° and so, in this respect, the orbit will be quite similar to the ISIS II satellite. General information on the CASSIOPE satellite is found at `http://mertensiana.phys.ucalgary.ca/cassiope.htm`.

Cascade is a proof-of-concept data transferring service. The payload has a large data storage system and a very high rate of data upload and download. The idea is to have the satellite fly over remote stations, such as oil and gas mines, and upload gigabytes of data in the few minutes when the satellite is overhead. The

data is stored until the satellite passes over the receiving station, when it is then downloaded. Basically, this is a test of a new system for transferring large amounts of data quickly across the globe when land line access is not available. The benefit of the Cascade system for ePOP is that the data storage and high data transfer rate abilities will be available for the scientific data that is collected by the many instruments on ePOP.

There are eight scientific instruments on the ePOP payload [*Yau et al.*, 2002]:

- The Imaging Rapid-scanning Mass spectrometer (IRM) measures the composition and velocities of ions in the region of the spacecraft.
- The Suprathermal Electron Imager (SEI) will measure electron energy distributions.
- The Neutral Mass and velocity Spectrometer (NMS) will measure the mass and velocities of neutral atmospheric constituents.
- The Fast Auroral Imager (FAI) will study emissions in the optical range.
- The Radio Receiver Instrument (RRI) is the focus of this thesis and will measure wave electric fields in the range of 0-18 MHz.
- The MaGnetic Field instrument (MGF) will measure the magnetic field strength and direction at the satellite.
- A GPS Attitude, Position, and occultation experiment (GAP) will be used for determining the exact location and orientation of the satellite and for ionospheric profile measurements.
- The Coherent Electromagnetic Radiation tomography experiment (CER) will transmit radio waves from the satellite to ground receiving stations to study radio wave propagation. This is opposite to the RRI experiment where the ground stations are the transmitters and the satellite instrument is the radio receiver. In the case of the CER, however, the frequencies will be in the VHF and UHF ranges instead of the HF range as with the RRI.

The RRI on ePOP will consist of four 3 m monopole antennas. They will be oriented to effectively make two perpendicular 6 m dipole antennas, however each side of one dipole will have a separate receiving channel. In this way there are a number of operating modes that can be used. If all the monopoles are receiving at one frequency, the full polarization of a wave from the ground can be determined. Among other things, this could be used to detect $N_e$ enhancements or depletions in the ionosphere through changes in the polarization state of the received wave. Another mode that could be used is to have two monopoles receive on one frequency and the other two receive on a different frequency. The polarization state will be ambiguous; but an estimate of total electron content along the propagation path can be made by examining the Faraday fade frequencies similar to the analysis presented in Chapter 4. In this case though there will be two different fade frequencies and the difference between them can be used to estimate electron density.

## 5.2 Ray Trace Modelling of RRI Signal

### 5.2.1 Simulated ePOP Passes

Unlike the satellite path for ISIS II, which was essentially north-south oriented and therefore varied essentially in latitude only during a pass, the satellite path for ePOP will also vary significantly in longitude during a pass. Instead of a straight north-south path over the transmitter, the ePOP orbits will resemble the passes shown in Figure 5.1. The satellite will travel over the transmitter in one direction and when the Earth has rotated 180° underneath the satellite track, the satellite will pass over the transmitter travelling the opposite direction. This is indicated by the labeled northeast and southeast passes in the diagram. Of course, the satellite will not always pass directly over the ground transmitter. Three passes, separated by 15° in longitude, are plotted for each direction. Also shown in Figure 5.1 is the SuperDARN field of view (FOV). This illustrates that passes travelling northeast over the transmitter will be the most useful because they will spend a greater time

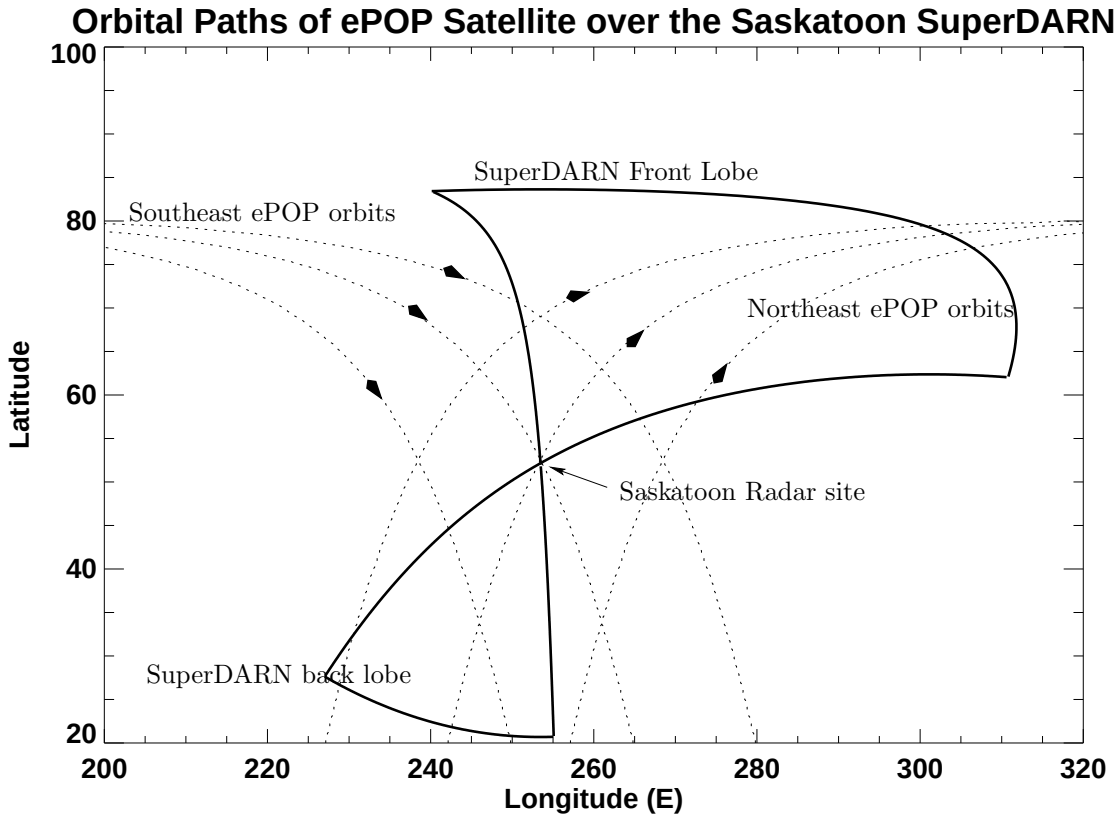


Figure 5.1: Various ePOP orbital paths over the Saskatoon SuperDARN array and the SuperDARN field of view.

in the FOV of the radar.

Several passes were simulated for the ray path modelling analysis presented below. In these simulations, a well behaved and quiet ionosphere, as with ISIS II simulations, was assumed. The three passes plotted in Figure 5.1 were simulated for the satellite travelling both northeast and southeast over the transmitter. These passes were also simulated at three different altitudes for the satellite; 1500 km, 900 km, and 350 km. Finally, all these combinations of passes were simulated using three different 2-D $N_e$ profiles. In total this amounted to 54 simulated passes over the transmitter. Only a few representative ones will be presented in detail. These passes were all simulated using a radar frequency of 15 MHz. Some additional simulation passes at 9.303 MHz (the ISIS II experiment frequency) were used as a comparison with

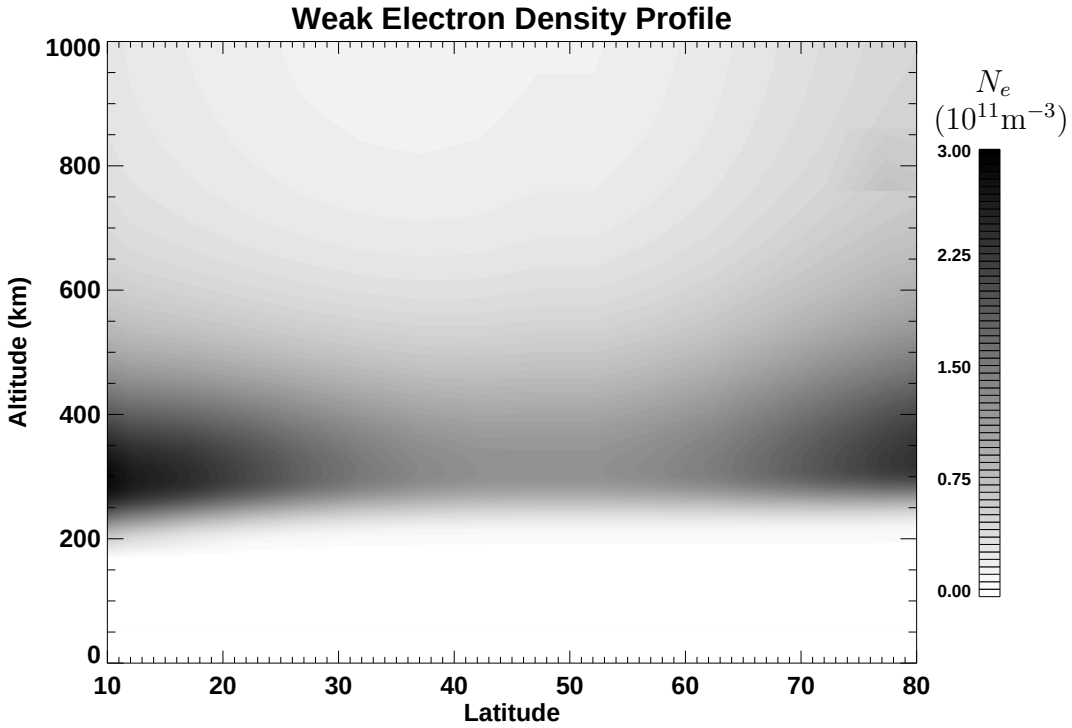


Figure 5.2: The lowest of the three 2-D $N_e$ profiles used for ePOP simulations.

the 15 MHz simulations. As the SuperDARN radar has the ability to transmit from 8 MHz to 20 MHz, it was of interest to examine the different propagation and signal characteristics at different frequencies.

Three 2-D $N_e$ profiles have been constructed for the ePOP simulations. Each 2-D profile was created using the IRI modeller by choosing a specific time and then determining the electron density at various latitudes along the Saskatoon longitude. The objective was to make the 2-D profiles as different from one another as possible. Therefore the low electron density 2-D profile or weak 2-D profile was modelled from IRI profiles on December 21, 2002, at 00h00 LT (winter solstice, midnight) and is presented in Figure 5.2. It is evident that the electron density actually increases both to the north and south of Saskatoon. The reason for this is that the sun is shining in the upper atmosphere even at night at high latitudes, thus causing an increase in $N_e$ to the north of Saskatoon. To the south of Saskatoon, a higher $N_e$ is expected even at night, as there is more photo-ionization of the upper atmosphere

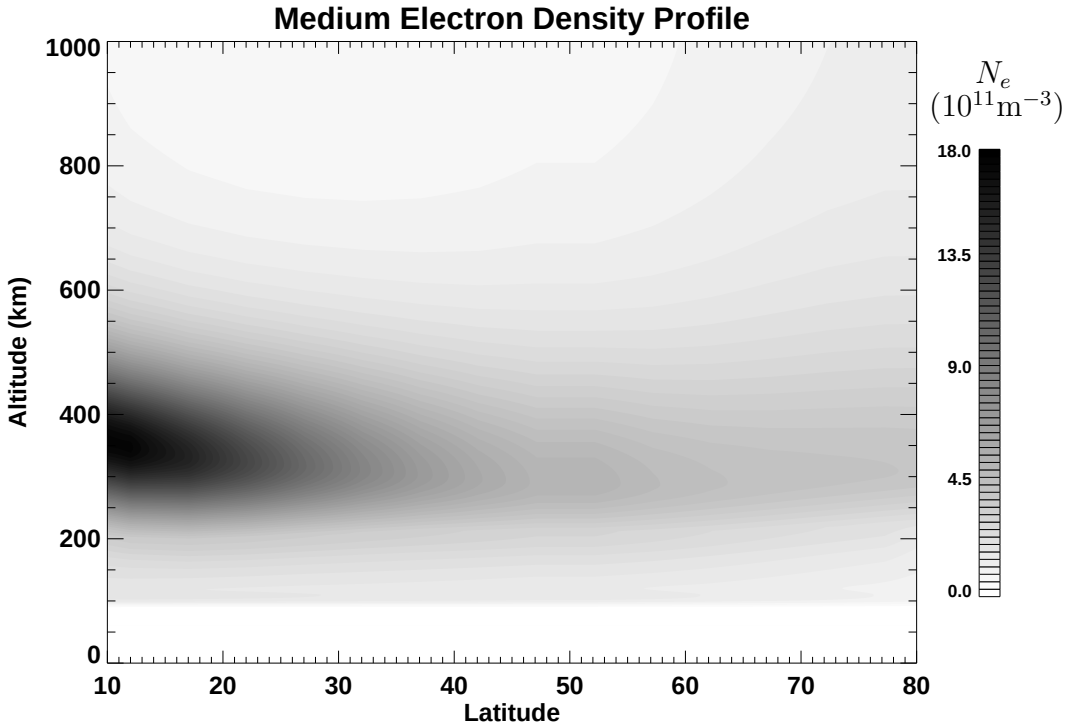


Figure 5.3: The medium of the three 2-D $N_e$ profiles used for ePOP simulations.

closer to the equator during the day and the recombination rate at night is not high enough to lower $N_e$ values at high altitudes. A medium 2-D profile was modelled for the date July 11, 2002, at 12h00 LT and appears in Figure 5.3.

Finally, the strong 2-D profile was modelled for the date December 21, 2002, at 12h00 LT and is shown in Figure 5.4. The strong and medium 2-D profiles have roughly the same $N_e$ to the south of Saskatoon which is to be expected as there are less seasonal differences in a sunlit ionosphere the closer one gets to the equator. Nevertheless, the strong 2-D profile is much higher in density overall directly above Saskatoon and this will differentiate it from the medium 2-D profile results.

Ray path simulations have been carried out for all 54 passes described at a transmitting frequency of 15 MHz. Comparisons were made between the different 2-D profiles, altitudes, longitudes and pass directions. The simulated fade rate and mode delay were determined and plotted in each case. Since there are so many passes to choose from and comparing all of them to each other would be nearly impossible,

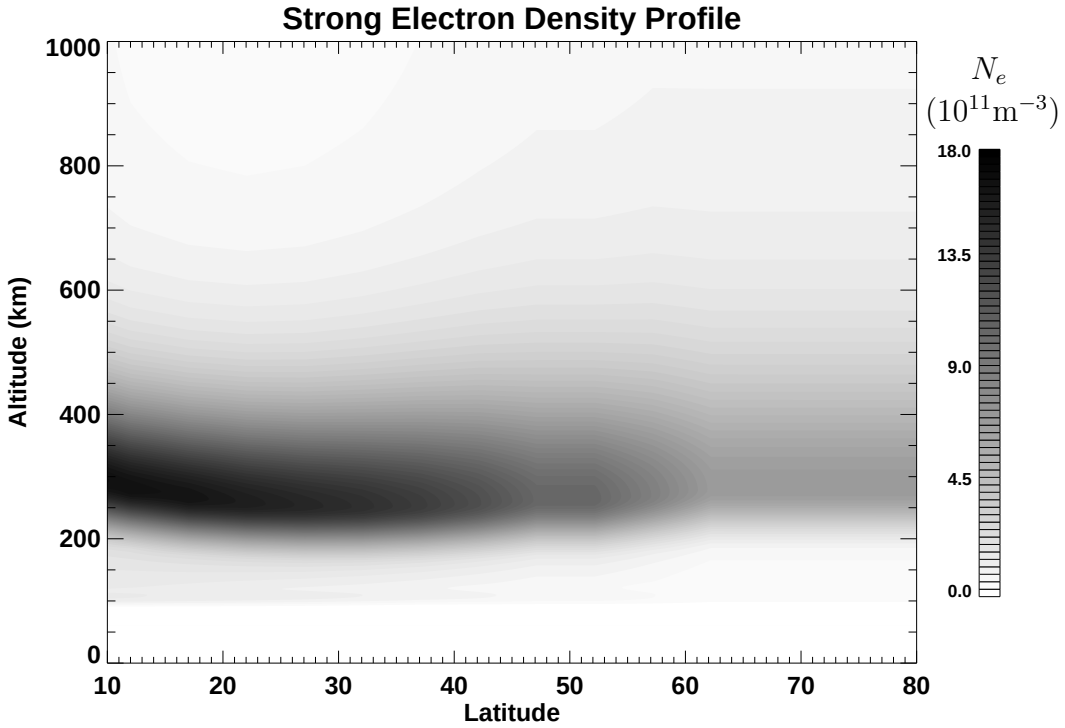


Figure 5.4: The highest of the three 2-D $N_e$ profiles used for ePOP simulations.

only one comparison was made for each variable. As well, a pass at 9.30 MHz using the medium profile has been simulated and presented.

### 5.2.2 Predicted Ray Trace Modelling Results

By examining the equations to calculate fade rate and differential mode delay, Equations 3.14 and 4.3, an initial estimate of the ray tracing results can be made. Two main variables will cause an increase in both fade rate and mode delay. The first is the difference between the indices of refraction for the O- and X-modes. If this quantity increases, both mode delay and fade rate will also increase because there will be more separation between the O- and X-modes. The two indices of refraction are plotted in Figure 2.3 as a function of the ratio of plasma frequency to radar frequency, $X$. The separation between the modes increases with an increase in $X$. If the radar frequency is set, an increase in plasma frequency, caused by a higher $N_e$,

will produce more separation between the two modes. As such, a higher $N_e$ should produce higher fade rate and mode delay values. If, on the other hand, the plasma frequency is set and the radar frequency is raised, $X$ will decrease and less mode delay and fade rate will be detected. The second variable to cause an increase in fade rate and mode delay is distance travelled by the wave. Since both values result from integrating along the path of the propagating wave, an increase to propagation distance will increase the frequency of fading and the magnitude of mode delay.

In Chapter 3 it was shown that the amount a wave path bends due to propagating in the ionosphere is proportional to the index of refraction (Equation 3.9). Therefore, the transmitted frequency and $N_e$ will also affect the amount of refraction that occurs when the wave propagates through the ionosphere. For lower transmitter frequencies and/or higher $N_e$ profiles, more bending of the wave is expected. As such, the wave will be totally refracted back to Earth at higher elevation angles and signal will be obtained over a much smaller latitudinal range with lower transmitter frequencies or higher $N_e$.

### 5.2.3 2-D $N_e$ Profile Comparison

For one comparison of the various 2-D $N_e$ profiles, satellite passes directly over the transmitter, travelling northeast and at 900 km altitude are compared for the three profiles. The comparison of fade rate appears in Figure 5.5 and the comparison of mode delay in Figure 5.6. One can immediately discover that both mode delay and fade rate are higher for the overall stronger 2-D $N_e$ profiles. The fade rate for the strong 2-D profile is $\sim$2.5 Hz and the mode delay is $\sim$0.05 ms overhead of the transmitter. The medium 2-D profile fade rate is only $\sim$1 Hz and the mode delay is $\sim$0.03 ms overhead. Finally, the weak 2-D profile has a fade rate that is only a fraction of a Hz throughout the pass and a mode delay that is always $<$0.02 ms. One can also observe the range of latitudes that connecting ray paths are determined for each 2-D profile. With the strong 2-D profile, paths were able to be simulated from about 37° to 73°. The range increases to 29° to 76° for the medium 2-D profile and 22° to 79° for the weak 2-D profile. It should be noted that the signal is expected

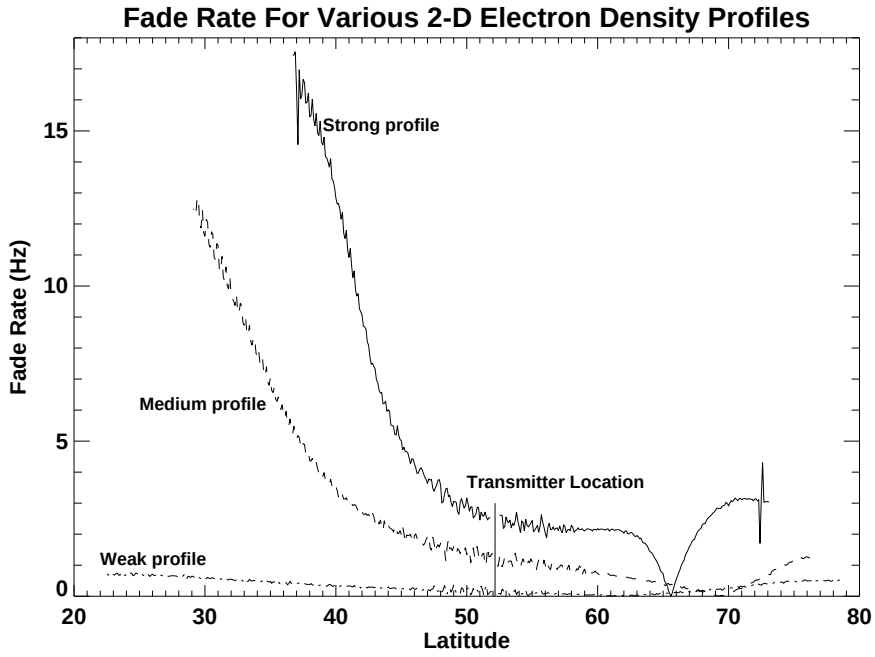


Figure 5.5: The simulated fade rates as a function of latitude for the three different 2-D profiles.

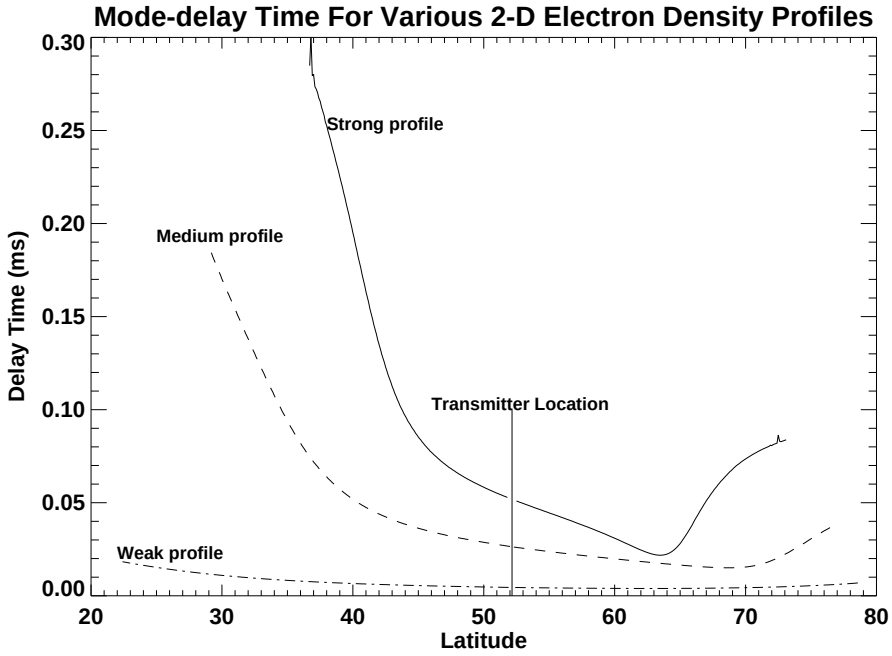


Figure 5.6: The simulated mode delays as a function of latitude for the three different 2-D profiles.

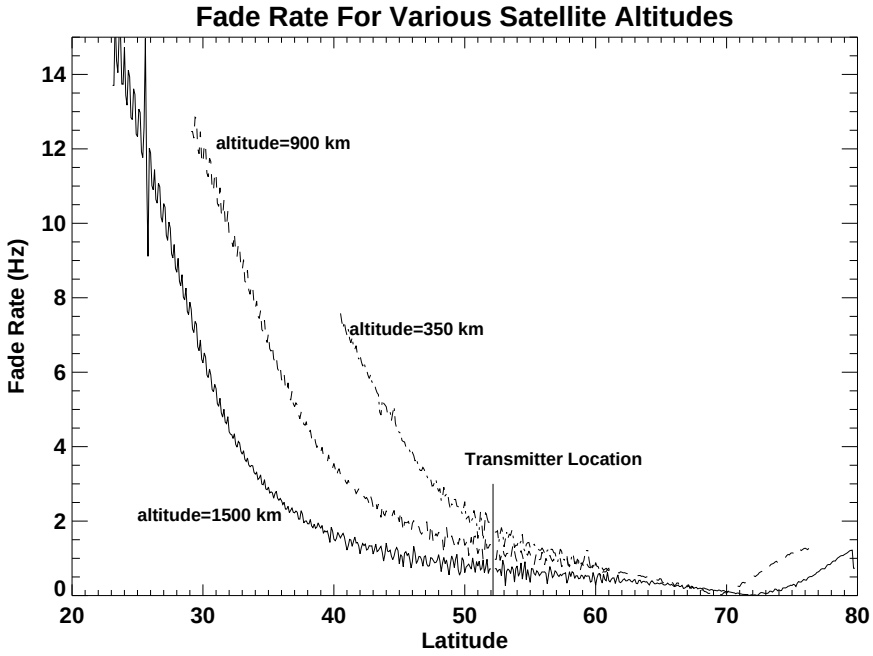


Figure 5.7: The simulated fade rates for various satellite altitudes using the medium 2-D profile.

to be very weak and noisy near the extremes of the passes. This was observed with the ISIS II results and will most likely be similar with ePOP, although ePOP will be much more sensitive. Therefore the high fade rates and mode delay simulated at the far southern ends of the passes likely will not be clearly observable during the ePOP mission.

### 5.2.4 Satellite Altitude Comparison

Three simulated altitudes were compared using the medium 2-D profile as a reference profile. The compared passes were again directly over the transmitter and in the northeast direction. The comparison between 350 km, 900 km, and 1500 km altitude for simulated fade rate and mode delay are displayed in Figures 5.7 and 5.8 respectively. The fade rate and mode delay simulated to the far north and south of the transmitter was actually less for higher satellite altitudes. This behaviour is not immediately predicted because one expects the separation between the modes to be

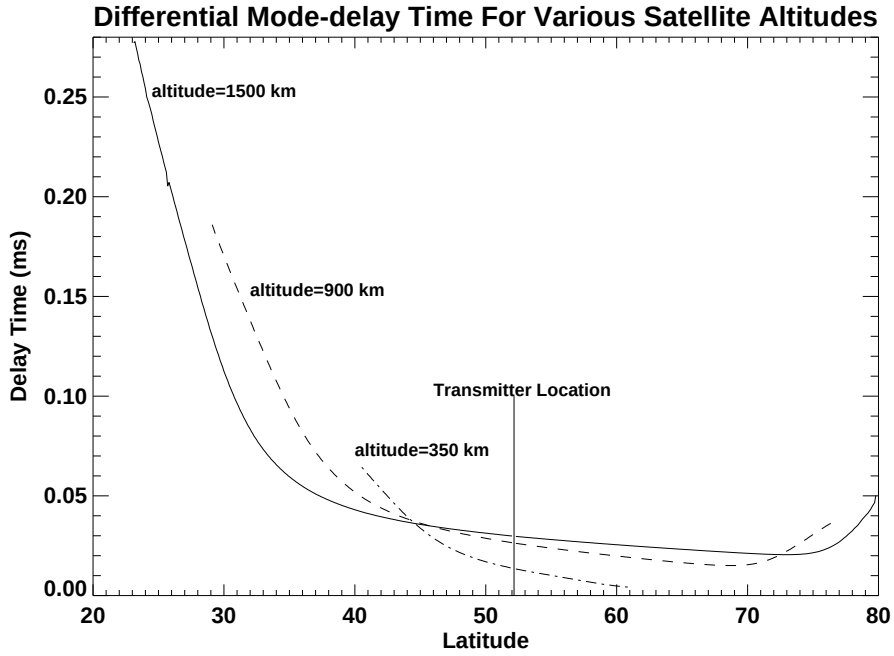


Figure 5.8: The simulated mode delays for various satellite altitudes using the medium 2-D profile.

less for lower altitudes because the path to the satellite is less. These results may be explained by a combination of factors. When the satellite is at a lower altitude near the horizon, the wave travels further in the highly dense F-region than it would for a higher altitude pass. Therefore, although the path length of the travelling wave is smaller, the difference between indices of refraction is larger and this outweighs the short path length. Above the transmitter, the fade rate is similar for all altitudes.

The mode delay is demonstrated to be higher for higher altitudes above the transmitter. This is expected, as there is less distance travelled by the wave over which the modes can separate during a low altitude pass. The latitudinal extent of simulated ray paths is greatest for the highest altitude. This is to be expected from simple geometry; a satellite at 1500 km will be visible at a greater range than a satellite at 350 km.

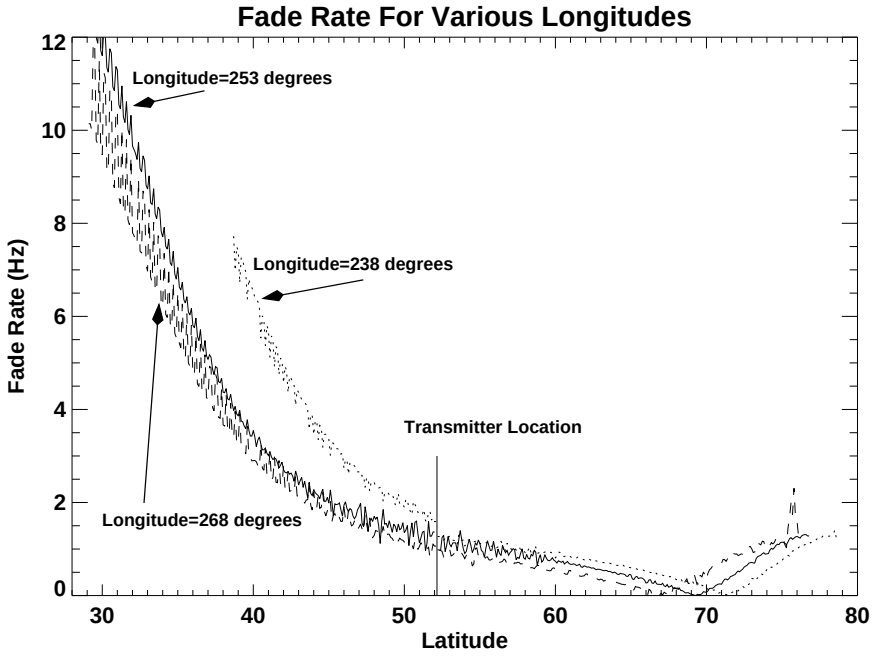


Figure 5.9: The simulated fade rates for various satellite longitudes using the medium 2-D profile.

### 5.2.5 Satellite Track Comparison

The final two comparisons for 15 MHz are between passes at three different longitudes and a pass travelling northeast to one travelling southeast. The comparison between longitudes examines the fade rate and mode delay for passes that pass directly overhead, 15° west and 15° east of Saskatoon. The compared passes use the medium 2-D $N_e$ profile and a satellite travelling northeast at an altitude of 900 km. The results for fade rate and mode delay appear in Figures 5.9 and 5.10 respectively.

The first item that is recognized in both the fade rate and mode delay comparisons is that there is slight disagreement between the simulated results north and south of the transmitter. This is due to the way the program reads the $N_e$ profile and cannot be fixed at this time, however the results are still useful. The pass to the west of the transmitter (longitude 238°) shows higher fade rates and mode delays to the south and lower fade rates and mode delays to the north. This can be explained by reviewing Figure 5.1, considering the northeast directed passes, the pass west of

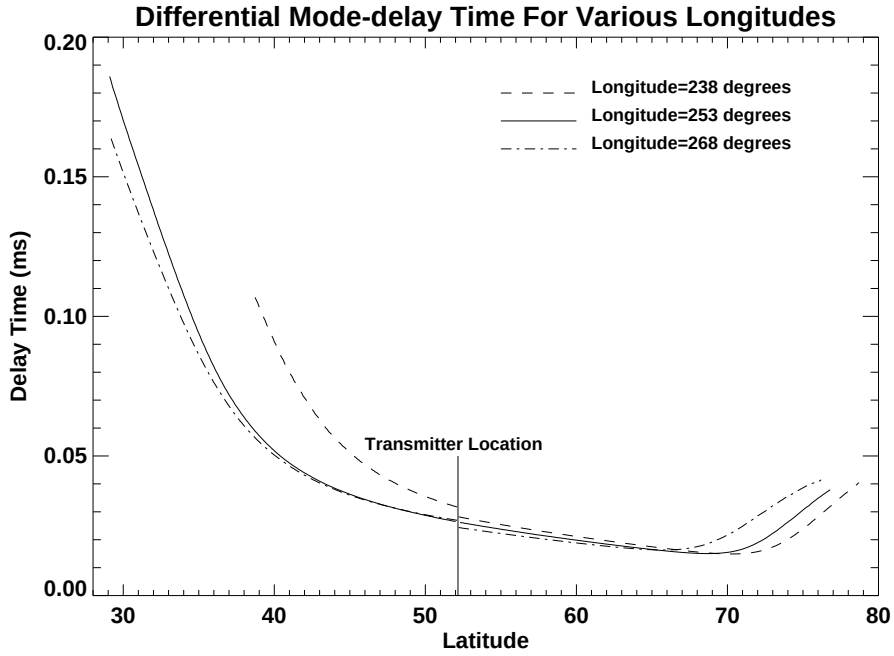


Figure 5.10: The simulated mode delays for various satellite longitudes using the medium 2-D profile.

Saskatoon is further away from the transmitter in the southern portion of the pass than the other passes. In the northern portion of the pass this track is closer to the transmitter, while the other passes are further away. Since the wave is propagating less distance to reach the satellite, in the northern portion of this pass there is less separation of the modes and therefore less Faraday fading and mode delay. The opposite occurs in the southern portion of the pass where the wave must propagate farther to reach the satellite.

The comparison of satellite pass direction uses the medium 2-D profile, with the satellite at 900 km altitude and travelling directly over the transmitter. The comparisons for northeast to southeast passes are shown in Figure 5.11 for fade rate and Figure 5.12 for mode delay. The comparisons of fade rate and mode delay for the two pass directions indicate roughly the same results for both directions. This is expected because of the symmetry of the situation. The propagation direction with respect to the magnetic field is the same in either case and the $N_e$ profile does not

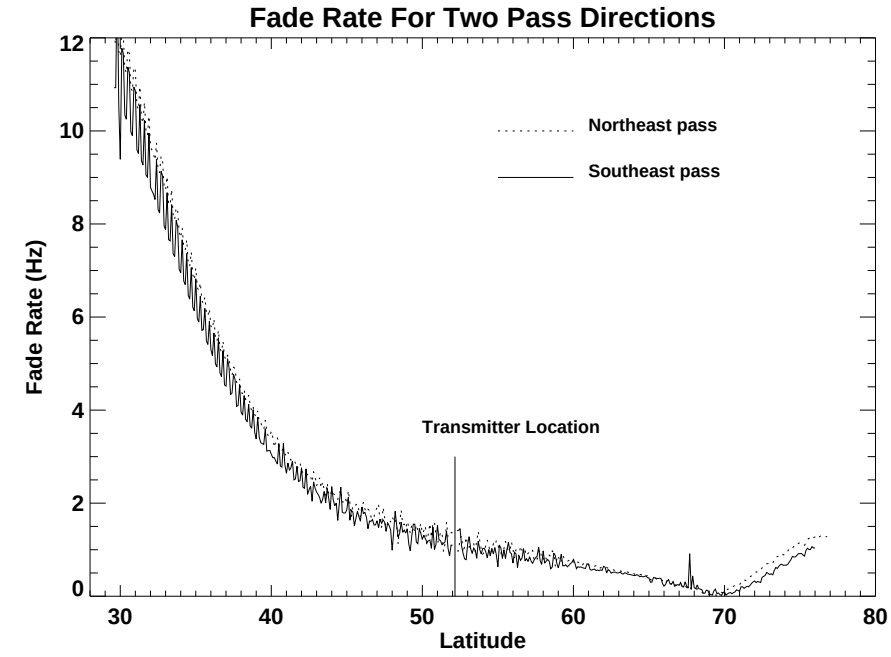


Figure 5.11: The simulated fade rates for the two satellite pass directions using the medium 2-D profile.

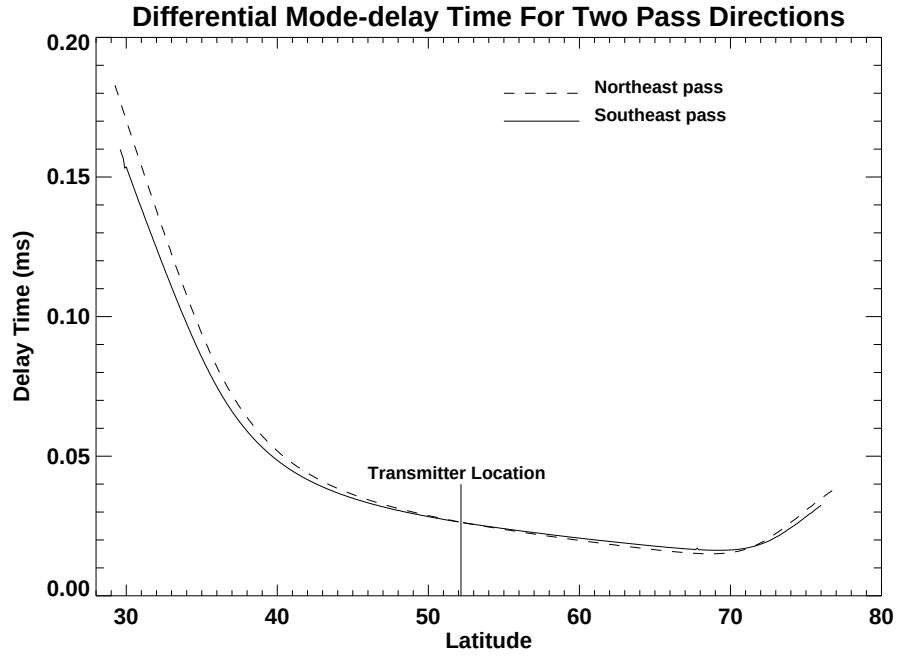


Figure 5.12: The simulated mode delays for the two satellite pass directions using the medium 2-D profile.

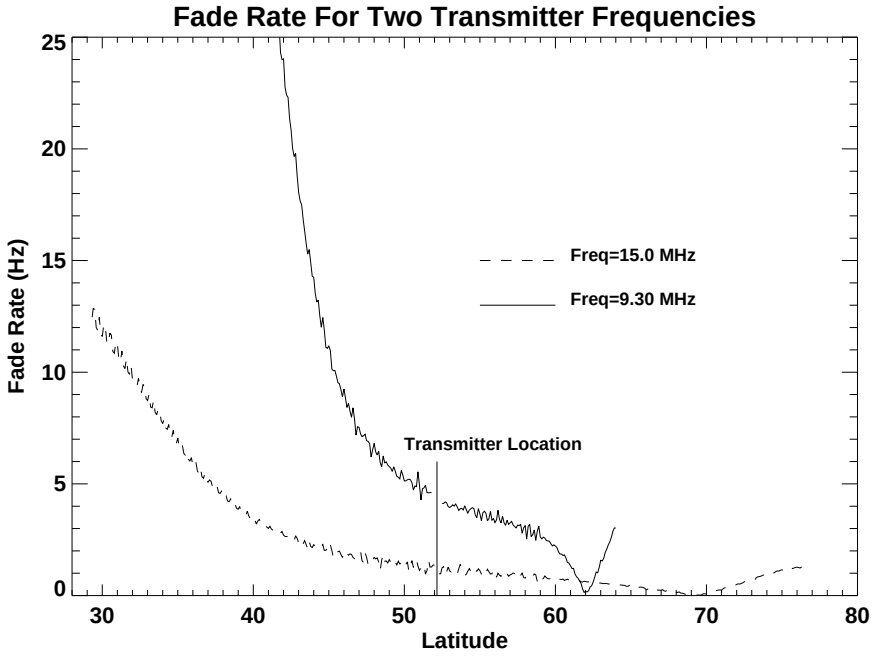


Figure 5.13: The simulated fade rates for two transmitter frequencies using the medium 2-D profile at 900 km satellite altitude.

change with longitude so the results should be similar. These results illustrate that the only difference between the two pass directions is that the radar FOV will be more favourable to a pass travelling northeast over the radar (see Figure 5.1).

### 5.2.6 Transmitter Frequency Comparison

A comparison of two different frequencies was performed using the medium 2-D profile, with the satellite at 900 km altitude and passing northeast directly over the transmitter. The two frequencies compared were 15.0 MHz and 9.30 MHz. The comparison of the two frequencies for fade rate and mode delay are presented in Figures 5.13 and 5.14 respectively. The main features to notice in these figures is that both fade rate and mode delay are much higher for the lower frequency, which should be expected. Also evident in the frequency comparison was that the satellite detects signal over a much broader range for 15 MHz than for 9.30 MHz. The range extends from about 29° to 77° latitude for 15 MHz to 41° to 64° latitude

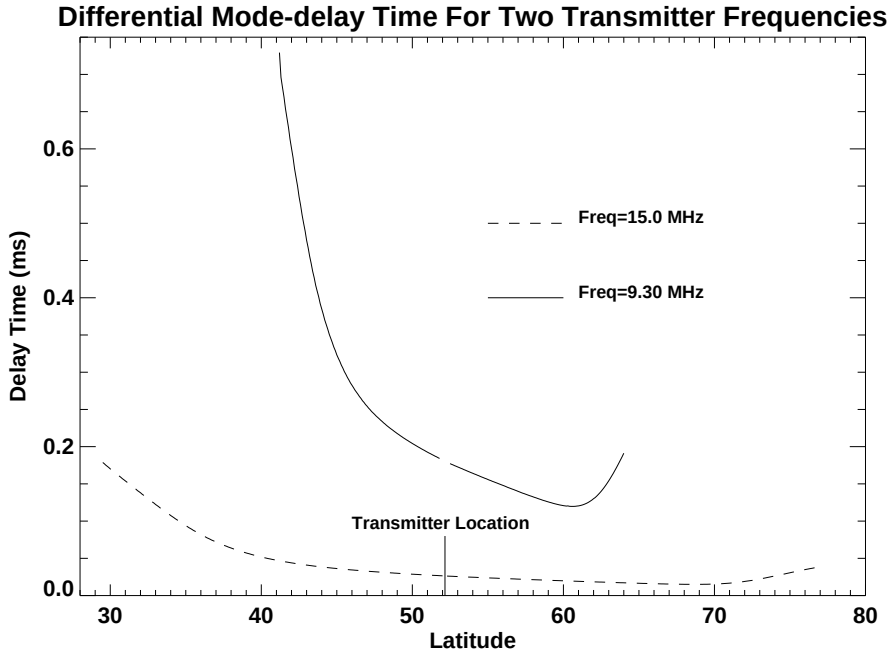


Figure 5.14: The simulated mode delays for two transmitter frequencies using the medium 2-D profile at 900 km satellite altitude.

for 9.30 MHz. This would also be expected as a radar wave will penetrate through the ionosphere at lower elevation angles when a higher frequency is used.

## 5.3 Summary

In anticipation of the RRI instrument becoming operational when ePOP is launched, ray tracing simulations were performed. These simulations have been undertaken with a well behaved and quiet ionosphere using HF transmitter frequencies of 9.303 MHz and 15.0 MHz. Findings from these simulations indicate some general expected behaviours of the received signal. The signal will be detected for a larger range of latitudes for higher frequencies, lower 2-D $N_e$ profiles, and/or higher satellite pass altitudes. The magnitude of Faraday fading and mode delay that is detected will depend on a number of variables. Higher 2-D $N_e$ profiles, larger propagation distances, and/or lower frequencies will increase both fade rate and mode delay.

# Chapter 6

# Conclusions

The focus of this thesis has been a study of transionospheric propagation of HF radar waves through the terrestrial ionosphere. The motivation was to develop a ray tracing model which would help in the interpretation of the RRI (Radio Receiver Instrument) observations on the upcoming ePOP (enhanced Polar Outflow Probe) Canadian led satellite mission. Another Canadian mission, ISIS II, from the 1970s had a transionospheric experiment with some similarities to the RRI one. As such, the transionospheric aspects of this mission were used to validate the ray tracing models. The dominant characteristics of the ISIS II received signal have been explained and simulated. The simulations agree with observed data for the most part and reasonable explanations exist for discrepancies. A preliminary sampling of possible ePOP passes over the Saskatoon SuperDARN array were simulated. These demonstrated the different signal characteristics expected for various different $N_e$ profiles, satellite pass parameters, and transmitting frequencies. The three signal characteristics studied were Faraday fade rates, differential mode delay times, and the latitudinal extent of received signal. There is still much research to be done in this area however.

## 6.1 Ray Tracing Software

A program to calculate the path a radio wave takes through the ionosphere was initially written by D. Andre at the University of Saskatchewan in C programming language. In its base form, the program simply calculates a set of points along the path of a radio wave given inputs of starting wave position, starting wave direction,

$N_e$ profile, and wave frequency. This ray tracing program can calculate the path for either mode of propagation (O- or X-mode) and uses a Hamiltonian approach to solving the Appleton-Hartree equation [*Haselgrove*, 1963] discussed in Chapter 2.

For this thesis, extensive modifications to the program have been made to acquire full signal modelling for the expected radar signal to be received by the RRI on ePOP. One modification allows the user to input a desired ending position for the ray path to pass through. Using this modification the starting parameters of the program now require a desired wave path end position (i.e., the satellite). The program modifies the starting wave direction until a ray path is found which passes within a set distance of the end location. Another modification allowed for simulation of ray paths along a satellite track (points along the orbit of the satellite). Finally, an analysis program was written to take the ray path simulation outputs and calculate the signal characteristics that would be present at the satellite. These characteristics include: the full polarization state of the wave, the propagation time from the ground transmitter to the satellite, and the propagation distance from the ground transmitter to the satellite.

## 6.2 ISIS II Analysis

In 1978 the satellite ISIS II, in conjunction with a ground transmitter in Ottawa, performed an experiment similar to the proposed transionospheric propagation experiment for ePOP. The ISIS II transionospheric experiment supplied a number of passes of good quality transionospheric signals. Interlaced with the transionospheric experiment, the ISIS II satellite performed topside soundings of the ionosphere, its primary data collection mode. These measurements were used to give an estimate of the $f$oF2 peak electron density during each pass. These signals received by ISIS II from the ground have been analyzed in preparation for ePOP RRI experiments.

The analysis indicated that Faraday rotational fading of the signal and time of arrival delay between the two modes was observed predominantly when the satellite was to the south of the Ottawa transmitter. This was explained by considering the

propagation direction of the waves with respect to the magnetic field orientation of the Earth to the south of the Ottawa transmitter (see Figure 4.8). To the south of Ottawa the propagation direction of the radar waves tends to be close to parallel to the magnetic field lines (quasi-longitudinal propagation) while to the north of Ottawa the propagation direction tends to be close to perpendicular to the magnetic field lines (quasi-transverse propagation). Further, in general, electron density increases south of the Ottawa transmitter and this causes more Faraday rotation and more separation between the two modes.

The magnitude of both the periodic fading rate and the differential mode delay has been calculated from the satellite data for each pass. In general, the magnitude of both the fading rate and the mode delay increased as the satellite moved farther from the transmitter. This is predicted behaviour as a wave travels a longer path to reach the satellite resulting in more mode separation and thus more Faraday rotation the further the satellite is from the transmitter. The magnitude calculated for the Faraday fading rate ranged from 0.5 Hz to 13 Hz. The magnitude of mode delay ranged from 0.1 ms to 0.8 ms.

The ray tracing program has been used to simulate the expected ISIS II results for these passes. Ray paths have been simulated over the latitudinal range that includes the observed fading rate and mode delay data for each pass. In total eight passes were simulated for fade rate and eleven passes were simulated for mode delay. The simulated and observed values for both fade rate and mode delay showed similar trends. A regression analysis comparing the measured and simulated data sets was performed. The simulated fade rates compared to modelled fade rates gave a regression slope of 1.07 with a regression coefficient of 0.934. For the comparison of mode delay times a slope of 1.14 and a regression coefficient of 0.930 were obtained. These regression analysis results indicate that there is rather good correlation between the observed and simulated data sets.

## 6.3 ePOP RRI Analysis

The Cassiope satellite, which will carry the ePOP payload, is to be launched in 2007. There will be eight scientific instruments associated with the ePOP payload. A separate communications payload, called Cascade, will be available to provide data storage and a high rate of data transfer for the ePOP scientific instruments. An experiment using the RRI instrument will be undertaken in conjunction with several ground transmitters (e.g., the Saskatoon SuperDARN radar). The ground transmitters will send HF radio waves up through the ionosphere where they will be detected by the passive RRI instrument on ePOP. The modifications to the radio waves as they propagate through the ionosphere to the receiver on ePOP may be used to determine characteristics of the ionosphere through which the wave propagated.

Using the Saskatoon SuperDARN radar as the ground transmitter, ray path modelling was performed for satellite passes under typical scenarios. Different satellite pass altitudes, longitudes and directions have been simulated for ePOP travelling over the Saskatoon SuperDARN. Most of the passes were analyzed with a 15.0 MHz transmitter frequency, but a comparison to the frequency used with ISIS II, 9.30 MHz, was also done.

The simulations produced periodic fade rates in the received signal as high as 16 Hz for the 15.0 MHz wave. For a transmitted frequency of 9.30 MHz, the maximum simulated periodic fade rate increased to 25 Hz. It should be noted that the highest values for fading rate occur when the satellite is nearly out of range of the transmitter. Therefore, the actual signal that is received will most likely be quite noisy and weak under these conditions and the highest fade rate frequencies may not be observed, at least most of the time. The differential mode delay times were up to 0.3 ms for a 15 MHz transmitted wave and up to more than 0.7 ms for a 9.30 MHz transmitted wave. Again, the highest values for mode delay are observed at the far extremes of a pass and therefore may not be measurable in practice.

The modelled signal for the simulated ePOP satellite passes suggested some general trends. In general, lower $N_e$ profiles, higher satellite altitudes and/or higher

frequencies resulted in received signal over a larger range of latitudes. The magnitudes of both Faraday fade rates and differential mode delay depend primarily on the differences between index of refraction and path length of the two modes. As such, higher fade rates and mode delays were observed from the simulations for conditions that cause either a larger difference in path length or a larger difference in index of refraction between the two modes. These parameters include higher (overall) $N_e$ profiles, lower transmitter frequencies, and larger propagation distances.

## 6.4 Summary and Future Work

Future research to be undertaken in preparation for the RRI experiment on Cassiope includes several items. Experiment modes for SuperDARN/ePOP collaborations need to be better defined in light of this research (i.e., transmitted pulse lengths, pulse patterns, pulse durations, etc.). For example, one transmitting mode will use the normal SuperDARN pulse pattern to look at forward and back scatter simultaneously when the RRI is overhead. This experiment will possibly provide a better understanding of F-region irregularities that cause backscatter. Another transmitting mode can be used to study Faraday rotation by sending out long pulses in a periodic pattern. In this mode the RRI will receive the same frequency on each dipole and will operate as a full polarimeter. Another possible mode is to have two frequencies transmitted and have the RRI receive one frequency on one dipole and the other frequency on the other dipole. The difference in Faraday rotation between the two frequencies can be used to estimate the electron density in the ionosphere.

The primary goal of this research was to develop a model of the signal that the RRI will receive from a ground transmitter. Analysis of ISIS II transionospheric data provided a basis for predicting the signal characteristics. Regular signal characteristics such as mode delay and Faraday fading were observed in the ISIS II analysis and similarly will be observed with the RRI experiment. Deviations from these regular signal characteristics are expected to be indicators of structures of interest in the ionosphere. Structures such as density enhancements and depletions could be

indicators of magnetospheric boundaries present in the polar ionosphere or of the mid-latitude trough region of the ionosphere. The modelling presented in this thesis will assist in providing a basis set of signal characteristics which describe some large scale ionospheric properties — significant deviations in the signal characteristics will be indicators of more complex structures. For example, the modelling has shown that fade frequency and mode delay increase for an overall larger $N_e$ in the ionosphere.

Further modelling will take into consideration small scale structures and their effects on the received signal at the RRI. These structures will cause scintillations in the signal properties at the RRI. For example, a sudden increase or decrease in fade rate or mode delay will indicate that the transmitted wave propagated through a small scale density enhancement or depletion. In this way the RRI experiment will provide a means of 'imaging' ionospheric structures and help discover the mechanism for coherent scattering used in experiments such as SuperDARN. A better understanding of scattering mechanisms in the F-region can lead to the development of better methods for studying this region and develop a better understanding of the fundamental physics that occurs. Methods for more readily detecting ionospheric structures and studying fundamentals of the ionosphere (such as the linking of ionospheric processes to solar processes) will lead to better overall models of the ionosphere. In the long term, this will assist in more broad goals such as a better understanding of space weather.

# References


Bhuyan, P.K, M. Chamua, K. Bhuyan, P. Subrahmanyam, and S.C. Garg. *Diurnal, seasonal and latitudinal variation of the electron density in the topside F-region of the Indian zone ionosphere at solar minimum and comparison with the IRI* Journal of Atmospheric and Solar-Terrestrial Physics 65, 359-368, 2003.

Bilitza, D. International Reference Ionosphere - IRI-2001 http://modelweb.gsfc.nasa.gov/models/iri.html. 2004.

Bilitza, D., X. Huang, B.W. Reinisch, R.F. Benson, H.K. Hills, and W.B. Schar. *Topside Ionogram Scaler With True Height Algorithm (TOPIST): Automated processing of ISIS topside ionograms* Radio Science, Vol. 39, 2004.

Bilitza, D. *International Reference Ionosphere 2000* Radio Science, Vol. 36, 261-275, 2001.

Born, M., and E. Wolf. *Principles of Optics: Electromagnetic Theory of Propagation Interference and Diffraction of Light, Sixth Edition* Pergamon Press Canada Ltd., Toronto, 1980.

Budden, K.G. *The propagation of radio waves: The theory of radio waves of low power in the ionosphere and magnetosphere* Cambridge University Press, 1985.

Budden, K.G. *Radio Waves in the Ionosphere* Cambridge University Press, 1961.

CSA - Alouette I and II. CSA. http://www.space.gc.ca/asc/eng/satellites/alouette.asp. December 1, 2005.

CSA - ISIS I and II. CSA. http://www.space.gc.ca/asc/eng/satellites/isis.asp. December 1, 2005.

Danskin, D.W., A.V. Koustov, T. Ogawa, N. Nishitani, S. Nozawa, S.E. Milan, M. Lester and D. Andre. *On the factors controlling occurrence of F region coherent echoes* Annales Geophysicae 20, 1-13, 2002.

Davies, K. *Ionospheric Radio Propagation* General Publishing Company, Ltd. Toronto, 1966.

Greenwald, R.A., K.B. Baker, J.R. Dudeney, M. Pinnock, T.B. Jones, E.C. Thomas, J.-P. Villain, J.-C. Cerisier, C. Senior, C. Hanuise, R.D. Hunsucker, G. Sofko, J. Koehler, E. Nielsen, R. Pellinen, A.D.M. Walker, N.

Sato, and H. Yamagishi. *DARN/SuperDARN: A Global View of the Dynamics of High-Latitude Convection* Space Science Reviews, 71, 761-796, 1995.

Griffiths, D.J. *Introduction to Electrodynamics, Third Edition* Prentice Hall, New Jersey, 1999.

Hartz, T.R. *Observations of the Galactic Radio Emission Between 1.5 and 10 MHz From the Alouette Satellite* Annales D'Astrophysique, 27, 823-830, 1964.

Haselgrove, J. *The Hamiltonian ray path equations* JATP 25, 397-399, 1963.

Hussey, G.C. Ph.D. Thesis, Institute of Space and Atmospheric Studies, University of Saskatchewan, 1994. *The Polarization of 50 MHz Auroral Backscatter*

Hunsucker, R.D., and J.K. Hargreaves. *The High-Latitude Ionosphere and its Effects on Radio Propagation* Cambridge University Press, 2003.

Hysell, D.L., and J.L. Chau. *Inferring E region electron density profiles at Jicamarca from Faraday rotation of coherent scatter* Journal of Geophysical Research, Vol. 106, 30371-30381, 2001.

James, H.G., R.G. Gillies, G.C. Hussey, and P. Prikryl. *HF fades caused by multiple wave fronts detected by a dipole antenna in the ionosphere* Submitted to Radio Science, 2005.

James, H.G. *Effects on transionospheric HF propagation observed by ISIS at middle and auroral latitudes* Adv. Space Res., in press, DOI: 10.1016/j.asr.2005.03.114, 2005.

James, H.G. *High-frequency direction finding in space* Review of Scientific Instruments, Vol. 74, No. 7, 3478-3486, 2003.

James, H.G., W. Calvert. *Interference Fringes detected by OEDIPUS C* Radio Science, Vol. 33, No. 3, 1998.

Kelley, M.C. *The Earth's Ionosphere: Plasma Physics and Electrodynamics* Academic Press, Inc. San Diego, 1989.

Kivelson, M.G., and C.T. Russell. *Introduction to Space Physics* Cambridge University Press, 1995.

Kovalick, T. SPDF - Coordinated Data Analysis Web (CDAWeb). NASA. http://cdaweb.gsfc.nasa.gov/cdaweb/pre_istp/. 2004

MacDougall, J.W., I.F. Grant and X. Shen. *The Canadian Advanced Digital Ionosonde: Design and Results* Rep. UAG-104, Ionosondes and Ionosonde Networks, pp 21-27, World Data Center A, Boulder, 1995.

Mancuso, S., and S.R. Spangler. *Coronal Faraday Rotation Observations: Measurements and Limits on Plasma Inhomogeneities* The Astrophysical Journal, 525, 195-208, 1999.

Maus, S., S. Macmillan, T. Chernova, S. Choi, D. Dater, V. Golovkov, V. Lesur, F. Lowes, H. Luhr, W. Mai, S. McLean, N. Olsen, M. Rother, T. Sabaka, A. Thomson and T. Zvereva. *The 10th generation international geomagnetic reference field* Physics of the Earth and Planetary Interiors, 151, 320-322, 2005.

Molcho, J., D. Censor. *A simple derivation and an example of Hamiltonian ray propagation* American Journal of Physics, Vol. 54, Issue 4, 1986.

Richards, P.G. *Seasonal and solar cycle variations of the ionospheric peak electron density: Comparison of measurement and models* Journal of Geophysical Research, Vol. 106, No. A7, Pages 12,803-12,819, 2001.

Shpynev, B.G. *Incoherent scatter Faraday rotation measurements on a radar with single linear polarization* Radio Science, Vol. 39, 2004.

Trondsen, T.S., and Cogger, L.L. *A Survey of Small-Scale Spatially Periodic Distortions of Auroral Forms* J. Geophys. Res. Vol. 103, 1998.

University of Calgary. CASSIOPE. ePOP. http://mertensiana.phys.ucalgary.ca/cassiope.htm. December 19, 2005.

Wang, L., J.W. MacDougall, and H.G. James. *Ionospheric structure effects on HF radio wave propagation for the Enhanced Polar Outflow Probe (e-POP) satellite mission* Radio Science, Vol. 39, 2004.

Yau, A.W., L.L. Cogger, E.P. King, D.J. Knudsen, J.S. Murphree, T.S. Trondsen, K. Tsuruda, H.G. James, I. Walkty. *The Polar Outflow Probe (POP): Science Objectives and Instrument Development* Canadian Aeronautics and Space Journal, Vol. 48, No. 1, 2002.

# Appendix A

# Ray Trace Program

Program 'tracer.c' was written in its base form by Dieter Andre after which extensive modifications were performed.

```
/Author: Dieter Andre
/Modified by: Rob Gillies

/************************ Main program: TRACER ******************/
/* Call: tracer 'directory-name' 'parameter-filename' ['no_3d'] */
/************************************************************/

 int main(int argc, char *argv[], char *envp[])

{
extern double maximal_range, maximal_stepsize;
double *ys;
int nok, nbad, iray, no_3d;
float year= (float) 1980.0;
float dimo;
char fnm[80]; /* ray output file name */
FILE *rf;

/* spacong between rays is 1/10 degree */
#define DEL_RAY 0.1* degtorad

/* for the four rays at the corners of a beam */
/* ccw from lower left corner */
/* these start at index 1, index 0 not used */
int kount[ 5]; /* actual number of intermediate
/ steps that has been stored */
double *xp[ 5]; /* storage of intermediate
/steps; independent variable */
double **yp[ 5]; /* storage of intermediate
/steps; dependent variables */
int ibc, j, k, nc, zerocount, numnonconverge;
int run, no_change, ind, indh;
int l, final_ind1, final_ind2;
double d, d1, d2, df;
double  del;
```

```
double  dela, finhgt;
double x, y, z;
double xf, yf, zf;
double delta_elev, delta_azi, elev1, elev0, azim1, azim0;
double de, da;
double d1e, d1a, d2e, d2a;
double temp1, temp2;
double a, b;
double phi1, theta1, phi2, theta2, phi3, theta3;
double alt1, altmax, lat1, lat2, lat3, alt2, alt3;
double phif1, phif2, phif3, altf1, latf1, latf2;
double latf3, altf2, altf3, thetaf1, thetaf2, thetaf3;
double x1, y1, z1, x2, y2, z2, x3, y3, z3;
double delta_pol, delta_polnew, delta_azinew;
double thetas, phis, lats, alts;
double heightdif1, heightdif2;
double lat_eps= 1.0e-6;
double rho, rlat_1, sin_lat, cap_c_inv;
double clat, slat;
double cap_s, xy_tmp;

elev1=0.0;
elev0=0.0;
azim1=0.0;
azim0=0.0;
ground =1;
numnonconverge=0;
if ( argc < 3)
{
printf( "Call: tracer 'directory-name' 'parameter-filename' ['no_3d'=0]\n");
goto finish;
}
directory_name= (char* ) calloc( 80, sizeof( char) );
strcpy( directory_name, argv[1]);
no_3d= atoi( argv[3]);
read_parameters( argv[2]);

printf("Number of traces to be done:  %i\n\n", numtraces);
for (p=0; p<numtraces; p++)
{
 // maximal_range = 2500.0 * 1000.0;
  //num_stor = 15000;
  feldcof( "/home/gillies/igrf/data/", &year, &dimo);
  ys= dvector( 1, num_vars);
  y_start= dvector( 1, num_vars);
```

```
  for ( ibc= 1; ibc <= 4; ibc++)
    {
    xp[ ibc]= dvector( 1, num_stor);
    yp[ ibc]= dmatrix( 1, num_vars, 1, num_stor);
    }
  kmax= num_stor -1;
  dxsav= storage_interval;
  /* calculate ray start position in cartesian and store */
  ray_start_pos= dvector( 1, 3);
  init_starting_values( ray_elev[ 1], ray_azim[ 1], ys);
  ray_start_pos[ 1]= ys[ 1];
  ray_start_pos[ 2]= ys[ 2];
  ray_start_pos[ 3]= ys[ 3];

  /* write electron profile */
  if (no_3d == 0)
    output_ne_profile( 240.0* degtorad, 0.2* degtorad, 301,
50.0* degtorad,  0.2* degtorad, 151,
80000.0, 5000.0, 81 );
    output_ne_slice( );

//=========================================
  //coordinate transform
  //=========================================

  Satlong[p]=Satlong[p]*3.14159265359/180;
  Satlat[p]=Satlat[p]*3.14159265359/180;
  geod_to_cart(Satlong[p], Satlat[p], Satalt[p]*1000.0, &Xsat[p], &Ysat[p], &Zsat[p] );



  Xsat[p]=(6378206.0*1/sqrt(1.0-0.0067686*sin(Satlat[p])*sin(Satlat[p]))+Satalt[p]*1000.0)
$*cos(Satlat[p])*cos(Satlong[p]);
Ysat[p]=(6378206.0*1/sqrt(1.0-0.0067686*sin(Satlat[p])*sin(Satlat[p]))+Satalt[p]*1000.0)
$*cos(Satlat[p])*sin(Satlong[p]);
Zsat[p]=(6335033.0*1/sqrt(1.0-0.0067686*sin(Satlat[p])*sin(Satlat[p]))+Satalt[p]*1000.0)
$*sin(Satlat[p]);
  //=====================================================
   if (rays_to_trace == 'O')
     {
ray_mode= 'o';
printf("%s\n", directory_name);
printf ("O-mode converging %i\n", parameternum[p]);

}
```

```
   if (rays_to_trace == 'E')
    {
    ray_mode= 'e';
printf("%s\n", directory_name);
printf ("X-mode converging %i\n", parameternum[p]);
      ;
}



//coordinates that are required for the ray to end up at (m)
       xf=Xsat[p];
yf=Ysat[p];
zf=Zsat[p];
//initial jump size for elev and azi
        if (p==0)
{
delta_elev=.05*3.14159265359/180;
delta_azi=.05*3.14159265359/180;
}
        else
{
delta_elev=.05*3.14159265359/180;
delta_azi=.05*3.14159265359/180;
        }

if (p > 1)
{
  delta_elev=elev1-elev0;
  delta_azi=azim1-azim0;
  ray_elev[1]=elev1+delta_elev;
  ray_azim[1]=azim1+delta_azi;
  ray_elev[2]=elev1+delta_elev;
  ray_azim[2]=azim1+delta_azi;
}
elev0=elev1;
azim0=azim1;

printf ("sat. lat= %f\n", Satlat[p]*180/3.14159265359);
printf ("sat. long= %f\n", Satlong[p]*180/3.14159265359);
printf ("sat. alt= %f\n\n", Satalt[p]);
printf ("xsat= %f\n", xf/1000.0);
printf ("ysat= %f\n", yf/1000.0);
printf ("zsat= %f\n", zf/1000.0);
printf ("initial elevation angle= %f\n", ray_elev[1]*180/3.14159265359);
```

```
printf ("initial azimuth angle= %f\n\n", ray_azim[1]*180/3.14159265359);

run=0;
satellite_check=0;
//for running this conversion, we'll estimate satellite lat and long
/*
  phis= atan2( Ysat[p], Xsat[p]);
  if ( phis < 0.0 )
    phis= 2.0* 3.14159265359 + phis;
  rho= sqrt( Xsat[p]* Xsat[p] + Ysat[p]* Ysat[p]);
  lats= atan( Zsat[p]/ rho);
  do
    {
      rlat_1= lats;
      sin_lat= sin( rlat_1);
      cap_c_inv= sqrt( 1.0 - ecce2* sin_lat* sin_lat);
      lats= atan( ( Zsat[p] + erequ* ecce2* sin_lat/ cap_c_inv)/ rho);
    }
  while ( fabs( lats - rlat_1) > lat_eps);
  if ( fabs( lats) < (85.0* degtorad) )
    alts= rho/ cos( lats) - erequ/ cap_c_inv;
  else
    alts= Zsat[p]/ sin( lats) - erequ* ( 1.0 - ecce2)/ cap_c_inv;

thetas=90.0-lats;
printf ("converging lat= %f\n", lats*180.0/3.14159265359);
printf ("converging long= %f\n", phis*180.0/3.14159265359);
printf ("converging alt= %f\n", alts);
*/
//start of convergance part
for (;;)
       {
       satellite_check=0;

       //go through once for theta1 and phi1
       for (iray=1; iray<=ray_num; iray++)
        {
  for ( ibc= 1; ibc <= 4; ibc++)
    {
      switch ( ibc)
        {
        case 0:
  init_starting_values( ray_elev[ iray], ray_azim[ iray], ys); break;
        case 1:
  init_starting_values( ray_elev[ iray], ray_azim[ iray] + DEL_RAY, ys); break;
```

```
        case 2:
  init_starting_values(ray_elev[iray]+DEL_RAY,ray_azim[iray]+DEL_RAY,ys);break;
        case 3:
  init_starting_values( ray_elev[ iray] + DEL_RAY, ray_azim[ iray], ys); break;
        }
              trace_err= 'f';
      odeint( ys, num_vars, x_start, x_stop, accuracy, initial_stepsize, minimal_stepsize,
   &nok, &nbad, &kount[ ibc], xp[ ibc], yp[ibc], maximal_stepsize);
    }

}
        if (satellite_check == 0)
{
        printf ("satellite check= %i\n", satellite_check);
}
//finding index of nearest height to sat. alt
        for (l=0; l<kount[1]; l++)
    {
x1=yp[1][1][l];
y1=yp[1][2][l];
z1=yp[1][3][l];
   cart_to_geod(x1, y1, z1, &phi1, &lat1, &alt1 );



  alt1=alt1*.001;
heightdif2=fabs(alt1-Satalt[p]);
//if (l < 500)
// {
 // printf ("alt1= %f\n", alt1);
// printf ("hd1= %f\n", heightdif2);
// }
        if (heightdif2 < heightdif1 || l==0)
    {

heightdif1=heightdif2;
altf1=alt1;
latf1=lat1;
phif1=phi1;
indh=l;
    }
}

//finding initial distance of two modes and closest index
//printf ("x= %f\n", yp[1][1][indh]*.001);
```

```
//printf ("y= %f\n", yp[1][2][indh]*.001);
//printf ("z= %f\n", yp[1][3][indh]*.001);
//printf ("xs= %f\n", xf*.001);
//printf ("ys= %f\n", yf*.001);
//printf ("zs= %f\n", zf*.001);
x=yp[1][1][indh]-xf;
y=yp[1][2][indh]-yf;
z=yp[1][3][indh]-zf;
        d=sqrt(x*x+y*y+z*z);

thetaf1=3.14159265359/2-latf1;
printf ("lat= %f\n", latf1*180.0/3.14159265359);
printf ("long= %f\n", phif1*180.0/3.14159265359);
printf ("alt= %f\n", altf1);
//printf ("height dif.= %f\n", heightdif1);
printf ("d= %f \n\n", d*.001);
df=d;
if (d < 10.0)
{
printf ("final distance(m)= %f\n\n", d);
numnonconverge=0;
break;
}// check if distance is less than minumum wanted

//go through once for theta2 and phi2  (change elevation)
       for (iray=1; iray<=ray_num; iray++)
        {
  for ( ibc= 1; ibc <= 4; ibc++)
    {
      switch ( ibc)
        {
        case 0:
  init_starting_values( ray_elev[ iray]+delta_elev, ray_azim[ iray], ys); break;
        case 1:
  init_starting_values( ray_elev[ iray]+delta_elev, ray_azim[ iray] + DEL_RAY, ys); break;
        case 2:
  init_starting_values(ray_elev[iray]+delta_elev+DEL_RAY,ray_azim[iray]+DEL_RAY,ys);break;
        case 3:
  init_starting_values( ray_elev[ iray]+delta_elev + DEL_RAY, ray_azim[ iray], ys); break;
        }
              trace_err= 'f';
     odeint( ys, num_vars, x_start, x_stop, accuracy, initial_stepsize, minimal_stepsize,
   &nok, &nbad, &kount[ ibc], xp[ ibc], yp[ibc], maximal_stepsize);
    }
```

```
}
for (l=0; l<kount[1]; l++)
    {
x2=yp[1][1][l];
y2=yp[1][2][l];
z2=yp[1][3][l];
cart_to_geod(x2, y2, z2, &phi2, &lat2, &alt2 );
alt2=alt2*.001;
heightdif2=fabs(alt2-Satalt[p]);
        if (heightdif2 < heightdif1 || l==0)
    {
heightdif1=heightdif2;
altf2=alt2;
latf2=lat2;
phif2=phi2;
indh=l;
    }
}
thetaf2=3.14159265359/2-latf2;

//printf ("lat2= %f\n", 90.0-thetaf2*180/3.14159265359);
     //   printf ("long2= %f\n", phif2*180/3.141592653659);
// printf ("alt2= %f\n", altf2);
//printf ("height dif.= %f\n\n", heightdif1);
//printf ("d2= %f \n\n", d*.001);

//go through once for theta3 and phi3  (change azimuth)
       for (iray=1; iray<=ray_num; iray++)
        {
  for ( ibc= 1; ibc <= 4; ibc++)
    {
      switch ( ibc)
        {
        case 0:
  init_starting_values( ray_elev[ iray], ray_azim[ iray]+delta_azi, ys); break;
        case 1:
  init_starting_values( ray_elev[ iray], ray_azim[ iray]+delta_azi + DEL_RAY, ys); break;
        case 2:
  init_starting_values(ray_elev[iray]+DEL_RAY,ray_azim[iray]+delta_azi+DEL_RAY,ys);break;
        case 3:
  init_starting_values( ray_elev[ iray] + DEL_RAY, ray_azim[ iray]+delta_azi, ys); break;
        }
              trace_err= 'f';
      odeint( ys, num_vars, x_start, x_stop, accuracy, initial_stepsize, minimal_stepsize,
   &nok, &nbad, &kount[ ibc], xp[ ibc], yp[ibc], maximal_stepsize);
```

```
    }

}



for (l=0; l<kount[1]; l++)
    {
x3=yp[1][1][l];
y3=yp[1][2][l];
z3=yp[1][3][l];
cart_to_geod(x3, y3, z3, &phi3, &lat3, &alt3 );
alt3=alt3*.001;
heightdif2=fabs(alt3-Satalt[p]);
        if (heightdif2 < heightdif1 || l==0)
    {
heightdif1=heightdif2;
altf3=alt3;
latf3=lat3;
phif3=phi3;
indh=l;
    }

    }
thetaf3=3.14159265359/2-latf3;

// printf ("lat3= %f\n", 90.0-thetaf3*180/3.14159265359);
   //     printf ("long3= %f\n", phif3*180/3.141592653659);
// printf ("alt3= %f\n", altf3);
// printf ("height dif.= %f\n\n", heightdif1);


//calculate change in polar angle (90-elevation angle) and azimuth
        delta_pol=-delta_elev;
thetas=3.14159265359/2-Satlat[p];
phis=Satlong[p];
//printf ("phis= %f\n", phis*180/3.14159265359);
//printf ("thetas= %f\n", thetas*180/3.14159265359);

delta_polnew=delta_pol*(phis-phif1-((phif1-phif3)/(thetaf1-thetaf3))*
$(thetas-thetaf1))/(phif2-phif1-((phif1-phif3)/(thetaf1-thetaf3))*(thetaf2-thetaf1));

delta_azinew=delta_azi*(phis-phif1-((phif1-phif2)/(thetaf1-thetaf2))*
$(thetas-thetaf1))/(phif3-phif1-((phif1-phif2)/(thetaf1-thetaf2))*(thetaf3-thetaf1));
```

```
printf ("del_elev= %f\n", -delta_polnew*180/3.14159265359);
printf ("del_azi= %f\n", delta_azinew*180/3.14159265359);

delta_elev=-delta_polnew;
delta_azi=delta_azinew;
ray_elev[1]=ray_elev[1]+delta_elev;
ray_azim[1]=ray_azim[1]+delta_azi;
ray_elev[2]=ray_elev[2]+delta_elev;
ray_azim[2]=ray_azim[2]+delta_azi;

printf ("new elevation angle= %f\n", ray_elev[1]*180/3.14159265359);
printf ("new azimuth angle= %f\n", ray_azim[1]*180/3.14159265359);
run++;
printf ("Number of times through=  %i\n\n", run);
if (run > 14)
{
printf ("final distance(m)= %f\n\n", df);
//printf ("Not Converging.\n");
break;
}
}
sprintf( fnm, "%s%c%d.ray", directory_name, ray_mode, parameternum[p]);
rf= fopen( fnm, "wb");
fwrite( &elev_num, sizeof( int), 1, rf);
fwrite( &azim_num, sizeof( int), 1, rf);
fwrite( &ray_num, sizeof( int), 1, rf);
//go through once more with new values and write to file
for (iray=1; iray<=ray_num; iray++)
        {
  for ( ibc= 1; ibc <= 4; ibc++)
    {
      switch ( ibc)
        {
        case 0:
  init_starting_values( ray_elev[ iray], ray_azim[ iray], ys); break;
        case 1:
  init_starting_values( ray_elev[ iray], ray_azim[ iray] + DEL_RAY, ys); break;
        case 2:
  init_starting_values(ray_elev[iray]+DEL_RAY,ray_azim[iray]+DEL_RAY,ys);break;
        case 3:
  init_starting_values( ray_elev[ iray] + DEL_RAY, ray_azim[ iray], ys); break;
        }
              trace_err= 'f';
      odeint( ys, num_vars, x_start, x_stop, accuracy, initial_stepsize, minimal_stepsize,
   &nok, &nbad, &kount[ ibc], xp[ ibc], yp[ibc], maximal_stepsize);
```

```
    }
//finding final index
for (l=0; l<kount[1]; l++)
{
 x2=yp[1][1][l]-xf;
           y2=yp[1][2][l]-yf;
         z2=yp[1][3][l]-zf;
                 temp1=sqrt(x2*x2+y2*y2+z2*z2);
                 if (temp1<d2e || l==0){
 d2e=temp1;
 final_ind1=l;
 }
}

  output_all ( rf, iray, nok, nbad, kount, xp, yp, final_ind1);
}
//printf ("ray_elev[1]= %f\n", ray_elev[1]*180/3.14159265359);
elev1=ray_elev[1];
azim1=ray_azim[1];
      fclose( rf);
}
finish:;
}
```

# Appendix B

# Ray Trace Analysis Program

Program 'rayanalyze.pro' written to determine wave characteristics from ray paths.

```
;Written by: Rob Gillies

PRO rayanalyze, rayo, raye

  pi=3.14159265359

phasedifcalc, rayo, raye, phasedif, dis
polarcalc, rayo, raye, orient, ellipt, phasedif

  num=rayo[0,0].find
  lat=(*rayo[0,0].rdat)(num).glat
  phase=phasedif
  orient=orient*180/pi
  chi=ellipt*180/pi
  aspect=(*rayo[0,0].rdat)(num).aspect_angle
  alt=(*rayo[0,0].rdat)(num).galt

print, "Latitude=", lat
print, "Altitude (km)=", alt
print, "Phase Difference=", phase
print, "Orientation Angle=", orient
print, "Ellipticity Angle=", chi
print, "Distance Between rays=", dis
END

pro raysana, rayo, raye, p, r
  pi=3.14159265359

phasedifcalc, rayo, raye, phasedif, dis, opath, epath, tototime, totetime
polarcalc, rayo, raye, orient, ellipt, phasedif
  num=rayo[0,0].find
  p.lat(r)=(*rayo[0,0].rdat)(num).glat
  p.phase(r)=phasedif
  p.orient(r)=orient*180/pi
  p.chi(r)=ellipt*180/pi
  p.aspect(r)=(*rayo[0,0].rdat)(num).aspect_angle
```

```
  p.dis(r)=dis
  p.alt(r)=(*rayo[0,0].rdat)(num).galt
  p.elevo(r)=rayo[0,0].selev
  p.eleve(r)=raye[0,0].selev
  p.opath(r)=opath*0.001
  p.epath(r)=epath*0.001
  p.otime(r)=tototime
  p.etime(r)=totetime
  p.x(r)=(*rayo[0,0].rdat)(num).x
  p.y(r)=(*rayo[0,0].rdat)(num).y
  p.z(r)=(*rayo[0,0].rdat)(num).z

print, r
print, "Latitude=", p.lat(r)
print, "Altitude (km)=", p.alt(r)
print, "Phase Difference=", p.phase(r)
print, "Orientation Angle=", p.orient(r)
print, "Ellipticity Angle=", p.chi(r)
print, "Distance Between rays=", p.dis(r)
print, "Total O-mode path (km)=", p.opath(r)
print, "Total X-mode path (km)=", p.epath(r)
print, "Total O-mode time (ms)=", p.otime(r)
print, "Total X-mode time (ms)=", p.etime(r)

END

PRO phasedifcalc, rayo, raye, phasedif, disbrays, totopath, totepath, tototime, totetime
  ;constants
  pi=3.14159265359
  freq=9.303e6
  afreq=2*pi*freq
  c=2.99792458e8
  eo=8.85418782e-12
  e=1.6021773e-19
  me=9.109390e-31
  totphaseo=0.0
  totphasee=0.0
  totopath=0.0
  totepath=0.0
  tototime=0.0
  totetime=0.0
  numtest=1000

  onum=rayo[0,0].find  ;# points to final O-mode point
  enum=raye[0,0].find  ;# points to final X-mode point
```

```
  oray={x:DBLARR(onum+1), y:DBLARR(onum+1), z:DBLARR(onum+1), bx:DBLARR(onum+1),$
by:DBLARR(onum+1), bz:DBLARR(onum+1), edens:DBLARR(onum+1), theta:DBLARR(onum+1),$
n:DBLARR(onum+1), phase:DBLARR(onum+1)}
  eray={x:DBLARR(enum+1), y:DBLARR(enum+1), z:DBLARR(enum+1), bx:DBLARR(enum+1),$
by:DBLARR(enum+1), bz:DBLARR(enum+1), edens:DBLARR(enum+1), theta:DBLARR(enum+1),$
n:DBLARR(enum+1), phase:DBLARR(enum+1)}
  oray.x=(*rayo[0,0].rdat)(0:onum).x
  oray.y=(*rayo[0,0].rdat)(0:onum).y
  oray.z=(*rayo[0,0].rdat)(0:onum).z
  oray.bx=(*rayo[0,0].rdat)(0:onum).bx
  oray.by=(*rayo[0,0].rdat)(0:onum).by
  oray.bz=(*rayo[0,0].rdat)(0:onum).bz
  oray.edens=(*rayo[0,0].rdat)(0:onum).edens
  oray.theta=(*rayo[0,0].rdat)(0:onum).aspect_angle

  eray.x=(*raye[0,0].rdat)(0:enum).x
  eray.y=(*raye[0,0].rdat)(0:enum).y
  eray.z=(*raye[0,0].rdat)(0:enum).z
  eray.bx=(*raye[0,0].rdat)(0:enum).bx
  eray.by=(*raye[0,0].rdat)(0:enum).by
  eray.bz=(*raye[0,0].rdat)(0:enum).bz
  eray.edens=(*raye[0,0].rdat)(0:enum).edens
  eray.theta=(*raye[0,0].rdat)(0:enum).aspect_angle

  for i=0, (onum-1) DO BEGIN
    opath=sqrt((oray.x(i)-oray.x(i+1))^2+(oray.y(i)-oray.y(i+1))$
^2+(oray.z(i)-oray.z(i+1))^2)*1000.0
    X=oray.edens(i)*e^2/eo/me/afreq^2
    B=sqrt(oray.bx(i)^2+oray.by(i)^2+oray.bz(i)^2)*1.0e-9
    Y=B*e/me/afreq
    Yt=Y*sin(oray.theta(i)*pi/180.0)
    Yl=Y*cos(oray.theta(i)*pi/180.0)
    oray.n(i)=sqrt(1-X/(1-Yt^2/(2*(1-X))+sqrt(Yt^4/(4*(1-X)^2)+Yl^2)))
    oray.phase(i)=afreq/c*oray.n(i)*opath
    otime=opath/oray.n(i)/c
    ; print, oray.phase(i)
    tototime=tototime+otime
    totopath=totopath+opath
    totphaseo=oray.phase(i)+totphaseo
  ENDFOR

  for i=0, (enum-1) DO BEGIN
    epath=sqrt((eray.x(i)-eray.x(i+1))^2+(eray.y(i)-eray.y(i+1))$
^2+(eray.z(i)-eray.z(i+1))^2)*1000.0
    X=eray.edens(i)*e^2/eo/me/afreq^2
```

```
    B=sqrt(eray.bx(i)^2+eray.by(i)^2+eray.bz(i)^2)*1.0e-9
    Y=B*e/me/afreq
    Yt=Y*sin(eray.theta(i)*pi/180.0)
    Yl=Y*cos(eray.theta(i)*pi/180.0)
    eray.n(i)=sqrt(1-X/(1-Yt^2/(2*(1-X))-sqrt(Yt^4/(4*(1-X)^2)+Yl^2)))
    eray.phase(i)=afreq/c*eray.n(i)*epath
    etime=epath/eray.n(i)/c
    ; print, oray.phase(i)
    totetime=totetime+etime


    totepath=totepath+epath
   ; print, oray.phase(i)-eray.phase(i)
    totphasee=eray.phase(i)+totphasee
  ENDFOR
  tototime=tototime*1000.0
  totetime=totetime*1000.0

  disbrays=sqrt((oray.x(onum)-eray.x(enum))^2+(oray.y(onum)-eray.y(enum))$
^2+(oray.z(onum)-eray.z(enum))^2)*1000.0
  ;print, disbrays

  phasedif=totphaseo-totphasee

END

PRO polarcalc, rayo, raye, orient, ellipt, phasedif

 ;constants
  pi=3.14159265359
  freq=9.303e6
  afreq=2*pi*freq
  c=2.99792458e8
  eo=8.85418782e-12
  e=1.6021773e-19
  me=9.109390e-31

  onum=rayo[0,0].find  ;# points to final O-mode point
  enum=raye[0,0].find  ;# points to final X-mode point
  oray={x:DBLARR(onum+1), y:DBLARR(onum+1), z:DBLARR(onum+1), bx:DBLARR(onum+1),$
by:DBLARR(onum+1), bz:DBLARR(onum+1), edens:DBLARR(onum+1), theta:DBLARR(onum+1),$
n:DBLARR(onum+1), aplus:DBLARR(onum+1), aminus:DBLARR(onum+1),$
rhoplus:DBLARR(onum+1), rhominus:DBLARR(onum+1)}
  eray={x:DBLARR(enum+1), y:DBLARR(enum+1), z:DBLARR(enum+1), bx:DBLARR(enum+1),$
by:DBLARR(enum+1), bz:DBLARR(enum+1), edens:DBLARR(enum+1), theta:DBLARR(enum+1),$
```

```
n:DBLARR(enum+1), aplus:DBLARR(enum+1), aminus:DBLARR(enum+1),  $
rhoplus:DBLARR(enum+1), rhominus:DBLARR(enum+1)}
  oray.x=(*rayo[0,0].rdat)(0:onum).x
  oray.y=(*rayo[0,0].rdat)(0:onum).y
  oray.z=(*rayo[0,0].rdat)(0:onum).z
  oray.bx=(*rayo[0,0].rdat)(0:onum).bx
  oray.by=(*rayo[0,0].rdat)(0:onum).by
  oray.bz=(*rayo[0,0].rdat)(0:onum).bz
  oray.edens=(*rayo[0,0].rdat)(0:onum).edens
  oray.theta=(*rayo[0,0].rdat)(0:onum).aspect_angle

  eray.x=(*raye[0,0].rdat)(0:enum).x
  eray.y=(*raye[0,0].rdat)(0:enum).y
  eray.z=(*raye[0,0].rdat)(0:enum).z
  eray.bx=(*raye[0,0].rdat)(0:enum).bx
  eray.by=(*raye[0,0].rdat)(0:enum).by
  eray.bz=(*raye[0,0].rdat)(0:enum).bz
  eray.edens=(*raye[0,0].rdat)(0:enum).edens
  eray.theta=(*raye[0,0].rdat)(0:enum).aspect_angle

;initial polarization

  ax=0.0
  ay=1.0

;for testing only
;onum=501;;;;;;;;
;enum=501;;;;;;;;
;;;;;;;;;;;;;;;;

  for i=0, (onum-1) DO BEGIN
    X=oray.edens(i)*e^2/eo/me/afreq^2
    B=sqrt(oray.bx(i)^2+oray.by(i)^2+oray.bz(i)^2)*1.0e-9
    Y=B*e/me/afreq
    Yt=Y*sin(oray.theta(i)*pi/180.0)
    Yl=Y*cos(oray.theta(i)*pi/180.0)
    oray.rhoplus(i)=abs(1/yl*(yt^2/(2*(1-X))-sqrt(yt^4/(4*(1-X)^2)+yl^2)))
    ;oray.rhoplus(i)=Yt^2/(2*Yl*(1-X))+sqrt(Yt^4/(4*Yl^2*(1-X)^2)+1)
    oray.rhominus(i)=1.0/oray.rhoplus(i)
    ;if (i EQ 210) then print, oray.rhoplus(i), oray.rhominus(i)
    axplus=1/sqrt(1+oray.rhoplus(i)^2)
    ayplus=oray.rhoplus(i)*axplus
    axminus=1/sqrt(1+oray.rhominus(i)^2)
    ayminus=oray.rhominus(i)*axminus
```

```
    oray.aplus(i)=ax*axplus+ay*ayplus
    oray.aminus(i)=ax*axminus-ay*ayminus

    ax=oray.aplus(i)*axplus
    ay=oray.aplus(i)*ayplus
   ; print, oray.aplus(i), oray.aminus(i)
ENDFOR
  axplusf=axplus
  aplusf=oray.aplus(onum-1)
  ayplusf=ayplus
;print, " "
  ax=0.0
  ay=1.0

  for j=0, (enum-1) DO BEGIN
    X=eray.edens(j)*e^2/eo/me/afreq^2
    B=sqrt(eray.bx(j)^2+eray.by(j)^2+eray.bz(j)^2)*1.0e-9
    Y=B*e/me/afreq
    Yt=Y*sin(eray.theta(j)*pi/180.0)
    Yl=Y*cos(eray.theta(j)*pi/180.0)
    eray.rhoplus(j)=abs(1/yl*(yt^2/(2*(1-X))-sqrt(yt^4/(4*(1-X)^2)+yl^2)))
    ; eray.rhoplus(j)=Yt^2/(2*Yl*(1-X))+sqrt(Yt^4/(4*Yl^2*(1-X)^2)+1)
    eray.rhominus(j)=1.0/eray.rhoplus(j)
   ; print, eray.rhoplus(j), eray.rhominus(j)
    axplus=1/sqrt(1+eray.rhoplus(j)^2)
    ayplus=eray.rhoplus(j)*axplus
    axminus=1/sqrt(1+eray.rhominus(j)^2)
    ayminus=eray.rhominus(j)*axminus
   ; print, axminus, ayminus
    eray.aplus(j)=ax*axplus-ay*ayplus
    eray.aminus(j)=ax*axminus+ay*ayminus
    ; print, eray.aplus(j), eray.aminus(j)
    ax=eray.aminus(j)*axminus
    ay=eray.aminus(j)*ayminus

 ;   print, eray.aplus(j), eray.aminus(j), eray.rhoplus(j), eray.rhominus(j), eray.theta(j)

  ENDFOR
axminusf=axminus
aminusf=eray.aminus(enum-1)
ayminusf=ayminus
;print, axplusf, ayplusf, aplusf
;print, axminusf, ayminusf, aminusf
axfinal=sqrt(axminusf^2*aminusf^2+aplusf^2*axplusf^2-2*$
aplusf*aminusf*axplusf*axminusf*cos(phasedif))
```

```
ayfinal=sqrt(ayminusf^2*aminusf^2+aplusf^2*ayplusf^2+2*$
aplusf*aminusf*ayplusf*ayminusf*cos(phasedif))
;print, axfinal, ayfinal
denx=axplusf*aplusf*sin(phasedif)
numx=-aplusf*axplusf*cos(phasedif)+aminusf*axminusf
phasexf=atan(numx/denx)
if (numx GT 0.0 AND denx LT 0.0) then phasexf=phasexf+pi
if (numx LT 0.0 AND denx LT 0.0) then phasexf=phasexf+pi
if (numx LT 0.0 AND denx GT 0.0) then phasexf=phasexf+2*pi
deny=-ayplusf*aplusf*cos(phasedif)-aminusf*ayminusf
numy=-aplusf*ayplusf*sin(phasedif)
phaseyf=atan(numy/deny)
if (numy GT 0.0 AND deny LT 0.0) then phaseyf=phaseyf+pi
if (numy LT 0.0 AND deny LT 0.0) then phaseyf=phaseyf+pi
if (numy LT 0.0 AND deny GT 0.0) then phaseyf=phaseyf+2*pi
;print, phasexf*180/pi, phaseyf*180/pi
numorient=2*axfinal*ayfinal*cos(phaseyf-phasexf)
denorient=axfinal^2-ayfinal^2
orient=atan(numorient/denorient)
if (numorient GT 0.0 AND denorient LT 0.0) then orient=orient+pi
if (numorient LT 0.0 AND denorient LT 0.0) then orient=orient+pi
if (numorient LT 0.0 AND denorient GT 0.0) then orient=orient+2*pi
orient=orient/2.0
;print, "Final orientation angle=", orient*180/pi
numellipt=2*axfinal*ayfinal*sin(phaseyf-phasexf)
denellipt=axfinal^2+ayfinal^2
ellipt=asin(numellipt/denellipt)
if (ellipt LT 0.0) then ellipt=abs(ellipt)
ellipt=ellipt/2.0
;print, "Final ellipticity angle=", ellipt*180/pi
END
```